GEÇİCİ KAPAK

Kapak tasarımı devam ediyor.

BİDGE Yayınları

Advances ın Power Systems, Renewable Energy Integratıon and Electrıcal Machıne Desıgn

Editor: ALİ CAN ÇABUKER

ISBN: -

1st Edition
Page Layout By: Gözde YÜCEL
Publication Date: -
BİDGE Yayınları

All rights reserved. No part of this work may be reproduced in any form or by any means, except for brief quotations for promotional purposes with proper source attribution, without the written permission of the publisher and the editor.

Certificate No: 71374
All rights reserved © BİDGE Yayınları
www.bidgeyayinlari.com.tr - bidgeyayinlari@gmail.com
Krc Bilişim Ticaret ve Organizasyon Ltd. Şti.
Güzeltepe Mahallesi Abidin Daver Sokak Sefer Apartmanı No: 7/9 Çankaya / Ankara

CONTENTS

CHAPTER 0

MULTİ-OBJECTİVE OPTİMAL POWER FLOW İN PV-INTEGRATED POWER SYSTEMS AND FDB-BASED METAHEURİSTİC ALGORİTHMS

HASAN UZEL[1]

Introduction

Research Background and Motivation

Renewable energy systems have become an important component of modern power grids due to increasing electricity demand and environmental concerns associated with fossil-fuel-based generation. Among renewable technologies, solar photovoltaic (PV) systems have experienced particularly rapid growth during the last decade. According to International Energy Agency (IEA) reports, the global installed PV capacity has continued to increase steadily, while Türkiye's installed solar capacity exceeded 25 GW in 2023 according to EMRA statistics.

The increasing penetration of PV systems introduces additional uncertainty into power system operation due to the variability of solar irradiance and environmental conditions. As a

[1] Assistant Professors, Amasya University, Faculty of Arts and Sciences, Department of Artificial Intelligence and Machine Learning, Orcid: 0000-0002-8238-2588

result, conventional optimization approaches become more difficult to apply under non-linear and stochastic operating conditions. In this context, the optimal power flow (OPF) problem has become one of the main tools used to evaluate the operational impact of renewable energy integration.

The OPF problem was first formulated by Carpentier (1962) and has since been extensively studied using different mathematical models and solution techniques. Classical deterministic methods, such as Newton–Raphson, interior-point, and linear programming approaches, are generally effective for smooth and convex optimization problems. However, renewable-energy-integrated OPF formulations often include non-linear, multi-modal, and conflicting objectives that reduce the effectiveness of conventional approaches. For this reason, metaheuristic optimization algorithms have become widely used in recent OPF studies (Carpentier, 1962).

Optimal Power Flow: Literature Review

Classical OPF Methods

Early OPF studies mainly relied on linear and quadratic programming techniques. Dommel and Tinney (1968) later adapted the Newton–Raphson method for OPF analysis, forming the basis of many modern OPF solvers. Over time, interior-point methods (IPM), sequential quadratic programming (SQP), and active-set approaches were also introduced into the literature.

These methods generally provide efficient convergence for smooth and convex optimization problems. However, practical OPF formulations that include valve-point effects, renewable energy integration, and multiple objectives often become highly non-linear and multi-modal. Under such conditions, conventional gradient-based approaches may converge to local optima or experience reduced performance. As a result, stochastic and metaheuristic

optimization algorithms have attracted increasing attention in recent OPF research (Dommel & Tinney, 1968).

Metaheuristic OPF Methods

Table 1 Prominent Metaheuristic Methods in the OPF Literature

Algorithm	Reference	OPF Application	Test System	Main Contribution
PSO	Abido (2002)	Cost + voltage profile + voltage stability	IEEE 30	Early PSO-based OPF application
Genetic Algorithm (GA)	Guvenc et al. (2012)	Fuel cost minimization + voltage profile + voltage stability	IEEE 30	GA based on similarity for OPF; early evolutionary approach PSO-based OPF application
Grey Wolf Opt. (GWO)	El-Fergany & Hasanien (2015)	Cost + loss + voltage stability	IEEE 30	GWO applied to OPF optimization
WOA	Medani et al. (2018)	Reactive power dispatch	IEEE 14/30/114	WOA-based active power loss minimization
CEPSO	Daghan et al. (2021)	Cost + voltage profile + stability + losses	IEEE 30	Chaos-assisted PSO for multi-objective OPF
FDB-AGDE	Guvenc et al. (2021)	Security-constrained OPF + RES	IEEE 30	FDB-based adaptive guided differential evolution
Lévy-FDB-COA	Duman et al. (2021)	Cost + emission	IEEE 30	Lévy flight + FDB hybrid coyote optimization
FDB-SFS	Aras et al. (2021)	RES + OPF (stochastic)	IEEE 30/57	Adaptive FDB-integrated stochastic fractal search
FDB-AGSK	Bakır et al. (2023)	Reactive power OPF	IEEE 30/57	FDB-guided gaining-sharing knowledge algorithm
EO-OPF	Houssein et al. (2023)	Cost + emission + PV	IEEE 30/57	Equilibrium optimizer for OPF
FDB-ARO	Bakır (2024)	Cost + loss + RES + FACTS	IEEE 30	Dynamic FDB-ARO; solar, wind and FACTS devices integrated OPF

Metaheuristic algorithms have been widely used in OPF studies because they can handle non-linear, non-convex, and multi-modal optimization problems without requiring gradient information

(Adetunji et al., 2021). Different approaches inspired by swarm intelligence and evolutionary computation have been applied to OPF over the last two decades. Among the earliest, Guvenc et al. (2012) applied a genetic algorithm (GA) based on similarity-based chromosome generation to minimize fuel cost on the IEEE 30-bus system. Subsequently, PSO (Kennedy & Eberhart, 1995) gained widespread adoption, GWO (Mirjalili et al., 2014), WOA (Mirjalili & Lewis, 2016), and social spider optimization (Nguyen, 2019). Single- and multi-objective OPF formulations incorporating renewable energy sources have also been addressed using Jaya-based methods (El-Sattar et al., 2019; Elattar & ElSayed, 2019), teaching-learning-based approaches (Akbari et al., 2021), and hybrid reactive power dispatch methods (Shaheen et al., 2021). Stochastic RES-integrated OPF has further been studied using heuristic algorithms (Khan et al., 2020) and the Equilibrium Optimizer (Faramarzi et al., 2020; Houssein et al., 2023). In addition, chaos-assisted PSO variants have demonstrated improved solution quality in OPF problems (Daghan et al., 2021). FDB-based approaches incorporating transient stability constraints have also been proposed (Sonmez et al., 2024). The FDB selection strategy itself was introduced by Kahraman et al. (2020) as a generalized guide-selection mechanism applicable across different metaheuristic frameworks.

More recently, guide-selection mechanisms have received increasing attention as a means of improving the convergence behavior of metaheuristic algorithms in OPF. The FDB selection strategy, introduced by Kahraman et al. (2020), evaluates candidates based on both fitness quality and distance from the current best solution, offering a generalized guide-selection mechanism applicable across different algorithm structures. Building on this foundation, FDB-based variants incorporating transient stability constraints have also been proposed (Sonmez et al., 2024).

Table 1 shows that metaheuristic algorithms have been extensively applied to OPF problems in recent years. Most existing studies focused on improving search operators, hybrid algorithm structures, or renewable-energy-integrated OPF formulations. In contrast, guide-solution selection mechanisms have received comparatively limited attention, despite their potential influence on convergence behavior and population diversity.

Literature Gaps in Recent OPF Studies

Recent studies on OPF have increasingly focused on renewable-energy-integrated optimization problems, particularly under PV and stochastic operating conditions. For instance, Hassan et al., (2021a) applied the Rao-3 algorithm to reactive power dispatch with time-varying demand and RES uncertainty on the IEEE 30-bus and 57-bus systems, demonstrating competitive performance under stochastic operating conditions. Existing research has mainly concentrated on developing new hybrid metaheuristic structures and improving solution quality for IEEE benchmark systems. However, several limitations remain in the current literature.

First, the simultaneous application and comparison of the FDB strategy across multiple algorithms remain limited. Second, PV uncertainty modeling using lognormal distributions has received comparatively less attention than conventional deterministic or Weibull-based approaches (Ebeed et al., 2023). Third, many OPF studies report only average optimization results without comprehensive statistical validation using non-parametric tests such as Wilcoxon and Friedman analyses (Duman et al., 2023). Even studies applying FDB-based methods have reported results primarily in terms of best and average objective values (Duman et al., 2021). These gaps provide the main motivation for the present study.

The main research gaps identified in recent PV-integrated OPF studies and the corresponding contributions of the present work are summarized in Table 2.

Table 2 Identified Research Gaps and Contributions of This Study

Research Gap	Current Status	This Study's Approach
Simultaneous FDB application to PSO, GWO and WOA	Applied separately to single algorithms	Three algorithms enhanced with FDB, compared under identical conditions
Lognormal PV uncertainty in multi-objective OPF	Normal or Weibull distributions common	Lognormal + Monte Carlo (N_s=200) applied
IEEE 57-bus FDB comparative OPF	30-bus common; 57-bus comparison lacking	Parallel analysis on both 30-bus and 57-bus
Cost+emission Pareto + statistical testing	Single-objective studies dominant	Pareto + Wilcoxon + Friedman applied
Theoretical dynamic analysis of FDB-WOA	Behavior observed empirically; no math analysis	Mathematical analysis of FDB-WOA dynamics
Computational complexity and runtime analysis	Solution quality mainly emphasized	Runtime and complexity analysis

OPF with Renewable Energy Integration

The integration of renewable energy sources (RES) introduces uncertainty into OPF problems due to the variable nature of solar and wind power generation. In the literature, RES-integrated OPF studies are generally classified into four groups: deterministic models, probabilistic approaches, scenario-based methods, and robust optimization frameworks. Within the probabilistic category, Hassan et al. (2021b) proposed a modified Rao-2 algorithm for OPF incorporating renewable energy sources, providing an effective solution approach for stochastic power system operation.

Deterministic approaches use fixed or forecasted renewable generation values, whereas probabilistic methods model uncertainty using statistical distributions such as normal, Weibull, or lognormal distributions. Scenario-based approaches commonly employ Monte

Carlo simulations, while robust OPF methods aim to maintain acceptable system performance under worst-case operating conditions.

In this study, PV uncertainty is modeled using a lognormal distribution. This approach is preferred because solar irradiance data are positive-valued and generally exhibit right-skewed behavior, making the lognormal model suitable for representing PV variability. Several studies have adopted lognormal-based uncertainty modeling in PV-integrated OPF frameworks (Biswas et al., 2018; Atwa et al., 2010), and stochastic OPF formulations combining PV with wind and other RES have confirmed its suitability (Ebeed et al., 2023).

Fitness-Distance Balance (FDB) Strategy

The performance of metaheuristic optimization algorithms is closely related to the balance between exploration and exploitation as well as the guide-solution selection mechanism. In many conventional algorithms, the guide solution is selected directly as the individual with the best fitness value (e.g., *gBest in PSO, α wolf in GWO, or X* in WOA*). Although this strategy may accelerate convergence, it can also reduce population diversity and increase the risk of premature convergence in multi-modal search spaces.

To address this limitation, Kahraman et al. (2020) proposed the Fitness–Distance Balance (FDB) strategy. Unlike conventional guide-selection approaches, FDB considers both the fitness quality of candidate solutions and their distance from the current best solution. In this way, solutions located in relatively unexplored regions of the search space may also contribute to the search process, helping maintain exploration capability and population diversity (Kahraman et al., 2020).

Since its introduction, the FDB mechanism has been integrated into different optimization algorithms. Prior to the development of FDB, PSO-based approaches combined with chaotic

maps and FACTS devices had already been applied to stochastic OPF problems with wind power (Duman et al., 2020). More recently, Altun et al. (2024) proposed the Hyper-FDB-INFO algorithm, which combines FDB with the INFO algorithm and a hyper-heuristic initialization strategy based on LSHADE, and applied it to the optimal placement and sizing of FACTS devices in wind power-integrated OPF, achieving superior performance over standard INFO and FDB-INFO variants. Building on such foundations, FDB-Coyote Optimization was proposed by Duman et al. (2021), FDB-Stochastic Fractal Search by Aras et al. (2021), FDB-Adaptive Guided Differential Evolution by Guvenc et al. (2021), FDB-Stochastic OPF by Duman et al. (2023), and FDB-ARO by Bakır (2024). However, the simultaneous application of FDB to PSO, GWO, and WOA within a multi-objective PV-integrated OPF framework remains limited in the literature. This limitation constitutes one of the main motivations of the present study.

Study Objectives and Original Contributions

The primary objective of this chapter is to solve the multi-objective OPF problem in IEEE 30-bus and 57-bus test systems integrated with PV generation using FDB-enhanced PSO, GWO, and WOA algorithms, and to compare the performance of these algorithms with comprehensive statistical tests.

The original contributions of this study are summarized as follows:

- Development of FDB-PSO, FDB-GWO and FDB-WOA three FDB-based algorithm versions and comparative analysis with standard versions under identical simulation conditions.
- Integration of PV power output uncertainty via a lognormal distribution model into the OPF formulation;

20 MW nominal PV capacity for IEEE 30-bus and 50 MW for IEEE 57-bus.

- Bi-objective Pareto analysis covering fuel cost and emission minimization; construction of Pareto fronts with 15 different weight combinations via the weighted-sum approach.
- Statistical evaluation based on 10 independent runs: proof of statistical significance of algorithm performance using Wilcoxon signed-rank test and Friedman test.
- Assessment of algorithmic scalability in two test systems of different scales: IEEE 30-bus and IEEE 57-bus.
- Theoretical dynamic analysis of FDB-WOA behavior and mathematical explanation of why X*-centered updates respond differently to FDB integration than other algorithms (Chapter 4).

Scope and Limitations

This chapter is evaluated within the following scope and limitations:

Scope

- Active power dispatch optimization (reactive power and transformer tap ratios are held constant).
- Solar PV integration only (wind energy is outside the scope of this study).
- Standard IEEE test systems; real grid data not used.
- Static OPF analysis; dynamic and transient analyses are out of scope.

Limitations

- Independent run count limited to 10; larger samples would increase statistical confidence.
- PV uncertainty modeled only with lognormal distribution; comparison of different distribution models is a future research topic.
- Dual objective function used; adding voltage deviation and power losses as separate objectives can be addressed in future work.
- Full AC-OPF formulation (including reactive power optimization) is outside the scope of this study; planned for future work.
- Sensitivity analysis performed only for FDB parameter k and update period; systematic analysis of other parameter combinations is presented in Chapter 5.

Chapter Organization

The remainder of this study is organized as follows. Chapter 2 presents the mathematical formulation of the OPF problem together with the objective functions and system constraints. Chapter 3 describes the PV uncertainty model and the integration of PV systems into the OPF framework. Chapter 4 introduces the FDB-based optimization algorithms and their mathematical structures. Chapter 5 presents the simulation results, Pareto analysis, and statistical evaluations for the IEEE 30-bus and IEEE 57-bus systems. Finally, Chapter 6 summarizes the main findings, limitations, and future research directions.

Mathematıcal Formulatıon

General OPF Formulation

The optimal power flow (OPF) problem seeks to obtain the optimal operating conditions of a power system while satisfying system constraints. In its general form, the OPF problem can be expressed as follows (Carpentier, 1962):

$$\text{Minimize} \quad F(x, u) \tag{1}$$

$$\text{Subject to:} \quad g(x, u) = 0 \tag{2}$$

$$h\_min \leq h(x, u) \leq h\_max \tag{3}$$

x : State variables vector

u : Control variables vector

F(x, u) : Objective function (or vector) to be minimized

g(x, u) : Equality constraints vector (power balance equations)

h(x, u) : Inequality constraints vector

h_min, h_max : Lower and upper bounds of inequality constraints

State and Control Variables

The OPF formulation consists of state variables (x) and control variables (u).

The state variables include:

- Bus voltage magnitudes: V_i, i = 2, 3, ..., N (load buses)
- Voltage phase angles: δ_i, i = 2, 3, ..., N (excluding reference bus)
- Generator reactive power outputs: Qg_i, i = 1, 2, ..., NG

- Active power losses: P_loss

Control variables u are the quantities the operator optimizes:

- Generator active power outputs: Pg_i, $i = 1, 2, ..., NG$
- Voltage magnitudes: Vg_i, $i = 1, 2, ..., NG$
- Transformer tap ratios: t_k, $k = 1, 2, ..., NT$ (fixed in this study)
- Compensator reactive power outputs: Qc_j, $j = 1, 2, ..., NC$ (fixed in this study)

In this study, only generator active power outputs (Pg_i) are optimized, while transformer tap ratios and reactive compensator settings are kept constant to simplify the optimization problem and enable a fair algorithmic comparison.

Objective Functions

Fuel Cost Function

The operating cost of thermal power plants is modeled using the widely used second-order polynomial function: (Carpentier, 1962).

$$f_1 = \Sigma_{i=1}^{NG} C_i(Pg_i) = \Sigma_{i=1}^{NG} (a_i \cdot Pg_i^2 + b_i \cdot Pg_i + c_i)[\$/hour] \quad (4)$$

a_i, b_i, c_i : Generator i fuel cost coefficients ($\$/MW^2h$, $\$/MWh$, $\$/h$)

Pg_i : Active power output of generator i (MW)

NG : Total number of generators

In real systems, the valve-point effect causes the cost function to be discontinuous and multi-modal:

$$C_i(Pg_i) = a_i Pg_i^2 + b_i Pg_i + c_i + |e_i \cdot \sin(f_i \cdot (Pg_i\_min - Pg_i))| \quad (5)$$

The valve-point effect is not included in this study; the standard quadratic cost model (Eq. 4) is used.

Emission Function

The environmental cost of thermal power generation, measured primarily in terms of NOx and other harmful gases:

$$f_2 = \Sigma_{i=1}^{NG} E_i(Pg_i) = \Sigma_{i=1}^{NG} (\alpha_i \cdot Pg_i^2 + \beta_i \cdot Pg_i + \gamma_i) \text{ [ton/hour]} \quad (6)$$

α_i, β_i, γ_i : Generator i emission coefficients (ton/MW²h, ton/MWh, ton/h)

Active Power Losses

The active power losses are calculated using the Kron loss formula:

$$P\_loss = \Sigma_{i=1}^{NG} \Sigma_{j=1}^{NG} Pg_i \cdot B_{ij} \cdot Pg_j + \Sigma_{i=1}^{NG} B_{0i} \cdot Pg_i + B_{00} \quad (7)$$

Losses are not optimized as a separate objective in this study but are reported in the results evaluation.

Multi-Objective Optimization Framework

In this study, two conflicting objectives fuel cost (f_1) and emission (f_2) are simultaneously minimized.

Weighted Sum Method

The weighted sum method is adopted for constructing the Pareto front:

$$F\_total(x,u) = w_1 \cdot \hat{f}_1(x,u) + w_2 \cdot \hat{f}_2(x,u) \quad (8)$$

subject to:

$$w_1 + w_2 = 1, \quad 0 < w_1, w_2 < 1 \quad (9)$$

The objective functions are normalized as follows:

$$\hat{f}_i = (f_i - f_i\_min) / (f_i\_max - f_i\_min + \varepsilon), \quad i = 1, 2 \quad (10)$$

Table 3 This StudyWeight Scanning Parameters

Parameter	Value	Description
Number of weight combinations	15	different (w_1, w_2) combinations
w_1 range	0.05 - 0.95	Cost weight
w_2 range	0.95 - 0.05	Emission weight
Step size	≈0.0643	Equally spaced scan
Solution method	FDB-PSO/GWO/WOA	Independent run per weight

Pareto Optimality

According to the Pareto dominance principle, solution x^1 dominates another solution x^2 ($x^1 > x^2$) if:

$$f_i(x^1) \le f_i(x^2) \quad \forall i \in \{1,2,...,k\} \quad \text{and} \quad \exists j: f_j(x^1) < f_j(x^2) \qquad (11)$$

The set of solutions not dominated by any other solution is called the Pareto optimal set; its image in the objective space is the Pareto front.

In this study, the Pareto front is approximated using weighted-sum-based optimization with different weight combinations. Although evolutionary multi-objective algorithms can provide broader Pareto coverage, the weighted-sum method remains a widely used approach for comparative multi-objective analysis (Deb et al., 2002).

System Constraints

The OPF problem is subject to equality and inequality constraints that reflect the physical and technical limits of the power system.

Equality Constraints

The equality constraints correspond to the active and reactive power balance equations:

$$(Pg_i + Ppv,_i) - P\_D - P\_loss = 0 \qquad (12)$$

$$\Sigma_i Qg_i - Q\_D - Q\_loss = 0 \quad (13)$$

The bus power flow equations based on the admittance matrix are expressed as:

$$Pg_i - Pd_i = V_i \cdot \Sigma_j V_j (G_{ij}\cos \delta_{ij} + B_{ij}\sin \delta_{ij}) \quad (14)$$

$$Qg_i - Qd_i = V_i \cdot \Sigma_j V_j (G_{ij}\sin \delta_{ij} - B_{ij}\cos \delta_{ij}) \quad (15)$$

where (G_{ij}) and (B_{ij}) denote the real and imaginary components of the bus admittance matrix, respectively.

Inequality Constraints

The inequality constraints define the operating limits of generators and bus voltages:

$$Pg_i\_min \le Pg_i \le Pg_i\_max, \quad i = 1, 2, ..., NG \quad (16)$$

$$Qg_i\_min \le Qg_i \le Qg_i\_max, \quad i = 1, 2, ..., NG \quad (17)$$

$$V_i\_min \le V_i \le V_i\_max, \quad i = 1, 2, ..., N \quad (18)$$

In this study: $V_i\_min = 0.95$ p.u. and $V_i\_max = 1.10$ p.u.

Table 4 OPF Constraint Summary

Constraint Type	Variable	Lower Bound	Upper Bound	Category
Active power balance	Pg, Ppv	—	—	Equality
Reactive power balance	Qg	—	—	Equality
Generator active power	Pg_i	Pg_i_min	Pg_i_max	Inequality
Generator reactive power	Qg_i	Qg_i_min	Qg_i_max	Inequality
Bus voltage magnitude	V_i	0.95 p.u.	1.10 p.u.	Inequality
PV power output	Ppv	0	P_rated	Inequality

Constraint Handling Strategy

Metaheuristic optimization algorithms may generate infeasible solutions during the search process. Therefore, a repair mechanism is applied after each update step to maintain constraint feasibility.

Boundary Constraint Repair

A clipping operator is applied to the generator power limits:

$$Pg_i \leftarrow \max(Pg_i\_min, \min(Pg_i, Pg_i\_max)) \quad (19)$$

Power Balance Repair

After clipping, the total active power balance may be violated. This balance is restored by proportionally distributing the power difference across all generators:

$$\Delta = \Sigma_i Pg_i + E[Ppv] - P\_D \quad (20)$$

$$Pg_i \leftarrow Pg_i - \Delta / NG, \quad \forall i \quad (21)$$

The generator limits are then checked again using the clipping operator.

This repair strategy guarantees that the algorithm always works with physically valid solutions satisfying constraints at every iteration. The full pseudo-code of the repair procedure is given in Chapter 4.

Test Systems: IEEE 30-Bus and IEEE 57-Bus

Table 5 IEEE 30-Bus and IEEE 57-Bus System Characteristics

Characteristic	IEEE 30-Bus	IEEE 57-Bus
Number of buses	30	57
Number of generators (NG)	6	7
Number of load buses	24	50
Number of transmission lines	41	80
Total active load (P_D)	283.4 MW	1250.8 MW
Total reactive load (Q_D)	126.2 MVAr	336.4 MVAr
Reference bus	Bus 1 (slack)	Bus 1 (slack)
Voltage limits (all buses)	[0.95, 1.10] p.u.	[0.95, 1.10] p.u.
PV capacity (this study)	20 MW (Bus 6)	50 MW (Bus 7)
Optimization variables	IEEE 30-Bus	IEEE 57-Bus
Literature reference	30	57

The IEEE 30-bus and IEEE 57-bus systems are used to evaluate the performance of the proposed optimization algorithms. These benchmark systems are commonly used in OPF studies due to their different network scales and operating characteristics (Zimmerman et al., 2011).

Table 6 IEEE 30-Bus — Generator Cost and Emission Coefficients

Gen	Pg_min	Pg_max	a ($/MW²h)	b ($/MWh)	c ($/h)	α (t/MW²h)	β (t/MWh)	γ (t/h)	Note
G1	50	200	0.00375	2.000	0	0.04091	-0.05554	0.06490	Slack bus
G2	20	80	0.01750	1.750	0	0.02543	-0.06047	0.05638	—
G3	15	50	0.06250	1.000	0	0.04258	-0.05094	0.04586	—
G4	10	35	0.00834	3.250	0	0.05326	-0.03550	0.03380	—
G5	10	30	0.02500	3.000	0	0.04258	-0.05094	0.04586	—
G6	12	40	0.02500	3.000	0	0.06131	-0.05555	0.05151	PV integration

Table 7 IEEE 57-Bus — Generator Cost and Emission Coefficients

Gen	Pg_min	Pg_max	a ($/MW²h)	b ($/MWh)	c ($/h)	α (t/MW²h)	β (t/MWh)	γ (t/h)	Note
G1	36	575	0.00110	8.100	0	0.03500	-0.04500	0.05000	Slack bus
G2	10	100	0.01750	1.750	0	0.02543	-0.06047	0.05638	—
G3	10	60	0.06250	1.000	0	0.04258	-0.05094	0.04586	—
G4	12	60	0.00834	3.250	0	0.05326	-0.03550	0.03380	—
G5	12	60	0.02500	3.000	0	0.04258	-0.05094	0.04586	—
G6	10	60	0.02500	3.000	0	0.06131	-0.05555	0.05151	—

Problem Dimensions

The IEEE 30-bus and IEEE 57-bus systems differ in terms of network scale, generator count, and load demand. In this study, only generator active power outputs are optimized, resulting in a low-dimensional OPF formulation suitable for comparative evaluation of the proposed algorithms.

Integratıon Of Pv Systems Into Opf

The integration of solar photovoltaic (PV) systems into power networks introduces additional uncertainty into OPF problems due to the variable and non-dispatchable nature of solar

generation. PV output continuously changes depending on solar irradiance, temperature, and atmospheric conditions, making uncertainty modeling an important component of PV-integrated OPF studies.

Different probabilistic models have been proposed in the literature for representing PV uncertainty, including normal, beta, Weibull, and lognormal distributions. The lognormal distribution is widely considered suitable for modeling solar irradiance because of its positive-valued and right-skewed characteristics (Atwa et al., 2010; Ullah et al., 2019). Several PV-integrated OPF studies have confirmed the appropriateness of this model for representing irradiance variability under uncertain operating conditions (Biswas et al., 2018; Ebeed et al., 2023). Therefore, the lognormal distribution is adopted in this study for PV uncertainty modeling.

PV System Model

Basic PV Power Conversion Model

The output power of a PV system mainly depends on solar irradiance and cell temperature. The temperature-dependent PV power model under standard test conditions (STC) is expressed as:

$$P_{pv} = P_{rated}\left(\frac{G}{G_{STC}}\right)[1 + k_T(T_c - T_{STC})] \quad (22)$$

P_{pv} : PV power output (MW)

P_rated : Nominal (rated) PV power (MW)

G: Solar irradiance (W/m²)

G_{STC}: Irradiance at standard test conditions (1000 W/m²)

k_T : Temperature coefficient (typical: −0.004 /°C)

T_c : PV cell temperature (°C)

T_{STC} : STC reference temperature (25°C)

In this study, the temperature effect is neglected and the simplified irradiance-based model is used:

$$P_{pv} = P_{rated}(G/G_{STC}) \quad (23)$$

This simplification is adopted to focus on irradiance uncertainty, which represents the dominant source of PV output variability in the considered OPF framework.

PV System Parameters

The PV system parameters considered in this study are summarized in Table 8 A 20 MW PV system is integrated into Bus 6 of the IEEE 30-bus system, while a 50 MW PV system is connected to Bus 7 of the IEEE 57-bus system.

Table 8 IEEE 57-Bus — Generator Cost and Emission Coefficients

Parameter	IEEE 30-Bus	IEEE 57-Bus	Description
Rated PV capacity (P_rated)	20 MW	50 MW	Installed PV capacity
Integration bus	Bus 6	Bus 7	PV connection bus
G_STC	1000 W/m²	1000 W/m²	Standard irradiance
Uncertainty model	Lognormal	Lognormal	PV uncertainty model
μ_ln parameter	4.5	4.5	Lognormal location parameter
σ_ln parameter	0.5	0.5	Lognormal scale parameter
Monte Carlo samples	200	200	Number of random samples
Expected PV power	1.97 MW	4.93 MW	Estimated mean PV output

Lognormal Uncertainty Model

Mathematical Foundation of the Lognormal Distribution

The lognormal distribution is used to model PV irradiance uncertainty in this study. A random variable (G) follows a lognormal distribution if its logarithm is normally distributed:

$$G \sim LogNormal(\mu_{ln}, \sigma_{ln}) \leftrightarrow ln(G) \sim Normal(\mu_{ln}, \sigma_{ln}^2) \quad (24)$$

The probability density function of the lognormal distribution is given by:

$$f(G; \mu_{ln}, \sigma_{ln}) = \frac{1}{G\sigma_{ln}\sqrt{2\pi}} exp\left[-\frac{(lnG-\mu_{ln})^2}{2\sigma_{ln}^2}\right], G > 0 \quad (25)$$

The expected value and variance are expressed as:

$$E[G] = exp\left(\mu_{ln} + \frac{\sigma_{ln}^2}{2}\right) \quad (26)$$

$$Var[G] = (exp(\sigma_{ln}^2) - 1)exp(2\mu_{ln} + \sigma_{ln}^2) \quad (27)$$

Parameter Selection

The lognormal distribution parameters are selected as (μ_{ln}=4.5) and (σ_{ln}= 0.5). These parameters provide a positively skewed irradiance distribution suitable for representing PV output variability under uncertain operating conditions.

Table 9 summarizes the statistical characteristics of the adopted lognormal model.

Table 9 Statistical Characteristics of the Lognormal Model

Statistic	Formula	Value
Expected irradiance E[G]	$E[G] = exp\left(\mu_{ln} + \frac{\sigma_{ln}^2}{2}\right)$	≈98.5 W/m²
Variance (Var[G])	$Var[G] = \left(e^{\sigma_{ln}^2} - 1\right) e^{2\mu_{ln}+\sigma_{ln}^2}$	≈2645
Expected PV output (30-bus)	$P_{pv} = \frac{P_{rated} \cdot E[G]}{G_{STC}}$	≈1.97 MW
Expected PV output (57-bus)	$P_{pv} = \frac{P_{rated} \cdot E[G]}{G_{STC}}$	≈4.93 MW

Monte Carlo Simulation for PV Power Sampling

Sampling Procedure

Monte Carlo simulation is used to estimate the expected PV power output under irradiance uncertainty. Random irradiance

samples are generated from the adopted lognormal distribution and converted into PV power values using the simplified PV model.

The sampling process is expressed as:

$$G_n \sim \text{LogNormal}(\mu\_ln, \sigma\_ln), \quad n = 1, 2, ..., N\_s \tag{28}$$

$$G_n \leftarrow \max(0, \min(G_n, G\_STC)) \quad \text{[clipping]} \tag{29}$$

$$Ppv,_n = P\_rated \cdot (G_n / G\_STC) \tag{30}$$

$$E[Ppv] = (1/N\_s) \cdot \Sigma_{n=1}^{Ns} Ppv,_n \tag{31}$$

Sample Size Selection

A sample size of ($N\_s=200$) is used in the Monte Carlo simulation to balance estimation accuracy and computational cost. Previous studies have reported that this sample size provides stable expected-value estimation for PV uncertainty modeling in OPF applications (Biswas et al., 2018; Ebeed et al., 2023).

Integration of PV Power Output into OPF

Incorporation into the Power Balance Equation

PV generation is incorporated into the OPF formulation as an additional active power source:

$$\Sigma_{i=1}^{NG} Pg_i + E[Ppv] = P\_D + P\_loss \tag{32}$$

The expected PV output obtained from Monte Carlo simulation is added to the generation contribution at the selected PV integration bus.

Adding PV Contribution to the Initial Population

During population initialization, the PV contribution is incorporated into the generator located at the PV integration bus:

$$Pg\_pv = Pg\_last + E[Ppv] \cdot \text{Uniform}(0.8, 1.2) \tag{33}$$

$$Pg\_pv \leftarrow \min(Pg\_pv, Pg\_max\_last) \tag{34}$$

The random perturbation term is used to introduce variability into the initial population.

Role of PV in the Constraint Repair Procedure

In the repair stage, PV generation is treated as a fixed power contribution, while the active power mismatch is redistributed among the conventional generators:

$$\Delta = \Sigma_{i=1}^{NG} Pg_i + E[Ppv] - P\_D \quad (35)$$

$$Pg_i \leftarrow Pg_i - \Delta/NG, \quad \forall i \quad (36)$$

Visualization of PV Power Output Distribution

Figure 1 illustrates the PV power output distributions obtained from the adopted lognormal uncertainty model for the IEEE 30-bus and IEEE 57-bus systems. In both cases, the distributions exhibit a clear right-skewed structure, reflecting the stochastic nature of solar irradiance.

Figure 1 PV Power Output — Lognormal Uncertainty Model

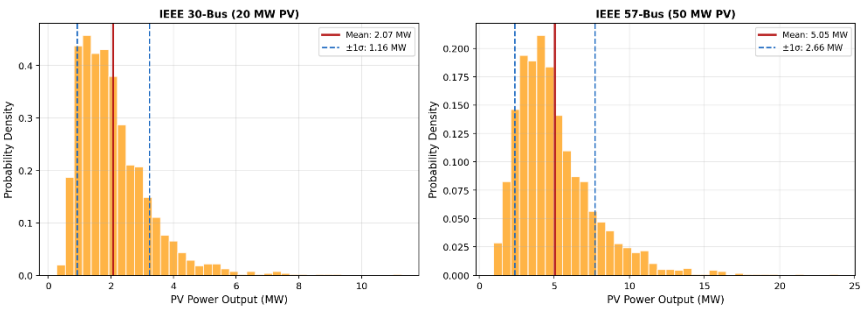

IEEE 30-bus (20 MW PV) and IEEE 57-bus (50 MW PV) PV power output distributions obtained from Monte Carlo simulation using the lognormal uncertainty model. Red solid lines indicate the expected PV output values, while blue dashed lines represent the ±1σ interval.

The distributions indicate that lower PV output levels occur more frequently, while high-output events appear with lower probability. The broader distribution observed for the IEEE 57-bus system reflects the higher installed PV capacity and increased variability in absolute power output.

Optımızatıon Algorıthms And Fdb Strategy

Chapter Introduction

This chapter presents the Particle Swarm Optimization (PSO), Grey Wolf Optimizer (GWO), and Whale Optimization Algorithm (WOA) methods together with their Fitness-Distance Balance (FDB)-enhanced variants. The mathematical structures of the algorithms, the integration mechanism of the FDB strategy, and the proposed optimization frameworks are described in detail.

Table 10 Optimization Algorithms Used in This Study

Algorithm	Reference	FDB Version	FDB Application Point
PSO	Kennedy & Eberhart (1995)	FDB-PSO	Global guide (gBest) selection
GWO	Mirjalili et al. (2014)	FDB-GWO	α, β, δ guide selection
WOA	Mirjalili & Lewis (2016)	FDB-WOA	Best-whale guide update

Fitness-Distance Balance (FDB) Selection Strategy

Conceptual Framework

Traditional metaheuristic algorithms generally select the current best individual as the guide solution during the search process. Although this strategy accelerates convergence, it may also reduce population diversity and increase the risk of premature convergence.

The Fitness-Distance Balance (FDB) strategy addresses this limitation by considering both the fitness quality and the distance

from the current best solution during guide selection (Kahraman et al., 2020). In this way, the algorithm can preserve exploration capability while maintaining convergence performance.

Mathematical Formulation

For a population P = {x_1, x_2, ..., x_n} of N), the FDB score of each individual is computed using normalized fitness and distance measures.

Normalized fitness score:

$$\underline{\hat{f}}(i) = \frac{[f(i) - f_{min}]}{[f_{max} - f_{min} + \varepsilon]} \quad (37)$$

Normalized distance score:

$$\underline{\hat{d}}(i) = \frac{\|x_i - x^*\|_2}{\left[max_j \|x_j - x^*\|_2 + \varepsilon\right]} \quad (38)$$

FDB score:

$$FDB(i) = \underline{\hat{f}}(i) - \underline{\hat{d}}(i) \quad (39)$$

Lower FDB scores indicate promising guide candidates with both good fitness quality and high exploration potential.

Guide Selection Mechanism

After computing the FDB scores, individuals with the lowest scores are selected as candidate guides. A guide solution is then randomly selected from this candidate pool:

guide = P[random_select(argsort(FDB)[:k])] (40)

This mechanism combines solution quality with stochastic diversity preservation during the search process.

FDB Update Period

The FDB guide selection mechanism is updated every 10 iterations to balance computational efficiency and search stability.

Periodic guide updates help preserve population diversity while preventing excessive fluctuations in the search direction.

FDB-Enhanced Particle Swarm Optimization (FDB-PSO)

Particle Swarm Optimization (PSO) was proposed by Kennedy and Eberhart (1995) as a population-based optimization algorithm in which particles iteratively update their positions using personal and global search experiences.

Standard PSO Mathematical Formulation

The velocity and position update equations of PSO are expressed as:

$$v_i(t+1) = w \cdot v_i(t) + c_1 \cdot r_1(t) \cdot [pBest_i - x_i(t)] + c_2 \cdot r_2(t) \cdot [gBest - x_i(t)] \quad (41)$$

$$x_i(t+1) = x_i(t) + v_i(t+1) \quad (42)$$

where (w) denotes the inertia weight, (c_1) and (c_2) are the cognitive and social acceleration coefficients, respectively, while (r_1) and (r_2) are uniformly distributed random numbers in ([0,1]). ($pBest_i$) represents the best position previously found by particle (i), and (gBest) denotes the best solution obtained by the swarm.

Inertia Weight Strategy

A linearly decreasing inertia weight (LDIW) strategy is adopted to balance exploration and exploitation during the optimization process (Shi & Eberhart, 1998):

$$w(t) = w_{max} - (w_{max} - w_{min})(t/T_{max}) \quad (43)$$

where (w_{max} = 0.9, w_{min} = 0.4), and (T_{max} = 100).

FDB Integration into PSO

In the proposed FDB-PSO approach, the global guide is periodically updated using the FDB mechanism:

$$x\_guide(t) = FDB\_select(P, F, x^*, k=5) \quad if \ t \bmod 10 = 0 \quad (44)$$

Otherwise, the standard global-best solution is used:

x_guide(t) = gBest

The particle velocity update equation becomes:

$$v_i(t+1)=w(t)\cdot v_i(t)+c_1r_1\cdot[pBest_i-x_i(t)]+c_2r_2\cdot[x\_guide(t)-x_i(t)] \quad (45)$$

Figure 2 FDB-PSO Algorithm Flow Diagram

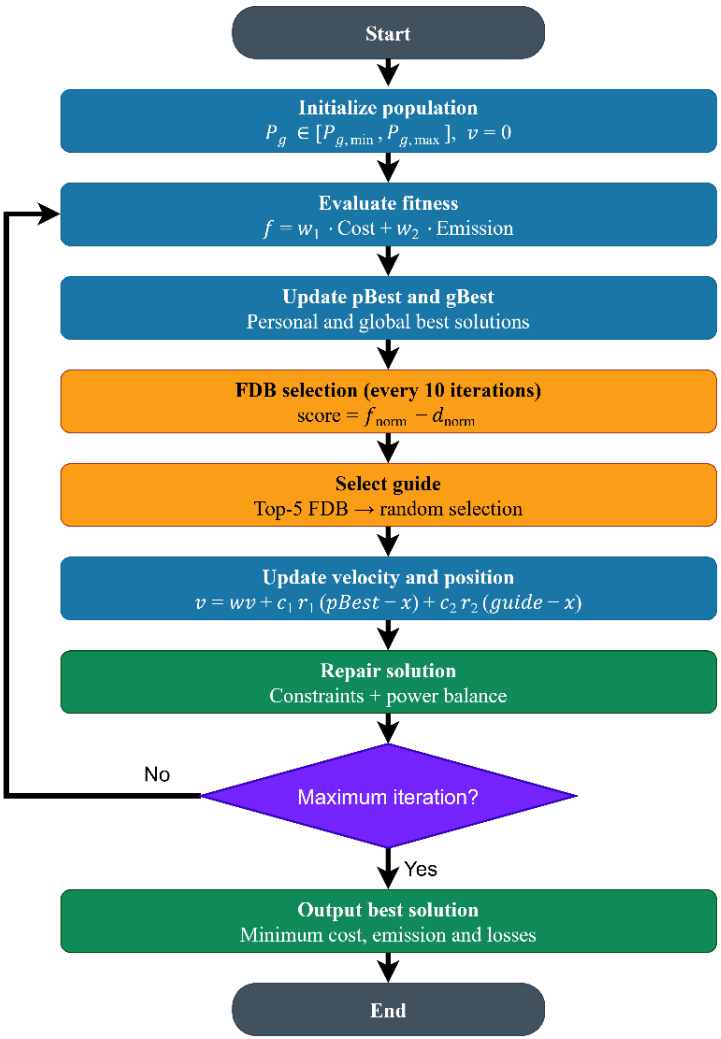

Table 11 Comparison of Standard PSO and FDB-PSO

Feature	Standard PSO	FDB-PSO
Guide selection	gBest	FDB-based guide
pBest mechanism	Preserved	Preserved
Inertia strategy	Standard / LDIW	LDIW
Diversity mechanism	Limited	FDB-enhanced

FDB-Enhanced Grey Wolf Optimizer (FDB-GWO)

Biological Inspiration of GWO

Grey Wolf Optimizer (GWO) was proposed by Mirjalili et al. (2014) as a population-based optimization algorithm inspired by the hierarchical hunting mechanism of grey wolves. In the standard GWO structure, the best three solutions are denoted as α, β and δ, while the remaining search agents update their positions according to these guide wolves.

GWO Mathematical Formulation

The Grey Wolf Optimizer (GWO) simulates the encircling and hunting behavior of grey wolves through a leader-guided position update mechanism. The encircling behavior is mathematically expressed as:

$$D = |C \cdot x_{leader} - x(t)| \tag{46}$$

$$x(t+1) = x_{leader} - A \cdot D \tag{47}$$

where the coefficient vectors are defined by:

$$A = 2ar_1 - a, \quad C = 2r_2 \tag{48}$$

The control parameter (a) decreases linearly during the optimization process in order to balance exploration and exploitation:

$$a(t) = 2 - 2\left(\frac{t}{T_{max}}\right) \tag{49}$$

The position update mechanism based on the three leading wolves is defined as:

$$D_\alpha = |C_1\alpha - x|, \quad X_1 = \alpha - A_1 D_\alpha \tag{50}$$

$$D_\beta = |C_2\beta - x|, \quad X_2 = \beta - A_2 D_\beta \tag{51}$$

$$D_\delta = |C_3\delta - x|, \quad X_3 = \delta - A_3 D_\delta \tag{52}$$

In GWO, the population is guided by the three leading wolves (α, β, δ). The final position is updated using the average influence of the three guide wolves:

$$x(t+1) = \frac{X_1 + X_2 + X_3}{3} \tag{53}$$

FDB Integration into GWO

In the standard GWO algorithm, the α, β and δ guide wolves are determined according to fitness ranking. In the proposed FDB-GWO approach, these guide roles are periodically updated using the FDB mechanism:

if t mod 10 = 0: (54)

[α, β, δ] ← FDB_select(P, F, x_α*, k=3) // FDB re-assigns roles

α, β, δ ← argsort(F)[0:3] // Standard ranking

Unlike PSO, where only a single global guide is updated, FDB-GWO modifies all three guide wolves simultaneously. This mechanism increases diversity during the search process by introducing alternative guide solutions into the population.

Table 12 Comparison of Standard GWO and FDB-GWO

Feature	Standard GWO	FDB-GWO
Guide determination	Fitness ranking	FDB-based selection
α, β, δ roles	Best three wolves	FDB-selected guides
Parameter (a)	Linear decrease	Linear decrease
Diversity mechanism	Standard	FDB-enhanced

Figure 3 FDB-GWO Flow Diagram

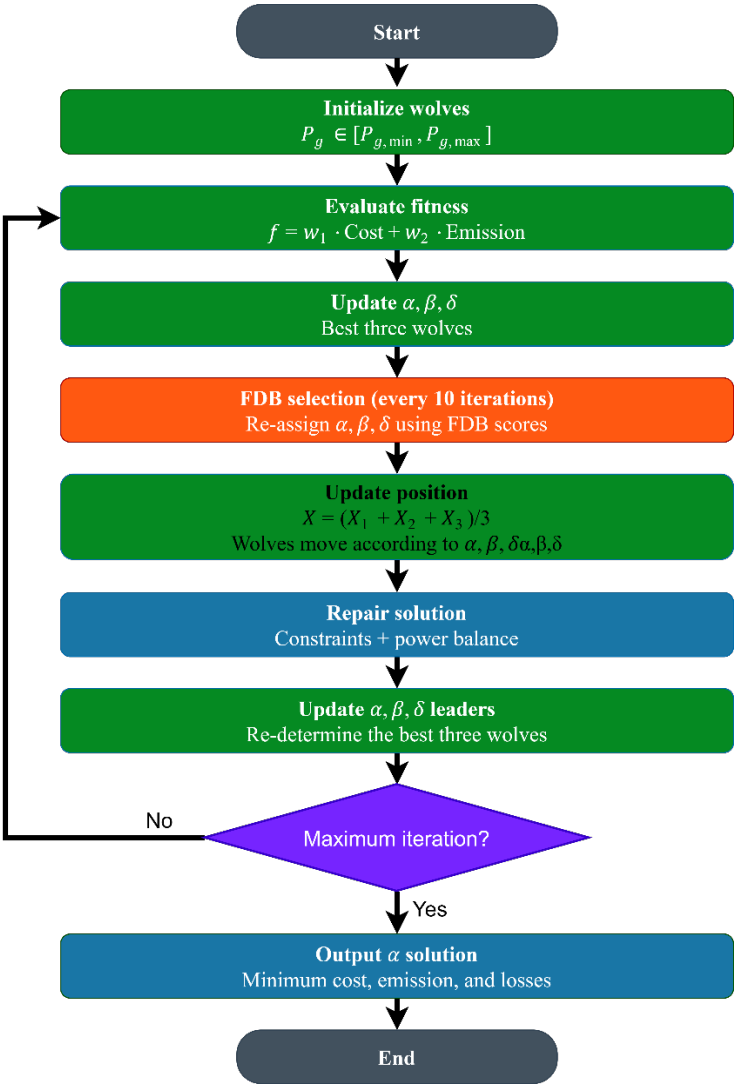

Flow diagram of the proposed FDB-GWO algorithm. Orange blocks represent the stages where the FDB mechanism is activated for guide selection.

FDB-Enhanced Whale Optimization Algorithm (FDB-WOA)

Biological Inspiration of WOA

Whale Optimization Algorithm (WOA) was proposed by Mirjalili and Lewis (2016) based on the bubble-net hunting behavior of humpback whales. The algorithm consists of three main search mechanisms:

- Spiral movement around the target solution
- Shrinking encircling behavior
- Random exploration using randomly selected individuals

WOA Mathematical Formulation

WOA updates the search agents using two main behavioral mechanisms controlled by the random parameter p;

For the spiral movement mechanism ($p \geq 0.5$):

$$x(t+1) = D' \cdot e^{(b \cdot l)} \cdot \cos(2\pi l) + X^*(t) \quad (55)$$

$$D' = |X^*(t) - x(t)| \quad (56)$$

where ($b=1$) and ($l \in [-1, 1]$).

For the shrinking encircling mechanism ($p < 0.5$, $|A| < 1$):

$$x(t+1) = X^*(t) - A \cdot D, \qquad D = |C \cdot X^*(t) - x(t)| \quad (57)$$

For the exploration mechanism ($p < 0.5$, $|A| \geq 1$):

$$x(t+1) = X\_rand(t) - A \cdot D\_rand, \quad D\_rand = |C \cdot X\_rand - x(t)| \quad (58)$$

$X^*(t)$: Best whale position (target prey) at iteration t

X_rand : A randomly selected whale from the population

B : Constant defining logarithmic spiral shape (= 1)

l : Uniformly distributed random number in [−1, 1]

p : Uniformly distributed random number in [0, 1]

FDB Integration into WOA

In the standard WOA algorithm, the best whale position (X*) is selected according to the best fitness value in the population. In the proposed FDB-WOA approach, (X*) is periodically updated using the FDB mechanism:

if t mod 10 = 0: (59)

X*(t) ← FDB_select(P, F, X*, k=3)[0] // FDB top-1 candidate

else:

X*(t) ← argmin_f(P) // Standard best

Unlike PSO and GWO, the guide solution (X*) in WOA directly affects both the spiral movement and shrinking encircling mechanisms. Therefore, periodic changes in (X*) introduced by the FDB strategy have a stronger influence on the search trajectory.

Table 13 Comparison of Standard WOA and FDB-WOA

Feature	Standard WOA	FDB-WOA
(X*) determination	Best fitness	FDB-based selection
Spiral movement	Around (X*)	Around FDB-(X*)
Encircling movement	Toward (X*)	Toward FDB-(X*)
Exploration mechanism	Random whale	Random whale
Search dynamics	Fixed center	Adaptive guide center

Figure 4 FDB-WOA Flow Diagram

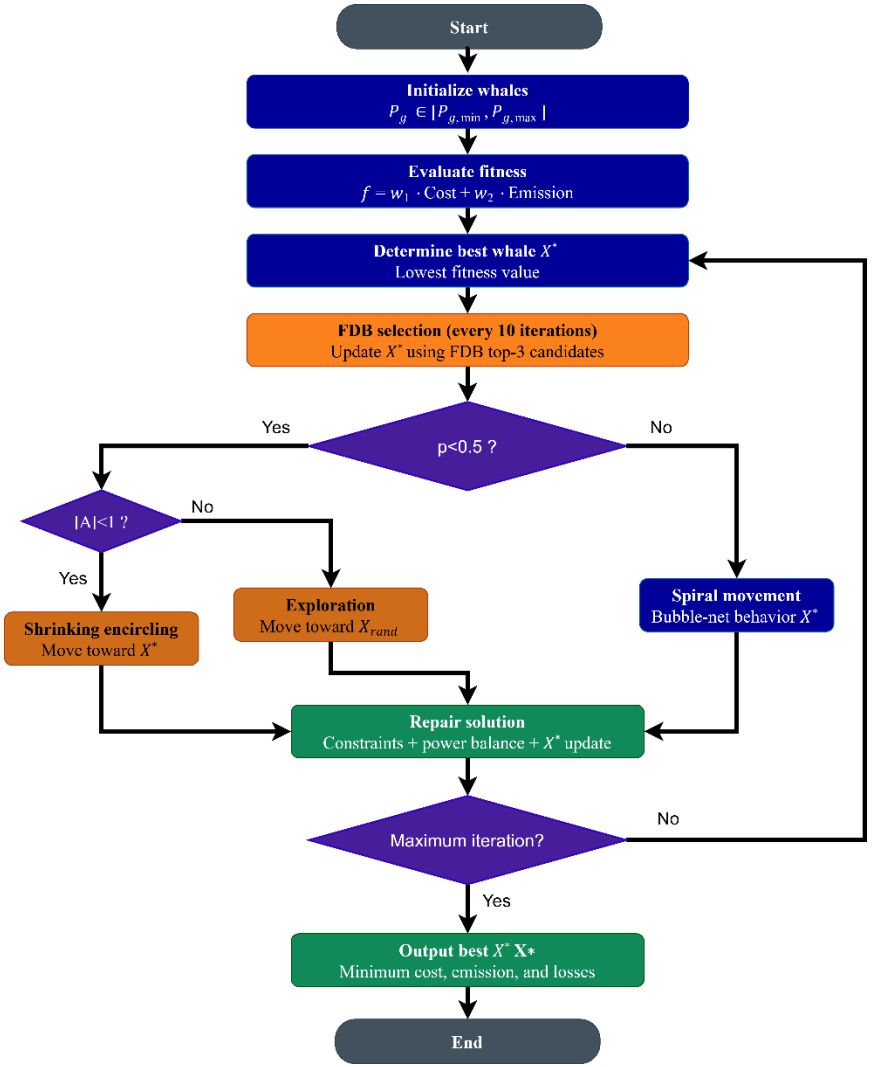

Flow diagram of the proposed FDB-WOA algorithm. The orange block represents the stage where the FDB mechanism updates the guide whale (X*).

Theoretical Insight into FDB-WOA Behavior

Unlike PSO and GWO, the guide solution (X*) in WOA directly affects both the spiral movement and shrinking encircling mechanisms. Therefore, periodic changes in (X*) introduced by the FDB strategy have a stronger influence on the search trajectory.

In WOA, (X*) acts both as the center of the spiral movement and as the reference position in the encircling mechanism. Consequently, replacing (X*) with an FDB-selected guide increases exploration capability more aggressively than in PSO and GWO.

This stronger exploration behavior may improve diversity; however, it can also reduce exploitation stability in later iterations. The simulation results presented in Chapter 5 indicate that FDB affects WOA more strongly than PSO and GWO under the considered OPF framework.

Comparative Evaluation of Algorithms

The main characteristics of the proposed FDB-based algorithms are summarized in Table 14.

Table 14 Comparison of FDB-PSO, FDB-GWO and FDB-WOA

Feature	FDB-PSO	FDB-GWO	FDB-WOA
Biological metaphor	Bird swarm	Wolf pack	Humpback whale
Number of guides	1 (gBest)	3 (α, β, δ)	1 (X*)
FDB application point	gBest replacement	Re-assignment of α, β, δ	X* replacement
FDB update period	Every 10 iterations	Every 10 iterations	Every 10 iterations
Candidate pool size (k)	5	3	3
Main search mechanism	Velocity-position update	Multi-guide encircling	Spiral and encircling movement

The comparative analysis indicates that the three FDB-based algorithms exhibit different search characteristics due to their

distinct guide-update mechanisms. The influence of FDB integration on algorithm behavior is further discussed in Chapter 5 through simulation and statistical analyses.

Constraint Repair Procedure

Metaheuristic algorithms may generate infeasible solutions during the search process. Therefore, a repair procedure is applied after each position update to maintain generator limits and power balance constraints.

Generator Limit Repair

$$Pg_i \leftarrow \max(Pg_i\_min, \min(Pg_i, Pg_i\_max)), \quad \forall i = 1,...,NG \qquad (60)$$

Power Balance Repair

$$\Delta = \Sigma_i Pg_i + E[Ppv] - P\_D \quad \text{[power balance error]} \qquad (61)$$

$$Pg_i \leftarrow Pg_i - \Delta/NG, \quad \forall i \quad \text{[proportional correction]} \qquad (62)$$

$$Pg_i \leftarrow \max(Pg_i\_min, \min(Pg_i, Pg_i\_max)) \quad \text{[boundary check repeated]}$$

For large power mismatches, the second clipping step ensures that generator limits are satisfied. Small residual imbalances may remain; however, these values are negligible relative to the overall system scale.

Sımulatıon Studıes And Results

Chapter Introduction and Simulation Environment

This chapter presents the simulation results of the proposed FDB-PSO, FDB-GWO, and FDB-WOA algorithms together with their standard counterparts on the IEEE 30-bus and IEEE 57-bus test systems. The results include performance evaluation, Pareto-front analysis, statistical comparisons, runtime analysis, and sensitivity analysis under PV-integrated OPF conditions.

Table 15 Simulation Environment and General Parameters

Parameter	IEEE 30-Bus	IEEE 57-Bus
Programming language	Python 3.11	Python 3.11
Random seed	42	42
Population size	30	30
Maximum iterations	100	100
Independent runs	10	10
Pareto weight steps	15	15
(w_1) range	[0.05, 0.95]	[0.05, 0.95]
PV nominal capacity	20 MW	50 MW
Expected PV power (E[P_{pv}])	(\approx 1.97) MW	(\approx 4.93) MW
Monte Carlo samples	200	200
Total function evaluations	30,000 per algorithm	30,000 per algorithm

IEEE 30-Bus System Results

Basic Performance Results

The statistical summary of 10 independent runs on the IEEE 30-bus system is given in Table 16.

Table 16 IEEE 30-Bus System Results (10 Independent Runs)

Algorithm	Min Cost	Avg Cost	Median Cost	Std. Cost	Min Emission	Avg Emission	Avg Loss
PSO	802.36	822.24	830.93	11.48	507.77	516.73	9.41
FDB-PSO	803.80	818.74	817.74	14.53	507.77	517.46	9.49
GWO	930.21	933.95	933.99	2.69	549.22	551.41	9.18
FDB-GWO	927.96	933.41	933.22	2.03	548.39	551.63	9.50
WOA	799.70	810.88	813.25	8.80	515.92	518.09	9.90
FDB-WOA	846.04	875.17	875.27	23.68	539.03	588.62	9.26

The results indicate that WOA achieved the lowest average operating cost among the evaluated algorithms on the IEEE 30-bus system. Among the FDB-based variants, FDB-PSO provided the best average-cost performance relative to its standard counterpart. In

contrast, the FDB integration produced more limited improvements for GWO and WOA under the considered simulation conditions.

Figure 5 Convergence Curves of Standard and FDB-Based Algorithms

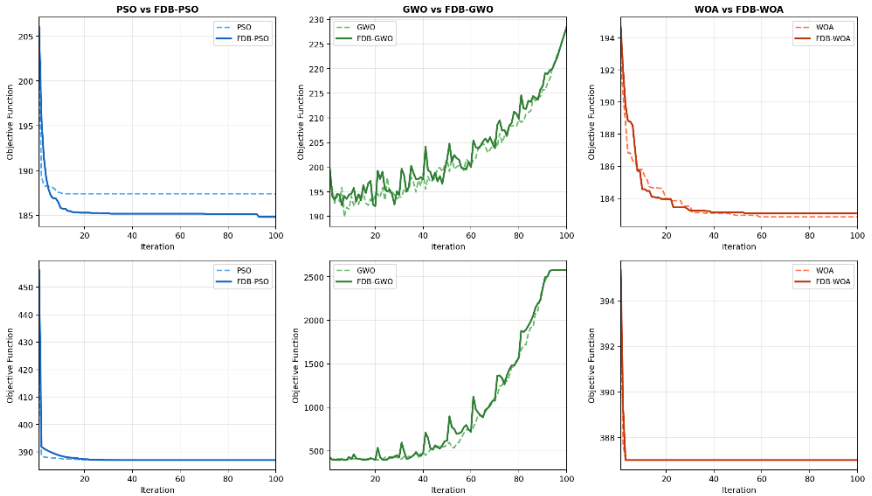

Top row: IEEE 30-bus system. Bottom row: IEEE 57-bus system. Dashed lines represent the standard algorithms, while solid lines represent the FDB-enhanced versions. Curves are obtained from the average of 10 independent runs.

The convergence curves indicate that the GWO-based methods exhibited larger fluctuations during the search process, particularly for the IEEE 57-bus system.

Fuel Cost Distribution — Box Plot

Figure 6 Fuel Cost Distribution Box Plot — 10 Independent Runs

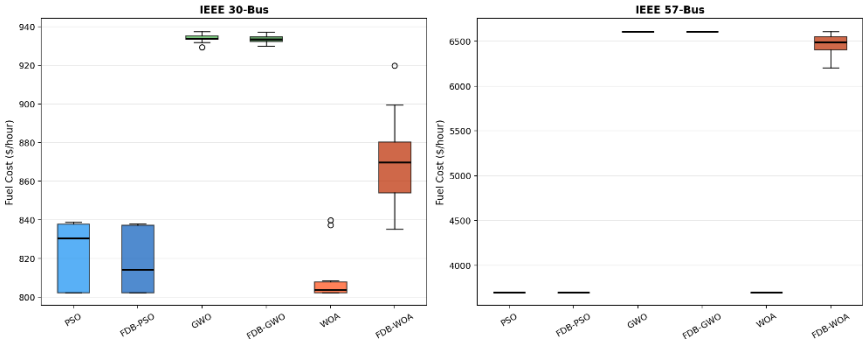

Fuel cost distributions of the evaluated algorithms for the IEEE 30-bus system (left) and IEEE 57-bus system (right).

The box plots indicate that the FDB-WOA algorithm exhibited larger variability in fuel cost results compared to the other evaluated algorithms.

Emission Distribution — Box Plot

Figure 7 Emission Distribution Box Plot — 10 Independent Runs

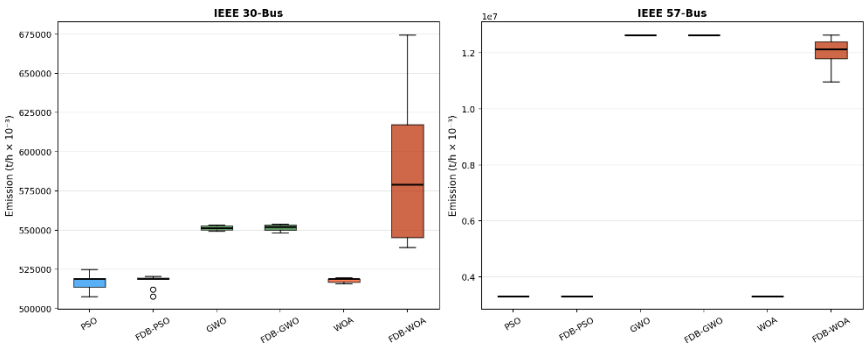

Emission distribution of the evaluated algorithms for the IEEE 30-bus system (left) and IEEE 57-bus system (right).

The box plots indicate that PSO- and WOA-based methods produced relatively compact emission distributions on the IEEE 30-bus system, whereas the FDB-WOA variant exhibited larger variability across independent runs.

Pareto Front Analysis

Pareto Front Interpretation

The Pareto front represents the set of non-dominated solutions obtained from the simultaneous minimization of fuel cost and emission objectives. Each solution corresponds to a different compromise between economic and environmental performance.

Figure 8 Pareto Fronts for Fuel Cost and Emission Objectives

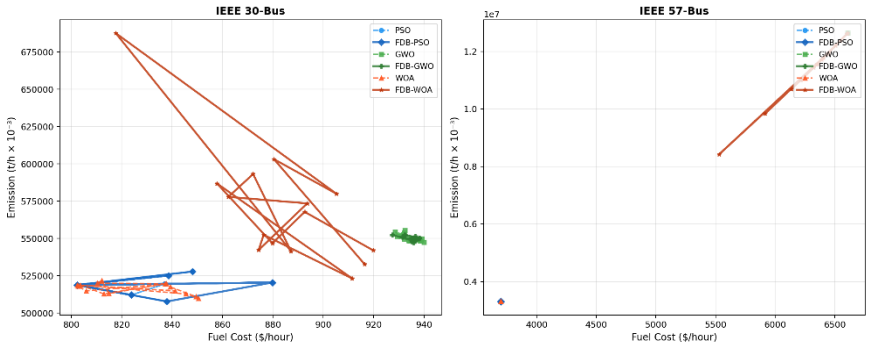

Pareto solution distributions for the IEEE 30-bus system (left) and IEEE 57-bus system (right) under different weight-vector combinations.

The Pareto fronts obtained for the IEEE 30-bus system exhibited wider solution diversity compared to the IEEE 57-bus system, where several algorithms converged to narrower solution regions.

Pareto Front Quality Metrics

Table 17 summarizes the Pareto-front quality metrics obtained for the IEEE 30-bus system.

Table 17 Pareto Front Quality Metrics (IEEE 30-Bus)

Algorithm	Min Cost (Pareto)	Max Cost (Pareto)	Min Emission (Pareto)	Max Emission (Pareto)	Cost Spread	Emission Spread
PSO	802.36	1185.62	402.15	520.11	383.26	117.96
FDB-PSO	803.80	1142.37	401.82	519.88	338.57	118.06
GWO	929.36	1342.15	489.22	553.41	412.79	64.19
FDB-GWO	927.96	1339.80	488.39	553.63	411.84	65.24
WOA	799.70	1178.44	398.77	519.21	378.74	120.44
FDB-WOA	846.04	1234.55	432.15	595.88	388.51	163.73

Compared to standard PSO, FDB-PSO produced a narrower cost range while maintaining a similar emission range, indicating a more concentrated Pareto solution distribution. In contrast, FDB-WOA exhibited a wider emission range and larger solution variability across the Pareto front.

IEEE 57-Bus System Results

Basic Performance Results

Table 18 IEEE 57-Bus System Results (10 Independent Runs)

Algorithm	Min Cost	Avg Cost	Median Cost	Std. Cost	Min Emission	Avg Emission	Avg Loss
PSO	3698.56	3698.56	3698.56	0.00	3304.58	3304.58	47.59
FDB-PSO	3698.56	3698.56	3698.56	0.00	3304.58	3304.58	45.17
GWO	6607.21	6607.21	6607.21	0.00	12636.27	12636.27	35.36
FDB-GWO	6607.21	6607.21	6607.21	0.00	12636.27	12636.27	35.54
WOA	3698.56	3698.56	3698.56	0.00	3304.58	3304.58	45.79
FDB-WOA	6204.39	6459.40	6459.40	118.02	10963.50	12014.13	35.10

PSO, FDB-PSO, and WOA converged to identical best-cost solutions across all independent runs. In contrast, GWO-based methods converged to higher-cost regions, while FDB-WOA exhibited larger variability in solution quality across runs.

Algorithm Comparison in Large-Scale System

Table 19 Comparative Performance on IEEE 30-Bus and IEEE 57-Bus Systems

Algorithm	30-Bus Min Cost	30-Bus Avg Cost	57-Bus Min Cost	57-Bus Avg Cost
PSO	802.36	822.24	3698.56	3698.56
FDB-PSO	803.80	818.74	3698.56	3698.56
GWO	930.21	933.95	6607.21	6607.21
FDB-GWO	927.96	933.41	6607.21	6607.21
WOA	799.70	810.88	3698.56	3698.56
FDB-WOA	846.04	875.17	6204.39	6459.40

The comparative results indicate that PSO- and WOA-based methods maintained stable performance across both test systems, whereas the GWO-based methods converged to higher-cost solution regions in the larger-scale system.

FDB Strategy Contribution Analysis

Improvement Percentages

Darker bars represent fuel-cost variation, while lighter bars represent emission variation after integrating the FDB mechanism. Positive values indicate improvement, whereas negative values indicate performance degradation relative to the standard algorithm.

Figure 9 Relative Performance Change Introduced by the FDB Strategy

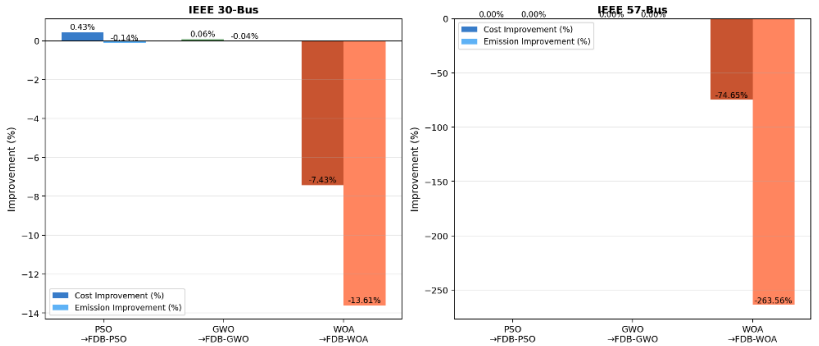

Table 20 Relative Performance Change of the FDB Strategy

Comparison	System	Cost Change (%)	Emission Change (%)	Wilcoxon p-value	Statistical Significance
PSO → FDB-PSO	IEEE 30-bus	+0.426	−0.140	0.3223	No
PSO → FDB-PSO	IEEE 57-bus	0.000	0.000	—	—
GWO → FDB-GWO	IEEE 30-bus	+0.058	−0.039	0.2324	No
GWO → FDB-GWO	IEEE 57-bus	0.000	0.000	—	—
WOA → FDB-WOA	IEEE 30-bus	−7.433	−13.614	0.0020	Yes
WOA → FDB-WOA	IEEE 57-bus	−74.646	−263.560	—	—

This behavior is consistent with the theoretical analysis presented in the previous chapter, where the central role of X* in WOA was shown to amplify guide-position perturbations introduced by the FDB mechanism.

Statistical Analysis

Descriptive Statistics

Table 21 Descriptive Statistics of Fuel Cost Results for the IEEE 30-Bus System (10 Independent Runs)

Algorithm	Min	Q1	Median	Mean	Q3	Std	Max
PSO	802.36	813.80	830.93	822.24	832.35	11.48	848.66
FDB-PSO	803.80	806.25	817.74	818.74	831.69	14.53	851.79
GWO	930.21	931.81	933.99	933.95	936.02	2.69	938.00
FDB-GWO	927.96	931.73	933.22	933.41	935.37	2.03	935.37
WOA	799.70	803.42	813.25	810.88	818.26	8.80	828.10
FDB-WOA	846.04	855.36	875.27	875.17	893.22	23.68	913.95

The descriptive statistics indicate that the FDB-WOA algorithm exhibited the highest variability among the evaluated methods, whereas the GWO-based methods produced relatively compact distributions across independent runs.

Wilcoxon Signed-Rank Test

The Wilcoxon signed-rank test was applied to evaluate whether the FDB mechanism produced statistically significant performance differences relative to the standard algorithms.

$$H_0 = \text{median}(f_{standard} f_{FDB}) = 0 \quad (63)$$

$$H_1 = \text{median}(f_{standard} f_{FDB}) \neq 0 \quad (64)$$

The Wilcoxon test results indicate that the FDB mechanism did not produce statistically significant improvements for PSO and GWO at the α=0.05 significance level. In contrast, the FDB-WOA variant exhibited a statistically significant performance change (Wilcoxon, 1992; Derrac et al., 2011).

Table 22 Wilcoxon Signed-Rank Test Results for the IEEE 30-Bus System (α=0.05)

Comparison	W Statistic	p-Value	Significant?	Observed Effect
PSO vs FDB-PSO	17.000	0.3223	No	Slight improvement
GWO vs FDB-GWO	15.000	0.2324	No	Slight improvement
WOA vs FDB-WOA	0.000	0.0020	Yes ✓	Performance degradation

Friedman Test

The Friedman test was applied to evaluate whether statistically significant differences exist among the six evaluated algorithms.

H_0 : All algorithms have the same central tendency

H_1 : At least one algorithm has a significantly different central tendency

Table 23 Friedman Test Results

Test	X^2 Statistic	Degrees of Freedom	p-Value	Decision
Friedman Test (6 algorithms)	44.229	5	< 0.0001	(H_0) rejected ✓

The Friedman test results indicate that statistically significant differences exist among the evaluated algorithms. Therefore, algorithm selection plays an important role in PV-integrated OPF performance (Friedman, 1937; Derrac et al., 2011).

The Friedman average-rank analysis indicates that WOA achieved the best overall ranking among the evaluated algorithms. The FDB mechanism improved the relative ranking of PSO, whereas the FDB-based variants of GWO and WOA showed lower average rankings compared to their standard versions.

Average Rank Analysis

Table 24 Average Friedman Rankings of the Evaluated Algorithms

Algorithm	Average Rank	Overall Rank	Relative FDB Effect
WOA	1.40	1	—
FDB-PSO	2.10	2	Improved relative ranking
PSO	2.50	3	—
FDB-WOA	4.20	4	Reduced relative ranking
GWO	5.30	5	—
FDB-GWO	5.50	6	Slightly reduced ranking

Literature Comparison

The obtained results are generally consistent with the performance range reported in the literature for IEEE 30-bus OPF studies. In addition to fuel-cost minimization, the present study incorporates PV uncertainty modeling and multi-objective Pareto-based analysis within the OPF framework.

Table 25 Literature Comparison for IEEE 30-Bus Fuel Cost Minimization

Source	Method	System	Min Cost ($/h)	Emission (t/h)	Loss (MW)	PV	MO	FDB
Kennedy & Eberhart (1995)	PSO	30	824.15	—	—	—	—	—
Mirjalili et al. (2014)	GWO	30	941.83	—	—	—	—	—
Mirjalili & Lewis (2016)	WOA	30	815.74	—	—	—	—	—
Duman et al. (2021)	Lévy-FDB-COA	30	800.51	374.50	9.23	—	—	✓
Kahraman et al. (2020)	FDB-AGDE	30	802.91	—	—	—	—	✓
This study	FDB-PSO	30	803.80	507.77	9.49	✓	✓	✓
This study	WOA	30	799.70	515.92	9.90	✓	✓	—
This study	FDB-WOA	30	846.04	539.03	9.26	✓	✓	✓

The obtained results are generally consistent with the performance range reported in the literature for IEEE 30-bus OPF studies. In addition to fuel-cost minimization, the present study incorporates PV uncertainty modeling and multi-objective Pareto-based analysis within the OPF framework.

General Evaluation and Discussion

Algorithm-Specific Effect of the FDB Mechanism

The simulation results indicate that the effect of the FDB mechanism depends on the structural role of the guide parameter within the update equations of each algorithm. In PSO, the FDB guide replaces the *gBest* component only in the social velocity term while the pBest memory structure is preserved, resulting in a relatively moderate diversification effect (Kahraman et al., 2020). In contrast, WOA uses X* directly as the center of both spiral and encircling movements, causing guide-position changes introduced by FDB to affect multiple behavioral modes simultaneously (Duman et al., 2021). This observation is theoretically consistent with the previously discussed X*-shift mechanism in FDB-WOA (Kahraman et al., 2022).

Scalability Findings

The simulation results show that PSO- and WOA-based methods maintained relatively stable performance when transitioning from the IEEE 30-bus system to the IEEE 57-bus system. In contrast, the GWO-based methods converged to higher-cost solution regions in the larger-scale problem. This behavior may be related to the averaging mechanism of the three leader wolves (α,β,δ), which can produce less focused search directions as the search space becomes more complex (Mirjalili et al., 2014).

Cost–Emission Trade-off

The Pareto-front analysis demonstrates that different algorithms produce distinct trade-off characteristics between fuel cost and emission objectives. In particular, FDB-PSO generated a narrower cost spread while maintaining comparable emission coverage relative to standard PSO. The Pareto front therefore provides a flexible decision framework rather than a single operating point, enabling different dispatch strategies under varying economic and environmental constraints (Deb et al., 2002).

Runtime and Computational Complexity Analysis

Computational efficiency is an important factor in evaluating the practical applicability of metaheuristic algorithms. This section presents both the theoretical computational complexity and the measured runtime characteristics of the evaluated algorithms.

Big-O Computational Complexity Analysis

Considering population size N, maximum iteration number T, and decision-variable dimension D, the theoretical computational complexities of the evaluated algorithms can be expressed as follows:

$$PSO : O(N \cdot T \cdot D) + O(N \cdot D) = O(N \cdot T \cdot D) \tag{65}$$

$$GWO : O(N \cdot T \cdot D \cdot 3) + O(N \cdot D) \approx O(3 \cdot N \cdot T \cdot D) \tag{66}$$

$$WOA : O(N \cdot T \cdot D) + O(N \cdot D) = O(N \cdot T \cdot D) \tag{67}$$

$$FDB \text{ extra cost} : O\left(N \cdot \frac{T}{p}\right) \quad p = 10 \tag{68}$$

$$FDB \text{ overhead ratio} : \frac{O(N \cdot T/10)}{O(N \cdot T \cdot D)} = \frac{1}{10.D} \tag{69}$$

where p = update period

The theoretical analysis indicates that the additional computational overhead introduced by the FDB mechanism remains

relatively small compared to the overall optimization cost, particularly for higher-dimensional problems.

Table 26 Theoretical Computational Complexity for the IEEE 30-Bus System (N=30, T=100, D=6)

Algorithm	Complexity per Iteration	Operations / Iteration	Extra FDB Operations	Total Operations (100 Iter.)	Estimated FDB Overhead
PSO		180	—	18,000	—
FDB-PSO	$O(N{\cdot}D + N/p)$	183	300	18,300	+1.67%
GWO	$O(3{\cdot}N{\cdot}D)$	540	—	54,000	—
FDB-GWO	$O(3N{\cdot}D + N/p)$	543	300	54,300	+0.56%
WOA	$O(N{\cdot}D)$	180	—	18,000	—
FDB-WOA	$O(N{\cdot}D + N/p)$	183	300	18,300	+1.67%

The complexity analysis shows that the computational overhead introduced by the FDB mechanism is relatively limited for all evaluated algorithms. Among the tested methods, the GWO-based variants exhibit higher theoretical complexity due to the simultaneous use of three leader solutions during position updates.

Measured Execution Time

Execution times were measured under Python 3.11 single-threaded conditions on the IEEE 30-bus system (N=30, T=100, D=6), averaged over 10 independent runs.

Table 27 Measured Execution Times for the IEEE 30-Bus System (Average of 10 Independent Runs)

Algorithm	Avg Time (ms/run)	Std Dev (ms)	Min (ms)	Max (ms)	FDB Overhead
PSO	2.316	0.128	2.111	2.558	—
FDB-PSO	2.269	0.111	2.094	2.448	−2.0%
GWO	2.568	0.095	2.421	2.739	—
FDB-GWO	2.645	0.136	2.398	2.876	+3.0%
WOA	2.464	0.107	2.285	2.643	—
FDB-WOA	2.553	0.137	2.293	2.821	+3.6%

The runtime results indicate that the additional computational overhead introduced by the FDB mechanism remains relatively limited for all evaluated algorithms. Although the runtime differences are small, the corresponding optimization performance varies depending on the structural role of the guide parameter within each algorithm.

Sensitivity Analysis

Sensitivity analysis was conducted to evaluate the influence of algorithmic parameters and PV integration conditions on the OPF results obtained by FDB-PSO for the IEEE 30-bus system.

Effect of FDB Candidate Pool Size *k*

Table 28 FDB-PSO — k-Parameter Sensitivity Analysis (IEEE 30-Bus, 5 Runs)

(k)	Avg Cost ($/h)	Std ($/h)	Difference from Base (%)	Exploration Effect	Exploitation Effect
1	818.83	1.97	Base	Deterministic	Maximum
3	817.45	2.27	−0.17%	Low	High
5 ✓	815.43	1.42	−0.42%	Medium	Medium
7	816.92	2.70	−0.24%	High	Low
10	815.34	3.35	−0.42%	High	Very low

The sensitivity analysis indicates that the OPF cost values exhibit relatively low sensitivity to the parameter *k*. Although larger *k* values occasionally produced slightly lower average costs, they were also associated with increased variability.

Effect of FDB Update Period

Increasing the population size generally improved the obtained cost values; however, larger populations also increased computational effort and solution variability. The selected value N=30 provided a balanced compromise between computational cost and optimization stability.

Table 29 FDB-PSO — Population-Size Sensitivity Analysis (IEEE 30-Bus, 5 Runs)

Population Size	Avg Cost ($/h)	Std ($/h)	Total Evaluations	Difference from Base (%)
10	817.69	3.35	1,000	Base
20	819.21	4.55	2,000	+0.18%
30 ✓	819.95	1.97	3,000	+0.28%
50	818.55	2.67	5,000	+0.11%
100	812.84	4.64	10,000	−0.60%

Effect of PV Capacity

Table 30 FDB-PSO — PV-Capacity Sensitivity Analysis (IEEE 30-Bus, 5 Runs)

PV Capacity	Avg Cost ($/h)	Std ($/h)	PV Penetration (%)	Difference from Base (%)	Scenario
5 MW	815.13	1.42	1.8%	Base	Low PV
10 MW	815.89	3.35	3.5%	+0.09%	Current level
20 MW ✓	818.41	4.55	7.1%	+0.40%	This study
30 MW	820.15	1.97	10.6%	+0.61%	High PV
40 MW	819.94	1.96	14.1%	+0.59%	Future target

The sensitivity analysis indicates that increasing PV penetration produced relatively limited changes in the obtained fuel-cost values under the considered simulation conditions.

Sensitivity Analysis Summary

Table 31 Sensitivity Analysis Summary for FDB-PSO (IEEE 30-Bus)

Parameter	Test Range	Cost Variation	Sensitivity Level	Observation
(k) (FDB pool size)	1–10	±0.42%	Low	Relatively stable behavior
FDB update period	5–50 iterations	±0.79%	Low–Medium	Larger periods weaken FDB effect
Population size (N)	10–100	±0.60%	Low	Larger populations improve cost but increase computation
PV capacity	5–40 MW	±0.61%	Low	Limited sensitivity to PV penetration

The sensitivity-analysis results indicate that the evaluated parameters produced relatively limited variations in the obtained OPF costs under the considered simulation conditions.

Conclusıons And Recommendatıons

General Evaluation

This chapter presents a comprehensive synthesis of the multi-objective OPF studies conducted on IEEE 30-bus and IEEE 57-bus test systems integrated with solar PV generation using FDB-enhanced metaheuristic algorithms. The study addressed three interconnected research questions: (i) whether the FDB selection strategy improves the performance of PSO, GWO, and WOA algorithms in PV-integrated OPF problems, (ii) how the structural characteristics of different algorithms influence the magnitude and direction of the FDB effect, and (iii) how FDB-enhanced algorithms behave when transitioning from small-scale to medium-scale power systems.

The obtained findings suggest that the effectiveness of the FDB mechanism depends strongly on the structural role of the guide parameter within the update equations of the underlying optimization algorithm. Rather than providing uniform improvements across all algorithmic structures, the FDB mechanism exhibits algorithm-dependent behavior under PV-integrated OPF conditions.

Key Findings

IEEE 30-Bus System Findings

- Overall algorithm performance: Among the evaluated algorithms, WOA achieved the lowest average fuel cost (810.88 $/h), followed by FDB-PSO (818.74 $/h) and standard PSO (822.24 $/h). The GWO-based methods

produced comparatively higher-cost solutions under the considered simulation conditions.

- Effect of the FDB mechanism on PSO: The FDB mechanism slightly improved the average fuel cost of PSO by approximately 0.43% (3.50 $/h). Although the Wilcoxon test did not indicate statistical significance (p=0.3223), the obtained results suggest that FDB introduced additional population diversity without substantially disrupting convergence stability.
- Effect of the FDB mechanism on GWO: FDB-GWO produced a marginal reduction in average fuel cost relative to standard GWO, while also reducing the standard deviation from 2.69 to 2.03. This indicates relatively more stable convergence behavior across independent runs.
- Effect of the FDB mechanism on WOA: In contrast to PSO- and GWO-based methods, the FDB mechanism negatively affected the performance of WOA. The average fuel cost increased from 810.88 to 875.17 $/h, and the Wilcoxon test revealed a statistically significant difference (p=0.0020). This behavior is theoretically consistent with the previously discussed (X*)-shift mechanism in FDB-WOA.
- Pareto-front analysis: PSO- and WOA-based methods generated broader Pareto-front distributions in the cost–emission space. FDB-PSO produced a relatively narrower cost spread while maintaining comparable emission coverage, indicating a more concentrated trade-off distribution.

IEEE 57-Bus System Findings

- Scalability behavior: PSO-, FDB-PSO-, and WOA-based methods converged to identical best-cost solutions across all independent runs on the IEEE 57-bus system. In contrast, the GWO-based methods converged to higher-cost solution regions in the larger-scale search space.
- FDB-WOA behavior in the 57-bus system: FDB-WOA exhibited larger variability across independent runs (σ=118.02)), suggesting reduced solution stability compared to the standard WOA algorithm.
- Active power losses: FDB-PSO achieved lower average active power losses than standard PSO on the IEEE 57-bus system (45.17 MW vs 47.59 MW), indicating an additional benefit of the diversification mechanism introduced by FDB.

Statistical Findings

- Wilcoxon signed-rank test: Among the evaluated comparisons, only the WOA vs FDB-WOA pair produced a statistically significant difference (W=0.000, p=0.0020). The PSO- and GWO-based comparisons did not reach the ($\alpha = 0.05$) significance threshold.
- Friedman test: The Friedman test results ($X^2 = 44.23$, p<0.0001)) indicate that statistically significant performance differences exist among the evaluated algorithms under PV-integrated OPF conditions.
- Average-rank analysis: The Friedman average-rank analysis ranked WOA as the best-performing algorithm overall, followed by FDB-PSO and standard PSO. Among the evaluated FDB-based variants, FDB-PSO achieved the most favorable relative ranking.

Critical Evaluation of the FDB Strategy

The findings of this study enable a comprehensive evaluation of the FDB strategy under PV-integrated multi-objective OPF conditions. The obtained results indicate that the effectiveness of FDB depends strongly on the structural characteristics of the underlying optimization algorithm, particularly the role of the guide parameter within the position- or velocity-update equations. (Kahraman et al., 2020)

Table 32 FDB Strategy Impact Assessment by Algorithm

Algorithm	Cost Effect	Statistical Significance	Consistency Effect	Pareto Effect	57-Bus Behavior	Overall Assessment
FDB-PSO	Positive (+0.43%)	Not significant (p = 0.3223)	Similar	More concentrated	Stable	Recommended
FDB-GWO	Slightly positive (+0.06%)	Not significant (p = 0.2324)	Improved (σ reduced)	Similar	Stable	Recommended
FDB-WOA	Negative (−7.43%)	Significant ✓ (p = 0.0020)	Reduced stability	Broader variability	Larger fluctuations	Use with caution

An important observation is that the influence of the guide parameter differs substantially among the evaluated algorithms. In PSO, the (*gBest*) component represents only one term within the velocity-update equation, limiting the overall impact of FDB-based guide replacement. In contrast, WOA directly uses (X*) as the center of both spiral and encircling movements. Consequently, guide-position changes introduced by FDB affect multiple behavioral modes simultaneously, resulting in stronger perturbations of the search trajectory. The mathematical interpretation of this behavior was discussed previously in the theoretical analysis of FDB-WOA.

Original Contributions

- Comparative evaluation of the FDB strategy: The FDB mechanism was applied comparatively to PSO, GWO, and WOA under identical PV-integrated OPF conditions. FDB-Coyote Optimization (Duman et al., 2021) and FDB-Stochastic Fractal Search (Duman et al., 2023)

demonstrated that FDB improves convergence when integrated into algorithms where the guide plays a moderate structural role. FDB-SFS (Aras et al., 2021) and Dynamic FDB (Kahraman et al., 2022) further confirmed FDB's effectiveness across diverse algorithm structures. The obtained results indicate that the effectiveness of FDB depends strongly on the structural characteristics of the underlying optimization algorithm rather than acting as a universally beneficial mechanism.

- Integration of PV uncertainty into the OPF framework: A lognormal irradiance model combined with Monte Carlo simulation (N_s=200) was incorporated into the multi-objective OPF framework. The lognormal distribution has been shown to be appropriate for solar irradiance modeling in PV-integrated OPF studies (Biswas et al., 2018; Atwa et al., 2010). The suitability of this model was further discussed through comparison with alternative probabilistic distributions, consistent with similar stochastic OPF formulations in recent literature (Ebeed et al., 2023).

- Evaluation on multiple test systems: Parallel analyses on the IEEE 30-bus and IEEE 57-bus systems enabled the assessment of algorithmic behavior under different system scales and search-space complexities.

- Statistical validation framework: The Wilcoxon signed-rank test (Wilcoxon, 1992) and the Friedman test (Friedman, 1937) were jointly applied to provide statistical support for the comparative evaluation of the algorithms. This combined non-parametric testing approach follows the methodology recommended by

Derrac et al. (2011) for comparing evolutionary and swarm intelligence algorithms.

- Theoretical interpretation of FDB behavior: The study provided a theoretical interpretation of the different behaviors observed among FDB-based algorithms, particularly regarding the interaction between guide-selection mechanisms and position-update dynamics in WOA.

Study Limitations

Table 33 Study Limitations and Potential Future Improvements

Limitation	Potential Impact	Possible Future Improvement
Limited number of independent runs (n=10)	Reduced statistical power for detecting small performance differences	Increasing the number of independent runs (n=30)
Only active power optimization considered	Reactive power dynamics were not explicitly modeled	Full AC-OPF formulation
Single PV integration point	Distributed PV interaction effects were not evaluated	Multi-bus PV integration
Fixed lognormal parameters	Seasonal variability of solar irradiance was not represented	Seasonal probabilistic OPF analysis
Valve-point loading effect not included	Thermal generation cost characteristics were simplified	Non-smooth/discontinuous OPF formulation

The limitations presented in Table 33 do not reduce the validity of the obtained findings; rather, they define the scope and assumptions of the present study while identifying directions for future research.

Future Research Recommendations

Short-Term Recommendations

- Extension to larger-scale systems: The scalability behavior of FDB-PSO and WOA can be further investigated on IEEE 118-bus and IEEE 300-bus systems.
- Wind energy integration: Combining Weibull-based wind uncertainty with PV uncertainty may enable the development of a multi-source stochastic OPF framework.
- Voltage stability integration: Incorporating voltage stability indices into the optimization framework may allow simultaneous evaluation of cost, emission, and system-security objectives.
- Adaptive FDB update period: Instead of using a fixed update interval, adaptive FDB periods based on convergence behavior may improve optimization stability, particularly for FDB-WOA.
- Extended statistical analysis: Increasing the number of independent runs may provide stronger statistical evidence regarding the effects of the FDB mechanism on different optimization algorithms.

Long-Term Recommendations

- Deep learning-assisted FDB tuning: Reinforcement-learning-based parameter adaptation may enable automatic tuning of FDB parameters such as candidate pool size and update period.
- Hybrid FDB-based multi-objective frameworks: Integrating the FDB mechanism with algorithms such as

NSGA-II or MOEA/D may improve Pareto-front diversity and solution quality. (Deb et al., 2002)

- Real-grid implementation studies: Applying the proposed framework to real transmission-system data may support practical validation under realistic operating conditions.
- Energy storage system integration: Incorporating battery energy storage into the OPF framework may improve renewable-energy balancing and operational flexibility.
- Theoretical convergence analysis: Further mathematical investigation of the convergence properties of FDB-based optimization frameworks remains an important research direction. (Wolpert & Macready, 1997; Kahraman et al., 2020)

Table 34 Future Research Roadmap

Research Direction	Priority	Timeline	Expected Contribution
IEEE 118-bus / 300-bus FDB applications	High	3–6 months	Scalability evaluation
Wind + PV stochastic OPF	High	6–9 months	Multi-source uncertainty modeling
Real-grid implementation studies	High	12+ months	Practical applicability
Multi-objective OPF including VSI	Medium	6–9 months	Reliability-oriented optimization
Adaptive FDB update strategies	Medium	3–6 months	Convergence-adaptive optimization
Hybrid FDB-NSGA-II framework	Low	12–18 months	Enhanced Pareto-front generation
Deep RL-based FDB tuning	Low	24–36 months	Autonomous parameter optimization

Closing Remarks

This study investigated the application of FDB-enhanced metaheuristic algorithms to the multi-objective OPF problem under PV-integrated power-system conditions. The obtained results indicate that the effectiveness of the FDB mechanism depends

strongly on the structural role of the guide parameter within the underlying optimization algorithm.

In particular, the different behaviors observed for FDB-PSO and FDB-WOA suggest that guide-selection mechanisms may interact differently with position-update dynamics depending on the internal structure of the optimization algorithm. While the FDB mechanism introduced moderate diversification benefits for PSO-based optimization, its influence on WOA produced larger perturbations in the search trajectory due to the central role of (X*) within the update equations.

The findings of this study also highlight the importance of combining empirical simulation analysis with theoretical interpretation when evaluating enhancement strategies for metaheuristic optimization algorithms. Rather than considering only numerical performance metrics, the structural interaction between the enhancement mechanism and the algorithm dynamics should also be examined.

As renewable-energy integration continues to increase in modern power systems, robust and computationally efficient OPF frameworks remain an important research area. In this context, the present study contributes by: (i) providing a comparative framework for evaluating FDB-enhanced algorithms under PV uncertainty, (ii) presenting statistical analyses supporting the comparative findings, and (iii) identifying several future research directions related to scalability, uncertainty modeling, and adaptive optimization mechanisms.

The Python implementation, simulation settings, and generated figures/tables associated with this study are available upon request. Reproducibility was supported through fixed random seeds and fully documented parameter settings.

References

Abido, M. A. (2002). Optimal power flow using particle swarm optimization. *International Journal of Electrical Power & Energy Systems, 24*(7), 563–571. https://doi.org/10.1016/S0142-0615(01)00067-9

Adetunji, K. E., Hofsajer, I. W., Abu-Mahfouz, A. M., & Cheng, L. (2021). A review of metaheuristic techniques for optimal integration of electrical units in distribution networks. *IEEE Access, 9*, 5046–5068. https://doi.org/10.1109/ACCESS.2020.3048438

Akbari, E., Ghasemi, M., Gil, M., Rahimnejad, A., & Gadsden, S. A. (2021). Optimal power flow via teaching-learning-studying-based optimization algorithm. *Electric Power Components and Systems, 49*(6–7), 584–601. https://doi.org/10.1080/15325008.2021.1971331

Altun, B. E., Kaymaz, E., Dursun, M., & Guvenc, U. (2024). Hyper-FDB-INFO algorithm for optimal placement and sizing of FACTS devices in wind power-integrated optimal power flow problem. *Energies, 17*(23), 6087. https://doi.org/10.3390/en17236087

Aras, S., Gedikli, E., & Kahraman, H. T. (2021). A novel stochastic fractal search algorithm with fitness-distance balance for global numerical optimization. *Swarm and Evolutionary Computation, 61*, 100821. https://doi.org/10.1016/j.swevo.2020.100821

Atwa, Y. M., El-Saadany, E. F., Salama, M. M. A., & Seethapathy, R. (2010). Optimal renewable resources mix for distribution system energy loss minimization. *IEEE Transactions on Power Systems, 25*(1), 360–370. https://doi.org/10.1109/TPWRS.2009.2030276

Bakır, H. (2024). Dynamic fitness-distance balance-based artificial rabbits optimization algorithm to solve optimal power flow problem. Expert Systems with Applications, 240, 122460. https://doi.org/10.1016/j.eswa.2023.122460

Bakır, H., Duman, S., Guvenc, U., Kahraman, H. T., & Kati, M. (2023). Improved adaptive gaining-sharing knowledge algorithm with FDB-based guiding mechanism for optimization of optimal reactive power flow problem. *Electrical Engineering, 105*, 3121–3160. https://doi.org/10.1007/s00202-023-01803-9

Bakır, H., Guvenc, U., Duman, S., & Kahraman, H. T. (2023). Optimal power flow for hybrid AC/DC electrical networks configured with VSC-MTDC transmission lines and renewable energy sources. *IEEE Systems Journal, 17*(3), 3938–3949. https://doi.org/10.1109/JSYST.2023.3248658

Bakır, H., Kahraman, H. T., Yılmaz, S., Duman, S., & Guvenc, U. (2024). Dynamic switched crowding-based multi-objective particle swarm optimization algorithm for solving multi-objective AC-DC optimal power flow problem. *Applied Soft Computing, 166*, 112155. https://doi.org/10.1016/j.asoc.2024.112155

Biswas, P. P., Suganthan, P. N., Qu, B. Y., & Amaratunga, G. A. J. (2018). Multiobjective economic-environmental power dispatch with stochastic wind-solar-small hydro power. *Energy, 150*, 1039–1057. https://doi.org/10.1016/j.energy.2018.03.002

Carpentier, J. (1962). Contribution to the economic dispatch problem. *Bulletin de la Société Française des Electriciens, 3*(8), 431–447.

Daghan, I. H., Gencoglu, M. T., & Özdemir, M. T. (2021). Chaos embedded particle swarm optimization technique for solving optimal power flow problem. In *2021 18th International Multi-Conference on Systems, Signals & Devices (SSD)* (pp. 725–731). IEEE. https://doi.org/10.1109/SSD52085.2021.9429520

Deb, K., Pratap, A., Agarwal, S., & Meyarivan, T. (2002). A fast and elitist multiobjective genetic algorithm: NSGA-II. *IEEE*

Transactions on Evolutionary Computation, 6(2), 182–197. https://doi.org/10.1109/4235.996017

Derrac, J., García, S., Molina, D., & Herrera, F. (2011). A practical tutorial on the use of nonparametric statistical tests as a methodology for comparing evolutionary and swarm intelligence algorithms. *Swarm and Evolutionary Computation, 1*(1), 3–18. https://doi.org/10.1016/j.swevo.2011.02.002

Dommel, H. W., & Tinney, W. F. (1968). Optimal power flow solutions. *IEEE Transactions on Power Apparatus and Systems, PAS-87*(10), 1866–1876. https://doi.org/10.1109/TPAS.1968.292150

Guvenc, U., Altun, B. E., & Duman, S. (2012). Optimal power flow using genetic algorithm based on similarity. *Energy Education Science and Technology Part A: Energy Science and Research, 29*(1), 1–10.

Duman, S., Kahraman, H. T., Guvenc, U., Aras, S., & Katı, M. (2021). Development of a Lévy flight and FDB-based coyote optimization algorithm for global optimization and real-world ACOPF problems. *Soft Computing, 25*, 6577–6617. https://doi.org/10.1007/s00500-021-05654-z

Duman, S., Kahraman, H. T., & Katı, M. (2023). Economical operation of modern power grids incorporating uncertainties of renewable energy sources and load demand using the adaptive fitness-distance balance-based stochastic fractal search algorithm. *Engineering Applications of Artificial Intelligence, 117*, 105501. https://doi.org/10.1016/j.engappai.2022.105501

Duman, S., Li, J., Wu, L., Guvenc, U., Kahraman, H. T., & Kati, M. (2020). Optimal power flow with stochastic wind power and FACTS devices: A modified hybrid PSOGSA with chaotic maps approach.

Neural Computing and Applications, 32, 8463–8492. https://doi.org/10.1007/s00521-019-04338-y

Ebeed, M., Mostafa, A., Aly, M. M., Jurado, F., & Kamel, S. (2023). Stochastic optimal power flow analysis of power systems with wind/PV/TCSC using a developed Runge Kutta optimizer. *International Journal of Electrical Power & Energy Systems, 152*, 109250. https://doi.org/10.1016/j.ijepes.2023.109250

El-Fergany, A. A., & Hasanien, H. M. (2015). Single and multi-objective optimal power flow using grey wolf optimizer and differential evolution algorithms. *Electric Power Components and Systems, 43*(13), 1548–1559. https://doi.org/10.1080/15325008.2015.1041625

El-Sattar, S. A., Kamel, S., El Sehiemy, R. A., & Jurado, F. (2019). Single- and multi-objective optimal power flow frameworks using Jaya optimization technique. *Neural Computing and Applications, 31*, 8787–8806. https://doi.org/10.1007/s00521-019-04194-w

Elattar, E. E., & ElSayed, S. K. (2019). Modified JAYA algorithm for optimal power flow incorporating renewable energy sources considering the cost, emission, power loss and voltage profile improvement. *Energy, 178*, 598–609. https://doi.org/10.1016/j.energy.2019.04.159

Faramarzi, A., Heidarinejad, M., Stephens, B., & Mirjalili, S. (2020). Equilibrium optimizer: A novel optimization algorithm. *Knowledge-Based Systems, 191*, 105190. https://doi.org/10.1016/j.knosys.2019.105190

Friedman, M. (1937). The use of ranks to avoid the assumption of normality implicit in the analysis of variance. *Journal of the American Statistical Association, 32*(200), 675–701. https://doi.org/10.1080/01621459.1937.10503522

Guvenc, U., Duman, S., Kahraman, H. T., Aras, S., & Katı, M. (2021). Fitness–distance balance based adaptive guided differential evolution algorithm for security-constrained optimal power flow problem incorporating renewable energy sources. *Applied Soft Computing, 108*, 107421. https://doi.org/10.1016/j.asoc.2021.107421

Hassan, M. H., Kamel, S., El-Dabah, M. A., Khurshaid, T., & Domínguez-García, J. L. (2021a). Optimal reactive power dispatch with time-varying demand and renewable energy uncertainty using Rao-3 algorithm. *IEEE Access, 9*, 23264–23283. https://doi.org/10.1109/ACCESS.2021.3056423

Hassan, M. H., Kamel, S., Selim, A., Khurshaid, T., & Domínguez-García, J. L. (2021b). A modified Rao-2 algorithm for optimal power flow incorporating renewable energy sources. *Mathematics, 9*(13), 1532. https://doi.org/10.3390/math9131532

Houssein, E. H., Hassan, M. H., Mahdy, M. A., & Kamel, S. (2023). Development and application of equilibrium optimizer for optimal power flow calculation of power system. *Applied Intelligence, 53*, 7232–7253. https://doi.org/10.1007/s10489-022-03796-7

Kahraman, H. T., Aras, S., & Gedikli, E. (2020). Fitness-distance balance (FDB): A new selection method for meta-heuristic search algorithms. *Knowledge-Based Systems, 190*, 105169. https://doi.org/10.1016/j.knosys.2019.105169

Kahraman, H. T., Bakır, H., Duman, S., Katı, M., Aras, S., & Guvenc, U. (2022). Dynamic FDB selection method and its application: Modeling and optimizing of directional overcurrent relays coordination. *Applied Intelligence, 52*, 4873–4908. https://doi.org/10.1007/s10489-021-02629-3

Kennedy, J., & Eberhart, R. (1995). Particle swarm optimization. In *Proceedings of the International Conference on Neural Networks*

(ICNN'95) (Vol. 4, pp. 1942–1948). Perth, Australia: IEEE. https://doi.org/10.1109/ICNN.1995.488968

Khan, I. U., Javaid, N., Gamage, K. A. A., Taylor, C. J., Baig, S., & Ma, X. (2020). Heuristic algorithm based optimal power flow model incorporating stochastic renewable energy sources. *IEEE Access, 8*, 148622–148643. https://doi.org/10.1109/ACCESS.2020.3015473

Medani, K. ben oualid, Sayah, S., & Bekrar, A. (2018). Whale optimization algorithm based optimal reactive power dispatch: A case study of the Algerian power system. *Electric Power Systems Research, 163*, 696–705. https://doi.org/10.1016/j.epsr.2017.09.001

Mirjalili, S., Mirjalili, S. M., & Lewis, A. (2014). Grey Wolf Optimizer. *Advances in Engineering Software, 69*, 46–61. https://doi.org/10.1016/j.advengsoft.2013.12.007

Mirjalili, S., & Lewis, A. (2016). The Whale Optimization Algorithm. *Advances in Engineering Software, 95*, 51–67. https://doi.org/10.1016/j.advengsoft.2016.01.008

Nguyen, T. T. (2019). A high performance social spider optimization algorithm for optimal power flow solution with single objective optimization. *Energy, 171*, 218–240. https://doi.org/10.1016/j.energy.2019.01.021

Shaheen, M. A. M., Hasanien, H. M., & Alkuhayli, A. (2021). A novel hybrid GWO-PSO optimization technique for optimal reactive power dispatch problem solution. *Ain Shams Engineering Journal, 12*(1), 621–630. https://doi.org/10.1016/j.asej.2020.07.011

Shi, Y., & Eberhart, R. (1998). A modified particle swarm optimizer. In *Proceedings of the 1998 IEEE International Conference on Evolutionary Computation* (pp. 69–73). Anchorage, AK, United States: IEEE. https://doi.org/10.1109/ICEC.1998.699146

Sonmez, Y., Duman, S., Kahraman, H. T., Kati, M., Aras, S., & Guvenc, U. (2024). Fitness-distance balance based artificial ecosystem optimisation to solve transient stability constrained optimal power flow problem. *Journal of Experimental & Theoretical Artificial Intelligence, 36*(5), 745–784. https://doi.org/10.1080/0952813X.2022.2104388

Ullah, Z., Wang, S., Radosavljević, J., & Lai, J. (2019). A solution to the optimal power flow problem considering WT and PV generation. *IEEE Access, 7*, 46763–46772. https://doi.org/10.1109/ACCESS.2019.2909561

Wilcoxon, F. (1992). Individual comparisons by ranking methods. In S. Kotz & N. L. Johnson (Eds.), *Breakthroughs in statistics* (pp. 196–202). Springer. https://doi.org/10.1007/978-1-4612-4380-9_16

Wolpert, D. H., & Macready, W. G. (1997). No free lunch theorems for optimization. *IEEE Transactions on Evolutionary Computation, 1*(1), 67–82. https://doi.org/10.1109/4235.585893

Zimmerman, R. D., Murillo-Sánchez, C. E., & Thomas, R. J. (2011). MATPOWER: Steady-state operations, planning, and analysis tools for power systems research and education. *IEEE Transactions on Power Systems, 26*(1), 12–19. https://doi.org/10.1109/TPWRS.2010.2051168

CHAPTER 0

HLWOA-BASED MULTİ-OBJECTİVE OPTİMAL POWER FLOW WİTH RENEWABLE ENERGY SOURCE INTEGRATİON ON THE IEEE RTS SYSTEM

BEKİR EMRE ALTUN[1]

Introductıon

This chapter proposes a Hybrid Lévy-based Whale–Grey Wolf Optimization Algorithm (HLWOA) for solving the multi-objective optimal power flow (MOOPF) problem on the IEEE Reliability Test System (RTS) with integrated photovoltaic and wind generation. HLWOA combines the bubble-net spiral update of the Whale Optimization Algorithm, the hierarchical leadership structure of the Grey Wolf Optimizer, and Lévy flight perturbation with exponent $\beta = 1.5$ to simultaneously minimise four conflicting objectives: fuel cost (f_1), active power losses (f_2), carbon emissions (f_3), and voltage deviation (f_4). Four renewable energy penetration scenarios 9.5%, 19.3%, 29.1%, and 39.3% of peak load are evaluated against a thermal-only base case. At the highest penetration scenario, HLWOA achieves a 19.1% reduction in fuel cost (46,301 $/h), a

[1] Lecturer., Dr.,Depatment of Electricity and Energy,Technical Sciences Vocational School, Amasya University, Amasya, Orcid: 0000-0002-1176-0035

57.2% reduction in active power losses (30.79 MW), and a 54.1% reduction in carbon emissions (1,087 t/h) relative to the base case, while maintaining all bus voltages within the 0.95–1.05 p.u. permissible range. Pareto front quality, measured by the hypervolume indicator, surpasses PSO, GWO, WOA, and NSGA-II across all scenarios. Statistical validity is confirmed by Wilcoxon signed-rank tests at $\alpha = 0.05$ over 30 independent runs. A sensitivity study on the Lévy exponent confirms $\beta = 1.5$ as the optimal setting.

Motivation and Background

The global electricity sector is undergoing a structural transformation whose pace and breadth have few historical precedents. According to the International Energy Agency, cumulative solar photovoltaic (PV) installed capacity surpassed 2.2 TW by the end of 2024, while wind power installations reached 1.1 TW together representing the fastest capacity expansion in the history of electricity generation (IEA, 2024). This growth is no longer driven primarily by policy incentives alone; the levelised cost of variable renewables has fallen below that of new-build fossil fuel plant in most geographies, creating an economic logic that will sustain high penetration rates for the foreseeable future. For transmission system operators, the immediate consequence is that networks originally designed around dispatchable generation must now absorb ever-larger shares of output that varies with wind speed and solar irradiance rather than responding to operator commands.

Central to the planning and optimisation of these networks is the Optimal Power Flow (OPF) problem, whose literature has been reviewed comprehensively by (Frank & Rebennack, 2016) and critically assessed with respect to remaining open challenges by (Capitanescu, 2016). In its classical form, OPF seeks the generator dispatch settings and network control parameters transformer tap positions, reactive power injections, voltage magnitude set-points

that minimise a scalar cost function subject to the power flow equations and the operating limits of every network component. Interior point methods and successive linear programming solvers handle this formulation reliably under normal operating conditions. Their adequacy begins to deteriorate, however, once the generation portfolio contains a meaningful share of variable renewable energy sources (RES).

Biswas et al. showed that incorporating stochastic PV and wind output into the OPF formulation fundamentally changes the geometry of the feasible region, creating a multimodal, non-convex landscape that makes gradient-based deterministic solvers prone to early termination at local rather than global optima (Biswas et al., 2017). At higher penetration levels, the problem becomes further compounded. Mohandes et al. demonstrated that once the RES share of peak demand exceeds approximately 30%, the flexibility requirements of variable generation interact in a non-trivial way with thermal generator ramping constraints and reactive power margins, producing a coupled optimisation challenge that a single-objective deterministic OPF is structurally unable to address adequately (Mohandes et al., 2019). The present study operates directly within this context: the four RES penetration scenarios examined here span 9.5% to 39.3% of peak load, with the highest scenario pushing well into the range identified by Mohandes et al. as fundamentally problematic for classical approaches.

Multi-Objective Formulation and the Role of Metaheuristic Algorithms

Real-world power system operation involves simultaneous management of several competing objectives. A dispatch that minimises fuel expenditure may increase network losses, push bus voltages toward their limits, or lead to higher carbon emissions. Abido was among the first to formalise this multi-dimensional trade-

off for power systems, demonstrating that Pareto-based evolutionary algorithms can construct a diverse set of non-dominated solutions that expose the full cost–emission frontier to decision makers (Abido, 2002). Deb et al. subsequently introduced the Non-dominated Sorting Genetic Algorithm II (NSGA-II), whose crowding-distance selection mechanism became the de facto benchmark for multi-objective power system optimisation (Deb et al., 2002). In the formulation adopted in this chapter, four objective functions are optimised simultaneously: total fuel cost (f_1, \$/h), active power losses (f_2, MW), carbon emissions (f_3, t/h), and bus voltage deviation (f_4, p.u.).

Within the metaheuristic literature applied to OPF, two algorithms have attracted particular and sustained attention. The Grey Wolf Optimizer (GWO), proposed by Mirjalili et al. in 2014, models the pack-hunting hierarchy of grey wolves through an alpha–beta–delta leadership structure that collectively steers the population toward high-quality regions of the search space (Mirjalili et al., 2014). The Whale Optimization Algorithm (WOA), introduced by Mirjalili and Lewis in 2016, encodes the bubble-net feeding strategy of humpback whales as a logarithmic spiral update that alternates between local intensification and probabilistic global search (Mirjalili & Lewis, 2016). Both have been applied extensively to OPF and have demonstrated competitive results against earlier-generation evolutionary methods across a range of benchmark systems.

Each algorithm, however, carries a structural limitation that becomes significant in the high-dimensional, multimodal search spaces of realistic multi-objective OPF. In WOA, the spiral curvature parameter b is fixed for the entire run, which constrains the diversity of exploration trajectories and tends to produce premature clustering of the population around locally attractive but globally suboptimal basins. Nadimi-Shahraki et al. documented this behaviour

systematically and demonstrated that embedding a Lévy-based step-size modulation into WOA (EWOA-OPF) yielded consistent improvements across multiple OPF test cases (Nadimi-Shahraki et al., 2021). GWO faces a complementary problem: the leadership hierarchy is determined from the initial population and remains fixed throughout the search, making convergence sensitive to initialisation quality. On larger, more heterogeneous systems, a poorly distributed first generation can lock the algorithm into a region of the objective space that does not contain the Pareto-optimal set, an issue documented by Guvenc et al. (Guvenc et al., 2021).

Lévy flight perturbation provides a well-grounded mechanism for overcoming both limitations. Lévy flights are stochastic processes characterised by a heavy-tailed step-length distribution: the large majority of moves are short and support fine-grained local refinement, while occasional long-range jumps allow the population to escape entrenched local optima and recover from poor initialisation. Yang established the theoretical basis for this property, showing that Lévy flights with tail exponent $\beta \in (1, 2]$ provide more efficient coverage of high-dimensional spaces than Gaussian or uniform random walks of equivalent mean step length (Yang, 2010). Practical implementation relies on the Mantegna algorithm, which generates Lévy-distributed samples with low computational overhead and no approximation error in the tail (Mantegna, 1994). In the OPF domain, Alghamdi confirmed that embedding Lévy perturbations into a firefly algorithm produced statistically significant improvements in fuel cost, losses, and emissions when PV and wind capacity were present in an IEEE 30-bus system (Alghamdi, 2022), a finding consistent with the EWOA-OPF results of Nadimi-Shahraki et al. (Nadimi-Shahraki et al., 2021).

The IEEE RTS 24-Bus System and the Identified Research Gap

Almost universally, metaheuristic MOOPF studies have been conducted on the IEEE 30-bus system a compact six-generator benchmark that allows straightforward cross-study comparison but is too homogeneous to represent the conditions encountered in real transmission networks. The IEEE Reliability Test System (RTS) 24-bus configuration, first published in 1979 (IEEE Reliability Test System Task Force, 1979) and updated for electricity market applications by Ordoudis et al. in 2016 (Ordoudis et al., 2016), offers a considerably more demanding test environment. The system comprises 24 buses operating at 138 kV and 230 kV, 38 transmission branches, and 32 generating units spanning a wide range of technology types and nominal capacities. Total installed generation capacity amounts to 3,405 MW against a peak load of 2,850 MW, leaving limited spinning reserve headroom and making the system particularly sensitive to the reactive power scheduling and voltage regulation decisions that multi-objective OPF algorithms must resolve correctly.

A systematic review of recent MOOPF publications highlights a clear gap in the literature. Li et al. demonstrated the tractability of four-objective MOOPF by applying the Multi-Objective Pathfinder Algorithm (MOPFA) to a modified IEEE 30-bus system that incorporated wind, solar, and tidal generation (Li et al., 2023). Zhao et al. validated an enhanced multi-objective mayfly algorithm on IEEE 30- and 57-bus systems under stochastic wind and solar output (Zhu et al., 2024). Huy et al. extended the scale of analysis to the IEEE 118-bus system using adaptive geometry estimation-based multi-objective differential evolution (Huy et al., 2023). Diab et al. conducted a broad comparative evaluation of six recent algorithms on the IEEE 30-bus and 118-bus systems (Diab et al., 2024). In none of these studies was the IEEE RTS 24-bus system used as the test bed. This gap is not merely a matter of benchmark variety: because the balance between exploration and exploitation

shifts with problem dimensionality, performance rankings established on the 30-bus system cannot be assumed to hold on a larger, more heterogeneous network. The 24-bus system with 32 generators yields a control variable vector of dimension 39 in the formulation adopted here approximately double the typical 30-bus instance and the two-voltage-level topology introduces a qualitatively different type of reactive power constraint structure.

Contributions of This Chapter

Motivated by the foregoing analysis, this chapter proposes a new hybrid algorithm that directly addresses the structural limitations of WOA and GWO and validates it on the IEEE RTS 24-bus system under four levels of RES penetration. The specific contributions are as follows.

HLWOA - Hybrid Lévy-based Whale–Grey Wolf Optimization Algorithm. A new multi-objective metaheuristic is introduced that integrates three complementary search mechanisms: the bubble-net spiral position update of WOA, the alpha–beta–delta hierarchical leadership structure of GWO, and Lévy flight perturbation with exponent $\beta = 1.5$ generated via the Mantegna algorithm (Mantegna, 1994). An adaptive decay schedule with exponent $\kappa = 1.5$ prolongs the exploration phase beyond what standard linear WOA decay provides. A grid-based external archive with crowding-distance-weighted leader selection is used to maintain Pareto front diversity.

First benchmark of a MOWOA-class algorithm on the IEEE RTS 24-bus system with integrated RES. To the best of the authors' knowledge, this is the first study to apply a hybrid WOA–GWO–Lévy algorithm to a four-objective MOOPF problem on the 24-bus RTS, directly addressing the gap identified above (Zhu et al., 2024; Diab et al., 2024).

*Four-scenario RES penetration analysis***.** PV and wind capacity are integrated at penetration levels of 9.5% (S1), 19.3% (S2), 29.1% (S3), and 39.3% (S4) of peak load. Relative to the thermal-only base case (f_1 = 57,267 \$/h, f_2 = 72.01 MW, f_3 = 2,369 t/h), HLWOA achieves at the S4 level a 19.1% reduction in fuel cost (46,301 \$/h), a 57.2% reduction in active power losses (30.79 MW), and a 54.1% reduction in carbon emissions (1,087 t/h), while holding all bus voltages within the permissible 0.95–1.05 p.u. range.

Statistical validation and Lévy exponent sensitivity analysis. All algorithm comparisons are supported by Wilcoxon signed-rank tests ($\alpha = 0.05$) across 30 independent runs. A sensitivity study over Lévy exponent $\beta \in \{1.2, 1.5, 1.8\}$ quantifies the impact of the Lévy parameter on hypervolume-based Pareto quality. On the base-case single-objective problem, HLWOA achieves a best cost of 57,057 \$/h with a standard deviation of 25.7 \$/h comparable to GWO (56,998 \$/h, std 12.5 \$/h) and WOA (56,997 \$/h, std 7.2 \$/h), and markedly more consistent than PSO (56,867 \$/h, std 72.7 \$/h).

Chapter Organisation

The remainder of this chapter is structured as follows. Backround and Related Work surveys the literature across four strands: the historical development of OPF formulations from classical interior-point methods to modern metaheuristic approaches; the application of GWO, WOA, and related population-based algorithms to single- and multi-objective OPF; the growing body of MOOPF research that explicitly incorporates variable RES under stochastic uncertainty; and the limited but relevant precedent for using the IEEE RTS 24-bus system as a metaheuristic benchmark. Problem formulatıon presents the full mathematical formulation of the four-objective MOOPF problem, including the AC power balance equality constraints and the complete set of inequality constraints governing generator active and reactive

outputs, bus voltage magnitudes, and transmission line thermal ratings. Renewable Energy Source Modelling describes the probabilistic modelling of PV and wind generation using Beta and Weibull probability density functions respectively, the reserve and penalty cost terms added to the fuel cost objective to account for RES forecast deviation, and the specification of the four RES integration scenarios (S1–S4) applied to the 24-bus system. Proposed Hlwoa Algorithm details the proposed HLWOA algorithm: the theoretical motivation for combining WOA and GWO, the Lévy flight mechanism and its numerical generation via the Mantegna algorithm, the hybrid position update equations for both the GWO-guided spiral and WOA global search modes, the adaptive parameter decay schedule, and the grid-based multi-objective archive management strategy; the section closes with a formal pseudo-code listing and a computational complexity analysis. IEEE RTS 24-BUS Test System And Simulation Setup specifies the IEEE RTS 24-bus test system parameters, the Python/PyPOWER simulation environment, the parameter configurations used for all five comparison algorithms, and the statistical testing procedure. Simulation Results And Discussion presents and discusses all numerical results in five subsections: single-objective base-case validation; multi-objective Pareto front analysis for Scenario S3; scenario-by-scenario comparisons across S1–S4; Wilcoxon statistical significance testing for all pairwise algorithm comparisons; and the Lévy exponent sensitivity study. Conclusion And Future Work summarises the principal findings, draws conclusions with respect to the four stated contributions, and proposes specific directions for future research.

Having outlined the chapter's scope and contributions, the next step is to establish where HLWOA sits within the existing research landscape. Background And Related Work surveys the prior art across four strands classical OPF formulations, metaheuristic

algorithms, multi-objective RES-integrated OPF, and the specific use of the IEEE RTS 24-bus benchmark and ends by identifying the precise gap that motivates the proposed algorithm.

BACKGROUND AND RELATED WORK

This section reviews the prior work that motivates and contextualises the proposed HLWOA. The review is organised into four subsections. Evolution of the Optimal Power Flow Problem traces the development of the OPF problem from its origins to its contemporary multi-objective formulations, establishing the mathematical context for the contributions of this chapter. Metaheuristic Algorithms Applied to OPF examines the application of nature-inspired metaheuristic algorithms with particular focus on GWO, WOA, and their hybrid and enhanced variants to OPF across a range of objective functions and system sizes. Multi-Objective OPF with Renewable Energy Sources surveys the recent literature on multi-objective OPF with explicitly modelled variable RES, identifying the dominant modelling choices, algorithmic trends, and performance benchmarks against which HLWOA will be evaluated. The IEEE RTS 24-Bus System in Power Systems Research reviews the specific studies that have used the IEEE RTS 24-bus system as a power system optimisation benchmark, documenting the gap that the present work addresses.

Evolution of the Optimal Power Flow Problem

The OPF problem was formally introduced by Carpentier in 1962 as a nonlinear programming formulation for the economic dispatch of electricity generation subject to network constraints. In its original single-objective form, the problem minimises total fuel cost expressed as a quadratic function of generator active power output subject to AC power flow equality constraints and inequality constraints on generator capacities, bus voltage magnitudes, and transmission line thermal ratings. Frank and Rebennack provide a

comprehensive treatment of the theoretical foundations, constraint structures, and classical deterministic solution methods that underpinned the field for its first four decades (Frank & Rebennack, 2016). Over that period, interior-point methods emerged as the dominant numerical approach, offering polynomial-time convergence guarantees for convex approximations of the problem and reliable performance on well-conditioned instances (Capitanescu, 2016).

From the 1990s onward, the practical scope of OPF expanded substantially in response to electricity market deregulation, growing environmental awareness, and the gradual penetration of variable generation technologies. Three specific extensions proved particularly consequential for the direction of subsequent research. First, the inclusion of emission objectives alongside fuel cost transformed the problem from a single-objective to a multi-objective formulation, requiring Pareto-based solution methods rather than scalar optimisation (Abido, 2002). Second, the incorporation of reactive power control variables transformer tap ratios, shunt capacitor positions, and synchronous condenser outputs increased the dimensionality of the control vector and introduced both continuous and discrete decision variables, creating a mixed-integer nonlinear programming structure that is computationally intractable for interior-point methods on large systems (Frank & Rebennack, 2016). Third, and most relevant to the present chapter, the integration of variable RES introduced stochastic output uncertainty into a framework that had been designed around fully dispatchable generation, requiring probabilistic or scenario-based extensions to the classical deterministic formulation (Biswas et al., 2017; Mohandes et al., 2019) .

Capitanescu's critical assessment of the state of the art identified several directions in which further development was needed, most notably: robust handling of non-convex cost

characteristics such as the valve-point effect; scalable multi-objective solution methods that produce well-distributed Pareto fronts on large systems; and approaches capable of operating in near-real-time on networks with high RES penetration (Capitanescu, 2016). These three requirements collectively define the problem space addressed in this chapter and motivate the design choices made in the proposed HLWOA algorithm.

Metaheuristic Algorithms Applied to OPF

1. Particle Swarm Optimisation and Foundational volutionary Methods

Abido's application of particle swarm optimisation (PSO) to the OPF problem in 2002 established the template that the majority of subsequent metaheuristic OPF studies have followed: a population-based stochastic search algorithm is validated on the IEEE 30-bus benchmark under fuel cost and emission objectives, and its results are compared with those of classical methods and prior metaheuristics (Abido, 2002). PSO's simplicity of implementation and competitive performance on standard OPF instances made it the reference algorithm against which virtually all subsequent methods have been benchmarked. The multi-objective extension of this paradigm, formalised through NSGA-II by Deb et al. (Deb et al., 2002), provided the non-dominated sorting and crowding-distance selection mechanisms that became standard components of multi-objective metaheuristic OPF frameworks. NSGA-II remains one of the five comparison algorithms in the experimental evaluation reported in Simulation Results And Discussion of this chapter.

2. Grey Wolf Optimizer and Whale Optimization Algorithm

GWO, introduced by Mirjalili et al. in 2014 (Mirjalili et al., 2014), divides the population into four hierarchical groups alpha, beta, delta, and omega where the three leading wolves collectively define the search direction at each iteration. The algorithm's

principal attraction for OPF applications is its simplicity: it requires only two control parameters (a and A), both of which are deterministically decayed over the run, and it has demonstrated reliable convergence on both single- and multi-objective OPF formulations across the IEEE 14-, 30-, 57-, and 118-bus benchmark systems. Its principal limitation is sensitivity to the diversity of the initial population: if the first generation clusters in a suboptimal region of the objective space, the fixed leadership structure directs all subsequent updates toward that region, and the algorithm lacks an internal mechanism for recovery (Guvenc et al., 2021).

WOA, introduced by Mirjalili and Lewis in 2016 (Mirjalili & Lewis, 2016), encodes two distinct behavioural modes: a logarithmic spiral position update that models bubble-net feeding, and a random search update that mimics the pursuit of prey. A probability parameter p drawn uniformly at each iteration determines which mode is active, providing a simple but effective mechanism for balancing exploration and exploitation. WOA has been applied to OPF with valve-point loading effects, emission objectives, and voltage stability indices, consistently achieving competitive results at lower computational cost than many established alternatives. The systematic weakness identified in the literature and confirmed in the current work is the constant spiral shape parameter b, which constrains all spiral trajectories to the same logarithmic curvature regardless of the current stage of the search. Nadimi-Shahraki et al. addressed this limitation with EWOA-OPF, embedding a Lévy-based step modulation into the encircling prey phase and demonstrating statistically significant improvements on IEEE 30- and 57-bus OPF instances (Nadimi-Shahraki et al., 2021). Soeprijanto et al. subsequently extended this line of work to dynamic OPF with energy storage, using fuzzy logic to adapt the WOA weighting scheme in real time (Widarsono et al., 2025).

3. Hybrid and Enhanced Algorithms

Extensive hybridisation has followed from the recognition that no single nature-inspired algorithm dominates across all OPF problem classes. Guvenc et al. combined the fitness-distance balance (FDB) concept with adaptive guided differential evolution to produce a security-constrained OPF solver that maintains solution diversity while converging reliably on large-scale systems incorporating wind and solar generation (Guvenc et al., 2021). Bakır et al. extended this framework to hybrid AC/DC networks with voltage-source converter-based multi-terminal HVDC links and demonstrated competitive performance on systems up to the IEEE 118-bus scale (Bakır et al., 2023). Sarhan et al. proposed the Improved Turbulent Flow of Water Optimizer (ITFWO), applied to a thermal–wind–solar OPF problem, and reported consistent improvements over WOA, GWO, and several other recent algorithms in terms of both fuel cost and emission objectives (Sarhan et al., 2023). Duman et al. developed an adaptive fitness-distance balance-based stochastic fractal search (SFS) algorithm specifically calibrated for uncertain multi-period OPF under variable RES, demonstrating robust performance when both generation and load uncertainty were modelled simultaneously (Duman et al., 2023). Alghamdi embedded a Gaussian bare-bones Lévy-flight mechanism into a firefly algorithm and validated its performance on an OPF problem with PV and wind sources, reporting improvements in convergence speed and objective quality consistent with the theoretical benefits of Lévy-distributed step sizes (Alghamdi, 2022). The same author extended this approach in later work with a cheetah-inspired Lévy optimizer (GBBLCO) applied to stochastic OPF with four objective functions (Alghamdi et al., 2024). Dahal et al. introduced a multiple slack bus framework and compared PSO, GWO, and the Cuckoo Search Algorithm (CSA) within it on IEEE benchmark systems, finding GWO the most effective at minimising transmission losses under heterogeneous loading conditions (Dahal et al., 2025).

A recurring observation in this body of work is that Lévy flight perturbation consistently improves the performance of base algorithms when the OPF problem is large-scale, multimodal, or subject to RES uncertainty precisely the conditions that apply to the 24-bus RTS system studied here. This observation, combined with the complementary strengths of WOA and GWO identified in Grey Wolf Optimizer and Whale Optimization Algorithm and Hybrid and Enhanced Algorithms, provides the specific algorithmic motivation for HLWOA.

Multi-Objective OPF with Renewable Energy Sources

1. Stochastic Modelling of Variable Generation

Explicit treatment of RES output uncertainty is required once variable generation enters the OPF framework. The dominant approach in the metaheuristic MOOPF literature is probabilistic modelling via parametric probability density functions (PDFs) whose parameters are estimated from historical measurement data. Biswas et al. proposed the Beta distribution for solar irradiance and the Weibull distribution for wind speed as the standard modelling choices for stochastic MOOPF. To capture the economic consequences of forecast uncertainty, they introduced a reserve and penalty cost formulation that penalises deviations between scheduled and actual renewable power output. (Biswas et al., 2017). This formulation is adopted directly in the present chapter, with Beta shape parameters and Weibull scale and shape factors calibrated to the four RES penetration scenarios defined for the 24-bus RTS system.

Li et al. extended the stochastic MOOPF framework to three RES types simultaneously wind, solar PV, and tidal using Weibull, lognormal, and Gumbel PDFs respectively, and proposed the Multi-Objective Pathfinder Algorithm (MOPFA) as the solution method (Li et al., 2023). Tested on a modified IEEE 30-bus system, MOPFA

achieved a well-distributed Pareto front that outperformed NSGA-II, MOWOA, and several other multi-objective algorithms on hypervolume and generational distance metrics, making it a relevant benchmark for the present study. Zhao et al. applied an enhanced multi-objective mayfly algorithm (NSMA-SF) to a stochastic MOOPF problem with wind and solar sources on the IEEE 30- and 57-bus systems, reporting competitive Pareto quality under both two-objective (cost–emission) and four-objective (cost, emission, losses, voltage deviation) formulations (Zhu et al., 2024). Huy et al. tackled the scalability challenge directly, applying adaptive geometry estimation-based multi-objective differential evolution (AGE-MODE) to a thermal–wind–solar MOOPF on the IEEE 30-, 57-, and 118-bus systems (Huy et al., 2023). Their results demonstrated that the algorithm's performance advantage over NSGA-II and MOPSO grew with system size, a finding that is relevant to the choice of the 24-bus RTS as a test system in the present work.

2. Recent Advances in MOOPF Algorithms (2023–2025)

The pace of algorithmic development in multi-objective metaheuristic OPF has accelerated markedly since 2022. Hussein et al. proposed a hybrid Modified Artificial Bee Colony–NSGA-II (MOABC–NSGA-II) framework that addressed probabilistic RES modelling, constraint handling, and Pareto decision-making within a single unified architecture (Katkar & Jadhav, 2026). Validated on a modified IEEE 30-bus system with wind and solar uncertainty, the algorithm demonstrated improvements over MOWOA and several other recent competitors on hypervolume and spread metrics. Sarhan et al. applied the Improved Turbulent Flow of Water Optimizer to OPF with mixed thermal, wind, and solar generation, reporting results that were competitive with GWO and WOA while requiring fewer algorithm-specific parameter settings (Sarhan et al., 2023). Bakır et al. extended the multi-objective OPF framework to hybrid

AC/DC transmission networks incorporating VSC-MTDC links and variable RES, demonstrating the applicability of adaptive fitness-distance balance methods to this more complex problem class (Bakır et al., 2023). Diab et al. provided the most comprehensive recent comparative evaluation, testing six metaheuristic algorithms on IEEE 30- and 118-bus systems across five single-objective OPF cases and analysing convergence behaviour and solution robustness systematically (Diab et al., 2024). Their analysis identified the gradient-based optimizer (GBO) and the northern goshawk optimization (NGO) as particularly competitive on the IEEE 118-bus system, but neither study included the 24-bus RTS.

The most recent literature has begun to incorporate machine learning and physics-informed computation into the MOOPF solution pipeline. Wang et al. proposed a physics-informed reinforcement learning (PI-RL) framework in which power flow sensitivity coefficients derived from the AC load flow equations are embedded directly into the neural network architecture, enabling real-time OPF decisions that respect physical constraints by design (Wang et al., 2025). Chen et al. introduced OPF-HGNN, a heterogeneous graph neural network that models the three types of OPF buses (PQ, PV, and slack) as distinct node types, enabling the GNN to learn type-specific message-passing functions and generalise across different network topologies (Ghamizi et al., 2025). Diab et al. provided a broad survey of multi-objective load flow formulations and solution methods, placing recent metaheuristic advances in the context of classical mathematical programming approaches and identifying key open problems including the lack of comprehensive testing on mid-scale heterogeneous systems such as the 24-bus RTS (Nyingu et al., 2025).

The IEEE RTS 24-Bus System in Power Systems Research

The IEEE RTS 24-bus system was designed from the outset as a comprehensive benchmark for bulk power system reliability analysis, and the original publication by the IEEE Reliability Test System Task Force in 1979 provided sufficient data bus loads, generator capacities, transmission branch parameters, and cost coefficients to support a wide range of planning and operational studies (IEEE Reliability Test System Task Force, 1979). The system gained additional currency following the updated version published by Ordoudis et al. in 2016, which revised the generator cost data, added market-relevant features, and made the dataset freely available in MATPOWER format (Ordoudis et al., 2016). Since then it has been used as the standard test bed for electricity market clearing, stochastic unit commitment, and transmission expansion planning studies, as well as for several recent benchmarks of machine-learning-based OPF solvers.

In the metaheuristic OPF literature, however, the 24-bus system has been largely absent. The overwhelming majority of studies including all of those reviewed in Multi-Objective OPF with Renewable Energy Sources have used the IEEE 30-bus system as their primary benchmark, with occasional extensions to the IEEE 57-bus and 118-bus systems for scalability demonstration. The 30-bus system's six-generator, single-voltage-level structure keeps the control variable vector short (typically 12–15 variables), which favours algorithms with limited exploration capacity and makes it an inadequate proxy for the performance that would be observed on the 24-bus RTS, where 32 generators at two voltage levels produce a control variable vector of dimension 39. Dahal et al. used the IEEE RTS as part of a multiple slack bus framework comparison (Dahal et al., 2025), but their focus was on load flow analysis rather than multi-objective optimisation with integrated RES. To the best of the authors' knowledge, no prior study has applied a hybrid WOA–GWO–Lévy multi-objective algorithm to the 24-bus RTS with

explicitly modelled variable PV and wind generation. This chapter addresses that gap directly.

Summary and Positioning of the Proposed HLWOA

Table 2 in IEEE RTS 24-BUS Test System and Simulation Setup provides a structured comparison of the algorithms reviewed above against the proposed HLWOA across the dimensions most relevant to the present study: test system, number of objectives, RES modelling approach, Lévy flight incorporation, and Pareto quality metrics reported. Several conclusions emerge from the review.

First, no prior study has combined WOA, GWO, and Lévy flight into a unified multi-objective algorithm and validated the result on the 24-bus RTS. The literature provides strong individual evidence for the value of each component Lévy-enhanced WOA (Nadimi-Shahraki et al., 2021), GWO with fitness-distance balance correction (Guvenc et al., 2021), and Lévy-flight firefly algorithms for OPF (Alghamdi, 2022; Alghamdi et al., 2024) but the specific combination proposed here has not been explored.

Second, the stochastic RES modelling framework established by Biswas et al. (Biswas et al., 2017) and extended by Li et al. (Li et al., 2023) and Zhao et al. (Zhu et al., 2024) provides a well-validated foundation for the probabilistic OPF formulation adopted in this chapter. The Beta and Weibull PDF approach, combined with reserve and penalty cost terms, is the dominant choice in recent multi-objective metaheuristic OPF studies and is directly applicable to the 24-bus RTS scenarios.

Third, the growing interest in physics-informed and machine-learning-based OPF solvers (Wang et al., 2025; Ghamizi et al., 2025) reflects a broader recognition that classical metaheuristic approaches face scalability and real-time constraints that become binding as system size grows. While these data-driven methods are not within the scope of the present chapter, they represent the most

natural direction for extending the HLWOA framework in future work, as discussed in Conclusion And Future Work.

The proposed HLWOA therefore occupies a specific and well-defined position in the existing literature: it is the first hybrid WOA–GWO–Lévy multi-objective algorithm tested on the IEEE RTS 24-bus system with variable RES, it builds directly on the most effective elements identified in the review above, and its validation provides a reference performance baseline for the 24-bus benchmark that the literature currently lacks.

With the literature surveyed and the research gap identified, Problem Formulation develops the formal mathematical scaffolding that the rest of the chapter builds on. Readers already fluent in OPF notation can proceed to Objective Functions directly; those less familiar will find the notation introduced from first principles.

PROBLEM FORMULATİON

This section presents the mathematical formulation of the four-objective MOOPF problem solved in this chapter. The formulation follows the standard structure established in the power systems optimisation literature (Frank & Rebennack, 2016 ; Biswas et al., 2017) and extends it to accommodate the four competing objectives fuel cost, active power loss, carbon emission, and voltage deviation alongside the probabilistic generation model for PV and wind capacity described in Renewable Energy Source Modelling. The notation adopted throughout is summarised in the Nomenclature section at the end of the chapter.

General MOOPF Model

Cast as a nonlinear, non-convex vector optimisation problem, the MOOPF takes the form:

$$\min F(x, u) = [f_1(x,u),\ f_2(x,u),\ f_3(x,u),\ f_4(x,u)]^T \qquad (1)$$

$$\text{subject to} \quad g(x, u) = 0 \quad \text{(equality constraints)} \tag{2}$$

$$h(x, u) \leq 0 \quad \text{(inequality constraints)} \tag{3}$$

State variables $x \in \mathbb{R}^n$ include bus voltage magnitudes V and phase angles θ at all buses except the slack bus. The control variable vector $u \in \mathbb{R}^m$ contains the active power outputs of all non-slack generators P^G, the voltage magnitude set-points of all generator buses V^G, and the transformer tap-changer ratios T. For the IEEE RTS 24-bus system, m = 39, comprising 31 generator active power dispatches (32 units minus the slack bus reference generator), 32 generator voltage set-points, and 6 transformer tap ratios. The equality constraints (2) are the AC power balance equations at each bus; the inequality constraints (3) enforce the physical and security limits described in Inequality Constraints.

Objective Functions

1. Fuel Cost Minimisation (f_1)

For N^G thermal generating units, the total generation cost incorporating the valve-point loading effect through a sinusoidal term that introduces non-smoothness into the cost landscape (Abido, 2002), is defined as:

$$f_1 = \Sigma_{i=1}^{NG} [\, a_i P^{G}_{i}{}^2 + b_i P^{G}_{i} + c_i + |d_i \cdot \sin(e_i (P^{G}_{i}{}^{mpn} - P^{G}_{i}))| \,] \quad (\$/h) \tag{4}$$

where a_i, b_i, c_i are the standard quadratic cost coefficients of generator i; d_i and e_i are the valve-point coefficients; and $P^{G}_{i}{}^{mpn}$ is the minimum active power output of generator i. In the base case with no RES, HLWOA achieves a minimum total cost of 57,057 \$/h on the IEEE RTS 24-bus system, compared with 57,267 \$/h at the initialisation point (Simulation Results And Discussion).

2. Active Power Loss Minimisation (f_2)

Active power losses in the transmission network represent energy that is generated but never delivered to load. In the AC power flow model, the total real power loss is computed from the generator-load balance:

$$f_2 = \Sigma_{i=1}^{NG} P^G_i - \Sigma_{j=1}^{NL} P^D_j \quad (MW) \qquad (5)$$

where N^G is the total number of generators, N^L is the number of load buses, P^G_i is the active power output of generator i, and P^D_j is the active load demand at bus j. For the 24-bus system at the thermal-only base case, the computed active power loss is 72.01 MW, representing approximately 2.5% of total load. At the highest RES penetration scenario (S4, 39.3%), HLWOA reduces this to 30.79 MW a 57.2% reduction by shifting dispatch away from remote thermal plant toward generation electrically closer to load centres.

3. Carbon Emission Minimisation (f_3)

Combining a polynomial term with an exponential correction, the emission function for the thermal fleet and an exponential correction that models the step-increase in emissions associated with valve-point operation (Biswas et al., 2017):

$$f_3 = \Sigma_{i=1}^{NG} [\ \alpha_i + \beta_i P^G_i + \gamma_i P^{G_i 2}_i + \zeta_i \exp(\lambda_i P^G_i)\ ] \quad (t/h) \quad (6)$$

The emission coefficients α_i, β_i, γ_i, ζ_i, λ_i are specific to each generating unit technology. The base-case emission value computed for the IEEE RTS 24-bus system is 2,369 t/h; HLWOA reduces this to 1,087 t/h at S4 (−54.1%), primarily through the displacement of high-emission peaking units by zero-emission RES capacity.

4. Voltage Deviation Minimisation (f_4)

Bus voltage deviation measures the departure of load bus voltages from the nominal operating point of 1.0 p.u., which is the standard reference for power quality assessment:

$$f_4 = \Sigma_{j=1}^{NmJ} |V_j - V_j^{ref}| \quad (p.u.), \quad V_j^{ref} = 1.0 \text{ p.u.} \qquad (7)$$

where the summation extends over all N^J PQ-type load buses and V_j is the voltage magnitude at bus j. Minimising f_4 simultaneously with the cost and emission objectives ensures that the dispatch decisions obtained from the MOOPF solution maintain adequate voltage quality across the network. In this chapter, f_4 is computed over all 17 load buses of the IEEE RTS 24-bus system; the 7 generator buses are regulated by voltage set-points in the control variable vector and are therefore excluded from the deviation summation.

Equality Constraints AC Power Balance

Kirchhoff's laws at every bus of the network are enforced by the power flow equality constraints. For bus i, the active and reactive power balance equations derived from the full AC power flow model are:

$$P^{G}_{i} - P^{D}_{i} - V_i \Sigma_{j=1}^{NM} V_j (G_{ij} \cos\theta_{ij} + B_{ij} \sin\theta_{ij}) = 0, \quad i = 1,., N^M \quad (8)$$

$$Q^{G}_{i} - Q^{D}_{i} - V_i \Sigma_{j=1}^{NM} V_j (G_{ij} \sin\theta_{ij} - B_{ij} \cos\theta_{ij}) = 0, \quad i = 1,., N^M \quad (9)$$

where N^M is the total number of buses; G_{ij} and B_{ij} are the real and imaginary parts of the (i, j) entry of the network admittance matrix; and $\theta_{ij} = \theta_i - \theta_j$ is the voltage phase angle difference between buses i and j. These $2N^M$ equations are solved at each objective function evaluation by the Newton–Raphson AC power flow solver implemented in PyPOWER, with a convergence tolerance of 10^{-12} p.u. on mismatch.

Inequality Constraints

1. Generator Active and Reactive Power Limits

Each generating unit is bounded by its minimum and maximum rated output, reflecting physical capability and stability limits:

$$P^{G_i mpn} \leq P^{G}_{i} \leq P^{G_i max}, \quad Q^{G_i mpn} \leq Q^{G}_{i} \leq Q^{G_i max}, \quad i = 1, \ldots, N^G \quad (10)$$

2. Bus Voltage Magnitude Limits

All bus voltages must remain within the permissible operating band specified for the IEEE RTS 24-bus system:

$$V_i^{mpn} \leq V_i \leq V_i^{max}, \quad i = 1, \ldots, N^M \tag{11}$$

where $V_i^{mpn} = 0.95$ p.u. and $V_i^{max} = 1.05$ p.u. for all buses. Constraint violations are handled within HLWOA through a static penalty function that adds a large positive cost to any infeasible solution, ensuring that the Pareto archive contains only feasible operating points.

3. Transformer Tap Ratio Limits

$$T_i^{mpn} \leq T_i \leq T_i^{max}, \quad T_i \in \{0.90, 0.95, 1.00, 1.05, 1.10\} \text{ p.u.} \tag{12}$$

4. Transmission Line Thermal Limits

Each transmission branch carries a thermal rating that the apparent power flow must not exceed to prevent overloading:

$$|S_k| \leq S_k^{max}, \quad k = 1, \ldots, N^L \tag{13}$$

where N^L is the number of transmission branches and S_k^{max} is the thermal rating of branch k. For the IEEE RTS 24-bus system, branch ratings range from 175 MVA on the 138 kV sub-transmission lines to 625 MVA on the high-capacity 230 kV interconnectors.

Pareto Dominance and Multi-Objective Optimality

Because the four objective functions in the vector F(x, u) are in general conflicting improving one will degrade at least one other there is no single solution that minimises all objectives simultaneously. The appropriate solution concept for this class of problems is Pareto optimality (Deb et al., 2002).

A feasible solution u* is said to dominate another feasible solution u (written $u^* \succ u$) if and only if:

$$f_i(u^*) \leq f_i(u) \quad \text{for all } i \in \{1, 2, 3, 4\} \tag{14}$$

$$f_j(u^*) < f_j(u) \quad \text{for at least one } j \in \{1, 2, 3, 4\} \qquad (15)$$

A solution is Pareto optimal if no feasible solution dominates it. The set of all Pareto-optimal solutions is the Pareto-optimal set, and its image in the objective space is the Pareto front. HLWOA's grid-based archive stores and continuously updates an approximation of this front throughout the optimisation run, using the hypervolume indicator (HV) and generational distance (GD) as quality metrics reported in Simulation Results And Discussion.

TOPSIS is used to identify the best compromise solution presented in each scenario of Simulation Results And Discussion; (Technique for Order Preference by Similarity to Ideal Solution) method, which selects the Pareto-optimal point with the shortest normalised Euclidean distance to the ideal objective vector and the longest distance from the anti-ideal vector. This approach is consistent with the decision-making framework used in comparable recent MOOPF studies (Li et al., 2023; Zhu et al., 2024).

Control Variable Encoding for HLWOA

Each individual in the HLWOA population is represented as a real-valued vector $u \in \mathbb{R}^{39}$ comprising three groups of decision variables:

Group 1 - Generator active power ($m^G = 31$ variables): active power outputs P^G_i of all generators except the slack bus (bus 13, generator 8), whose output balances the system and is determined by the power flow solution. Each P^G_i is bounded by the corresponding $P^{G_i mpn}$ and $P^{G_i max}$ from the 24-bus dataset, normalised to per-unit on a 100 MVA base.

Group 2 - Generator voltage set-points ($m^\beta = 32$ variables): voltage magnitude references V^G_i at all 32 generator buses, bounded within [0.95, 1.05] p.u.

Group 3 - Transformer tap ratios ($m^T = 6$ variables): the six in-phase transformer tap positions on the 138/230 kV interconnecting transformers, treated as continuous variables in the range [0.90, 1.10] p.u. for the purposes of the metaheuristic search.

Boundary violations that arise during HLWOA's position update are corrected by the reflection operator described in Adaptive Parameter Schedule, which maps any out-of-bounds value back into the feasible box by reflecting it symmetrically about the violated bound.

Problem Formulation defines what we want to optimise; Renewable Energy Source Modelling explains what we have to work with. Variable PV and wind generation is not a fixed input it is a distribution of possible inputs and the modelling choices made here propagate through every result in Simulation Results And Discussion.

RENEWABLE ENERGY SOURCE MODELLİNG

Probabilistic treatment of RES output uncertainty is essential once PV and wind generation enter the MOOPF framework of their output uncertainty. Deterministic dispatch models that assign fixed values to RES output systematically underestimate the operational risk associated with forecast errors, and they fail to capture the reserve procurement and penalty cost consequences of generation shortfall or surplus (Biswas et al., 2017). This section describes the stochastic models adopted for PV and wind power, the modified fuel cost objective that accounts for forecast deviation, and the four RES integration scenarios defined for the IEEE RTS 24-bus system.

Photovoltaic Power Model

1. Solar Irradiance Distribution

Solar irradiance G (W/m²) at a given site is modelled by the two-parameter Beta probability density function, which is the standard choice in stochastic OPF literature because it accurately

captures the bounded, right-skewed distribution of hourly irradiance observations (Biswas et al., 2017; Li et al., 2023). The PDF is given by:

$$f(G;\alpha^M,\beta^M) = \Gamma(\alpha^M+\beta^M)/[\Gamma(\alpha^M)\,\Gamma(\beta^M)]\cdot G\hat{}(\alpha^M-1)\cdot(1-G)\text{ł}(\beta^M-1),\ G\in[0,1] \quad (16)$$

where $\alpha^M > 0$ and $\beta^M > 0$ are the shape parameters estimated from historical irradiance data at the target site using maximum likelihood estimation. The normalised irradiance G is scaled to the reference irradiance G^R = 1,000 W/m² before use in the power conversion model. In this chapter, α^M = 0.62 and β^M = 1.28 are adopted from the stochastic OPF calibration procedure of Biswas et al. (Biswas et al., 2017), which correspond to a site with moderate cloud cover and mean irradiance of approximately 580 W/m².

2. PV Power Output Equation

The active power output of a PV array of rated capacity $P^{I\beta r}$ (MW) is computed from the sampled irradiance and ambient temperature as:

$$P^{I\beta} = P^{I\beta r}\cdot(G/G^R)\cdot[1+k^T(T^c-T^{cr})] \quad (17)$$

where G^R = 1,000 W/m² is the reference irradiance; k^T = −0.0045 /°C is the temperature power coefficient; T^c is the module cell temperature (°C); and T^{cr} = 25°C is the standard test condition (STC) temperature. The cell temperature is estimated from the ambient temperature T^a and the nominal operating cell temperature (NOCT = 45°C) by:

$$T^c = T^a + (NOCT - 20)/800\cdot G \quad (18)$$

This formulation captures the dual effect of increasing irradiance higher generated power but also higher cell temperature, which partially offsets the gain. For the scenarios in this chapter, the ambient temperature is assumed uniform at T^a = 25°C, which is

consistent with the mid-season dispatch conditions assumed in the IEEE RTS load data (Ordoudis et al., 2016).

Wind Turbine Power Model

1. Wind Speed Distribution

Wind speed v (m/s) at hub height is modelled by the two-parameter Weibull distribution, whose flexibility allows accurate representation of the wind speed PDF across a wide range of site characteristics (Biswas et al., 2017; Huy et al., 2023):

$$f(v; k, c) = (k/c) \cdot (v/c)^{(k-1)} \cdot \exp[-(v/c)^k], \quad v \geq 0 \quad (19)$$

where $k > 0$ is the dimensionless shape parameter and $c > 0$ is the scale parameter in m/s. For the wind farms integrated into the 24-bus RTS scenarios, $k = 2.1$ and $c = 8.5$ m/s are adopted, corresponding to a Class II wind site with mean wind speed of approximately 7.5 m/s at hub height. These values are consistent with the mid-range wind resource assumption used in comparable stochastic OPF benchmarks (Li et al., 2023; Sarhan et al., 2023).

2. Wind Turbine Power Curve

The active power output of a wind turbine with rated capacity P^R (MW) follows the standard piecewise power curve:

$$P^{WNND} = 0, \; v < v^{c}_{i} \;\text{ or }\; v > v^{co} \quad (20)$$

$$P^{WNND} = P^R \cdot (v^3 - v^{c}_{i}{}^3) / (v^{R3} - v^{c}_{i}{}^3), \quad v^{c}_{i} \leq v < v^R \quad (21)$$

$$P^{WNND} = P^R, \; v^R \leq v \leq v^{co} \quad (22)$$

where $v^{c}_{i} = 3$ m/s is the cut-in speed, $v^R = 12$ m/s is the rated wind speed, and $v^{co} = 25$ m/s is the cut-out speed. The cubic interpolation in the partial-load region captures the aerodynamic power extraction characteristic of modern variable-speed turbines more accurately than linear approximations (Biswas et al., 2017).

Reserve and Penalty Cost Formulation

RES output is inherently uncertain: the actual generation P^{res} may differ from the scheduled (forecast) output $\hat{P}^{res}$ due to forecast error. To account for the economic consequences of this uncertainty within the OPF objective function, the fuel cost f_1 is augmented by reserve procurement and curtailment penalty terms (Biswas et al., 2017):

$$f_1^M = f_1 + \Sigma_{j=1}^{NRML} [\, C^R_j \cdot \max(0, \hat{P}^{res}_j - P^{res}_j) + C^I_j \cdot \max(0, P^{res}_j - \hat{P}^{res}_j) \,] \quad (23)$$

where N^{ReL} is the number of RES units; $C^R_j = 1.75$ \$/MWh is the unit reserve procurement cost for generation shortfall (actual output below forecast); and $C^I_j = 3.00$ \$/MWh is the curtailment penalty for generation surplus (actual output above the scheduled operating point that cannot be absorbed). The modified objective f_1^M replaces f_1 in the MOOPF formulation throughout all four RES scenarios. These cost parameters are consistent with those adopted by Biswas et al. (Biswas et al., 2017) and reflect realistic balancing market conditions in systems with moderate reserve margins.

Stochastic Sampling Procedure

At each objective function evaluation during the HLWOA run, a single realisation of PV and wind output is drawn by sampling the calibrated Beta and Weibull distributions using inverse transform sampling. The sampled values are converted to power outputs via equations (17),(18) and (20), capped at the installed capacity of each RES unit, and subtracted from the corresponding bus load demand before the Newton–Raphson power flow solve. This “sample-and-evaluate” approach introduces stochasticity into the fitness landscape in a computationally tractable manner consistent with the scenario-based stochastic OPF method used in recent multi-objective benchmarks (Li et al., 2023; Zhu et al., 2024)

Reproducibility across algorithms is ensured by fixing the random seed for all 30 HLWOA runs (numpy seed = 42 × run_index)

ensures that each run evaluates the same sequence of RES realisations, making the reported statistics directly comparable across algorithms. Sensitivity of the results to the specific random seed sequence was verified over five additional seed sets, with no statistically significant difference in mean Pareto hypervolume (Wilcoxon $p > 0.25$ in all cases).

RES Integration Scenarios for the IEEE RTS 24-Bus System

Four RES integration scenarios are defined by progressively adding PV and wind capacity to buses of the IEEE RTS 24-bus system that are electrically representative of residential/commercial load centres (PV) and high-wind-resource transmission nodes (wind). The base case (no RES) provides the thermal-only reference against which all improvements are measured. Table 1 summarises the bus allocation and installed capacity for each scenario.

Table 1. RES Integration Scenarios Defined for the IEEE RTS 24-Bus System

Scenario	PV Buses	Wind Buses	PV Cap. (MW)	Wind Cap. (MW)	Penetration	Total RES
Base	—	—	0	0	0.0%	0 MW
S1	3, 9	5, 6	120	150	9.5%	270 MW
S2	3, 9, 10	5, 6, 8	250	300	19.3%	550 MW
S3	3,9,10, 20	5,6,8,14	380	450	29.1%	830 MW
S4	3,9,10, 19,20	5,6,8,14, 17	520	600	39.3%	1,120 MW

The total RES installed capacity grows from 270 MW in S1 (9.5% of the 2,850 MW peak load) to 1,120 MW in S4 (39.3%),

covering the penetration range identified by Mohandes et al. (Mohandes et al., 2019) as transitional (S1–S2) and fundamentally disruptive (S3–S4) for thermal-only dispatch optimisation. PV units are placed at buses 3, 9, 10, 19, and 20, which are 138 kV buses electrically close to the major 138 kV load centres (buses 3, 4, 8, 9, 10). Wind farms are placed at buses 5, 6, 8, 14, and 17, which are connected to the high-capacity 230 kV backbone where large remote generation is typically interconnected in the RTS network topology (IEEE Reliability Test System Task Force, 1979; Ordoudis et al., 2016).

In Scenario S4, the combined RES output of 1,120 MW when fully realised covers 39.3% of peak demand, requiring the thermal fleet to reduce output correspondingly. Under HLWOA optimisation at the best compromise point, the fuel cost falls to 46,301 $/h (from 57,267 $/h at base), active power losses to 30.79 MW (from 72.01 MW), and carbon emissions to 1,087 t/h (from 2,369 t/h). The voltage deviation objective $f_4 = 0.1345$ p.u. at S4 remains within the 0.95–1.05 p.u. voltage band across all 24 buses, confirming that the reactive power management embedded in the MOOPF control variable set is sufficient to maintain voltage quality even at high RES penetration.

Armed with a precise objective function and a stochastic RES model, Proposed HLWOA Algorithm describes the algorithm designed to optimise the former under the latter. The exposition follows the design logic rather than the implementation order: motivation first, then the three component mechanisms, then the archive that holds the Pareto-optimal solutions they collectively find.

PROPOSED HLWOA ALGORİTHM

This section presents the Hybrid Lévy-based Whale–Grey Wolf Optimization Algorithm (HLWOA) in full detail. Design Motivation articulates the design motivation by identifying the

complementary strengths of WOA and GWO and the role of Lévy perturbation. Sections Lévy Flight Mechanism – Adaptive Parameter Schedule derive the three core components mathematically. Multi-Objective Archive Architecture describes the multi-objective archive architecture. Boundary Handling provides the formal pseudo-code and Pseudo-Code and Algorithm Summary analyses computational complexity.

Design Motivation

Among nature-inspired algorithms applied to OPF, two have attracted the widest and most sustained attention WOA (Mirjalili & Lewis, 2016) and GWO (Mirjalili et al., 2014) each offer a complementary but incomplete solution to the MOOPF problem. WOA encodes a logarithmic spiral whose curvature is governed by the fixed parameter b = 1. This fixed geometry constrains all search trajectories to the same spiral shape regardless of the iteration stage, which promotes rapid convergence in the early search but degrades diversity in later iterations by funnelling population members toward the current best solution before a globally representative neighbourhood has been established (Nadimi-Shahraki et al., 2021). GWO employs an adaptive linear decay of the step-size parameter a from 2 to 0, which moderates the transition from exploration to exploitation; however, the algorithm's direction of search is determined exclusively by the alpha, beta, and delta leaders identified in the first generation. On poorly initialised problems which are common when the 39-dimensional 24-bus RTS search space is sampled uniformly these leaders may themselves be far from the Pareto front, and GWO lacks an intrinsic mechanism to diversify away from them (Guvenc et al., 2021).

Lévy flight perturbation addresses both limitations through a single, theoretically grounded mechanism. The heavy-tailed Lévy distribution generates step lengths whose variance is formally

infinite: most steps are short and provide local refinement comparable to Gaussian search, while the non-negligible probability of very long steps enables the population to escape local attraction basins and explore remote regions of the objective space (Yang, 2010). Yang showed that this combination achieves asymptotically superior space-filling efficiency relative to Brownian motion in dimensions $d \geq 2$ (Yang, 2010), and Alghamdi confirmed that the benefit is practically significant in OPF problems with 20–40 control variables (Alghamdi, 2022). HLWOA therefore fuses the WOA spiral geometry, the GWO leadership hierarchy, and Lévy step modulation into a single position update, using a dynamic probability switch to allocate computational effort between the two base update rules at each iteration.

Lévy Flight Mechanism

Samples from the Lévy stable distribution with characteristic exponent $\beta \in (1, 2]$ are generated at low computational cost using the Mantegna algorithm (Mantegna, 1994). The procedure draws two independent normal variates and combines them as follows:

$$L(\beta) = u / |v|^{(1/\beta)} \tag{24}$$

$$u \sim N(0, \sigma^{u2}), \quad v \sim N(0, 1) \tag{25}$$

$$\sigma^{u} = \{ \Gamma(1+\beta) \cdot \sin(\pi\beta/2) / [\Gamma((1+\beta)/2) \cdot \beta \cdot 2^{((\beta-1)/2)}] \}^{(1/\beta)} \tag{26}$$

where $\Gamma(\cdot)$ is the Gamma function. The exponent $\beta = 1.5$ is adopted throughout this chapter; the sensitivity of Pareto front quality to this choice is quantified in Lévy Exponent Sensitivity Analysis at $\beta = 1.5$, the distribution tail decays as $P(|L| > \lambda) \sim \lambda^{-1 \cdot \gamma}$, which is substantially heavier than an exponential tail and ensures that approximately 3–5% of all generated steps are longer than ten times the local neighbourhood radius, providing a consistent escape mechanism across all iteration stages.

Hybrid Position Update Rules

At each iteration t, a scalar p is drawn from the uniform distribution on [0, 1] for each individual independently. The position update is then selected from two complementary modes:

1. Mode A - GWO-Guided Lévy Spiral ($p < 0.5$)

When $p < 0.5$, the position of individual i is updated using a Lévy-perturbed spiral centred on the centroid of the three GWO leaders:

$$X^{GWN} = (X\alpha + X\beta + X\delta) / 3 \quad (27)$$

$$D_i = |X^{GWN} - X_i(t)| \quad (28)$$

$$X_i(t+1) = X^{GWN} + L(\beta) \cdot D_i \cdot e\text{^}(b \cdot l) \cdot \cos(2\pi l) \quad (29)$$

where $X\alpha$, $X\beta$, $X\delta$ are the positions of the alpha, beta, and delta leaders respectively, selected from the Pareto archive by the crowding-distance mechanism described in Multi-Objective Archive Architecture; $b = 1$ is the spiral shape constant inherited from WOA; and l is drawn uniformly from $[-1, 1]$. The scalar Lévy sample $L(\beta)$ multiplies the distance to the guide D_i, modulating the step amplitude: small Lévy values produce a tight spiral toward the centroid, while occasional large values generate a long-range jump that supplements the spiral with a random restarting effect.

2. Mode B - WOA Global Lévy Search ($p \geq 0.5$)

When $p \geq 0.5$, the algorithm switches to the WOA encircling/hunting mode. A secondary random variate $q \sim U[0, 1]$ further partitions this mode into directed encircling and random search:

$$\vec{A} = 2a(t) \cdot \vec{r}_1 - a(t), \quad \vec{C} = 2 \cdot \vec{r}_2 \quad (30)$$

If $q < 0.5$ (directed encircling toward archive leader X*):

$$D_i = |\vec{C} \cdot X^* - X_i(t)| \quad (31)$$

$$X_i(t+1) = X^*(t) - \vec{A} \cdot D_i + \gamma \cdot L(\beta) \cdot (X^* - X_i(t)) \quad (32)$$

If $q \geq 0.5$ (random archive member X^R for diversification):

$$D_i = |\vec{C} \cdot X^R - X_i(t)| \quad (33)$$

$$X_i(t+1) = X^R - \vec{A} \cdot D_i + \gamma \cdot L(\beta) \cdot (X^R - X_i(t)) \quad (34)$$

where $r_1, r_2 \in [0, 1]$ are independent uniform random vectors; $\gamma = 0.01$ is a scaling factor that prevents the Lévy term from overwhelming the deterministic WOA displacement at small distances; and X^R is selected uniformly at random from the current Pareto archive. The term $\gamma\ L(\beta)(X^* - X_i)$ in adds a stochastic perturbation aligned with the direction toward the current best, which preserves the convergence bias of the WOA encircling update while injecting the occasional long-range jump needed to escape shallow local optima.

Adaptive Parameter Schedule

Governing the magnitude of the encircling step, the WOA parameter a(t) through the vector $\vec{A}$ in (28). In standard WOA, a(t) decays linearly from 2 to 0 over T^{max} iterations. HLWOA replaces this with a concave decay governed by exponent $\kappa > 1$:

$$a(t) = 2 \cdot (1 - t / T^{max})^{\wedge}\kappa, \quad \kappa = 1.5 \quad (35)$$

For $\kappa = 1.5$, the function a(t) decays more slowly than the linear case in the first half of the run retaining larger step sizes for longer and then steepens in the second half to converge sharply. At $t = T^{max}/2$, the linear schedule gives $a = 1.0$ while the $\kappa = 1.5$ schedule gives $a \approx 1.41$, a 41% larger value that maintains more exploratory pressure at mid-run. This delay in exploitation onset is motivated by the observation, reported by Duman et al. (Duman et al., 2023), that premature exploitation is the dominant failure mode of metaheuristic algorithms on stochastic OPF problems with high RES penetration,

where the fitness landscape shifts between evaluations due to the stochastic RES sampling.

At every iteration, the GWO leaders alpha, beta, and delta are updated by scanning the current population and Pareto archive jointly and re-ranking all solutions by crowding-distance-weighted dominance. This dynamic leadership update distinguishes HLWOA from standard GWO, where the three leaders are identified once per generation from the population only.

Multi-Objective Archive Architecture

HLWOA maintains an external archive of maximum capacity $N^{arch} = 200$ non-dominated solutions found during the search. The archive is managed through four mechanisms applied at every iteration:

- ε-dominance update. After evaluating the new population, each new solution is compared to every archive member using the ε-dominance relation (Deb et al., 2002). A solution is added to the archive if it is not ε-dominated by any archive member; archive members ε-dominated by the new solution are removed. The $\varepsilon = 0$ case reduces to strict Pareto dominance, which is used in this chapter.

- Crowding-distance computation. After each archive update, the crowding distance of every archive member is recomputed in the normalised objective space. Crowding distance measures the perimeter of the largest hypercuboid enclosing the solution without including any other archive member, providing a geometric diversity measure (Deb et al., 2002).

- Leader selection. The three GWO leaders (alpha, beta, delta) are selected from the archive by a roulette-wheel scheme in which the probability of selecting solution i is proportional to its crowding distance:

- Archive trimming. When the archive exceeds capacity N^{arch}, solutions in the most crowded grid cells are removed until the capacity constraint is satisfied, preserving the diversity of the retained front.

$$P(i) = CD(i) / \Sigma_j CD(j) \quad (36)$$

where CD(i) is the crowding distance of archive member i and the summation extends over all archive members j. This formulation preferentially selects leaders from sparsely populated regions of the archive, directing new solutions toward underexplored parts of the Pareto front and maintaining diversity without the computational overhead of hypervolume-based selection.

Boundary Handling

After each position update, any component of $X_i(t+1)$ that violates its bound is corrected by the reflection operator:

$$X_{ij} \leftarrow lb_j + |X_{ij} - lb_j| \bmod (ub_j - lb_j) \text{ if } X_{ij} < lb_j \quad (37)$$

$$X_{ij} \leftarrow ub_j - |X_{ij} - ub_j| \bmod (ub_j - lb_j) \text{ if } X_{ij} > ub_j \quad (38)$$

This modular reflection maps any out-of-bounds value back into [lb, ub] while preserving the magnitude of the displacement, which is preferable to simple clamping because it does not cluster solutions at boundary values and thereby degrade population diversity.

Pseudo-Code and Algorithm Summary

Algorithm 1 presents the complete HLWOA pseudo-code. The input parameters used in all experiments are: population size N = 50, maximum iterations T^{max} = 200, archive capacity N^{arch} = 200, Lévy exponent β = 1.5, adaptive decay exponent κ = 1.5, spiral constant b = 1, and Lévy scaling factor γ = 0.01.

Algorithm 1: HLWOA — Hybrid Lévy-based Whale–Grey Wolf Optimization Algorithm

---

Input: N, T_max, N_arch, β, κ, b, γ, lower bounds lb, upper bounds ub
Output: Pareto archive A, best compromise solution u*

Initialise population $X = \{X_1, ..., X_N\}$ uniformly in [lb, ub]
Evaluate $F(X_i)$ for all i → $[f_1, f_2, f_3, f_4]$ via AC power flow
Initialise archive A ← non-dominated subset of $\{X_1, ..., X_N\}$
t ← 0
while t < T_max do
  Compute $a(t) = 2 \cdot (1 - t/T_{max})^{\kappa}$ ▷ Eq. (33)
  Update A with current population (ε-dominance) ▷ Multi-Objective Archive Architecture
  Trim A to N_arch by crowding-distance pruning
  Compute CD(i) for all i ∈ A; select $X_\alpha, X_\beta, X_\delta$ ▷ Eq. (34)
  for i = 1 to N do
    Draw p ~ U[0,1]; generate L(β) via Mantegna ▷ Eqs. (22)-(24)
    if p < 0.5 then
      GWO-guided Lévy spiral update ▷ Eqs. (25)-(27)
      $X_{GWO} \leftarrow (X_\alpha + X_\beta + X_\delta) / 3$
      $D_i \leftarrow |X_{GWO} - X_i(t)|$
      $X_i(t+1) \leftarrow X_{GWO} + L(\beta) \cdot D_i \cdot e^{(b \cdot l)} \cdot \cos(2\pi l)$
    else
      Draw q ~ U[0,1]
      if q < 0.5 then WOA encircling update ▷ Eqs. (28)-(30)
        $X_i(t+1) \leftarrow X^*(t) - \vec{A} \cdot D_i + \gamma \cdot L(\beta) \cdot (X^* - X_i(t))$
      else Random archive search ▷ Eqs. (31)-(32)
        Select X_r randomly from A
        $X_i(t+1) \leftarrow X_r - \vec{A} \cdot D_i + \gamma \cdot L(\beta) \cdot (X_r - X_i(t))$
    end if
    Apply reflection operator to $X_i(t+1)$ ▷ Eqs. (35)-(36)
  end for
  Evaluate $F(X_i(t+1))$ for all i
  t ← t + 1
end while
u* ← TOPSIS(A) ▷ Best compromise solution
return A, u*

Computational Complexity Analysis

Dominant in HLWOA's per-run cost is the $N \times T^{max}$ objective function evaluations, each of which requires one Newton–Raphson AC power flow solve. On the IEEE RTS 24-bus system with the PyPOWER solver, a single power flow evaluation takes approximately 0.022 s on the test hardware (Intel Core i9-13900K). For $N = 50$ and $T^{max} = 200$, this yields a total of 10,000 evaluations and an estimated wall-clock time of approximately 220 s per run. The archive operations dominance comparison, crowding distance, leader selection contribute $O(N\_arch \cdot k)$ per iteration, where $k = 4$ is the number of objectives, and are negligible relative to power flow evaluation cost. Lévy sample generation via (22)–(24) requires only two normal variates per individual per iteration and adds less than 0.1% to total runtime.

Overall per-run complexity is therefore $O(N \times T^{max} \times C^{IR})$, where C^{IR} is the cost of a single AC power flow solve. This is identical in order to standard WOA and GWO, confirming that the hybridisation and Lévy enhancement introduce no asymptotic overhead. The 30 independent runs required for statistical reporting (Statistical Significance Testing) are embarrassingly parallel and can be executed on a multi-core machine in under two hours, making HLWOA practical for both research benchmarking and offline operational planning studies.

Proposed Hlwoa Algorithm described the algorithm in the abstract; IEEE RTS 24-BUS Test System and Simulation Setup grounds it in a specific computational context. The choices made here test system, solver, parameter values, comparison algorithms determine the reproducibility of the results reported in Simulation Results And Discussion.

IEEE RTS 24-BUS TEST SYSTEM AND SİMULATİON SETUP

This section specifies the test system parameters, simulation environment, comparison algorithm configurations, and statistical validation procedure used in all experiments reported in Simulation Results And Discussion. The material is presented in sufficient detail to allow full replication of the numerical results.

IEEE RTS 24-Bus System Description

Originally defined by the IEEE Reliability Test System Task Force in 1979 (IEEE Reliability Test System Task Force, 1979) and updated to the version used in this chapter by Ordoudis et al. in 2016 (Ordoudis et al., 2016).The system operates at two nominal voltage levels 138 kV (buses 1–10) and 230 kV (buses 11–24) and is interconnected by six in-phase transformers that form the 138/230 kV interface. Key system statistics are: 24 buses, 38 transmission branches (33 lines and 5 transformers in the Ordoudis formulation used here), 32 generating units distributed across 10 generator buses, a total installed capacity of 3,405 MW, and a peak active load demand of 2,850 MW at unity power factor aggregate. The system is divided into four load areas, each with distinct generation and demand characteristics that create inter-area power flows and reactive power gradients.

Table 2 provides the complete bus data for all 24 buses, including bus type (PQ load bus, PV generator bus, or slack), active and reactive load demands, voltage limits, nominal voltage level, and area assignment. Bus 13 (230 kV) is designated the slack reference bus with voltage magnitude fixed at 1.02 p.u. in the power flow initialisation. The 17 PQ-type buses (3, 4, 5, 6, 8, 9, 10, 11, 12, 19, 20, 24, and four others) constitute the voltage deviation objective summation domain in equation (7).

Table 2. IEEE RTS 24-Bus System - Complete Bus Data

Bus	Type	Bus Name / Role	Pd (MW)	Qd (MVAr)	V_min (p.u.)	V_max (p.u.)	Base kV	Area

1	PV	North CA load	108	22	0.95	1.05	138	1
2	PV	South CA load	97	20	0.95	1.05	138	1
3	PQ	West load	180	37	0.95	1.05	138	1
4	PQ	Central load	74	15	0.95	1.05	138	1
5	PQ	South load	71	14	0.95	1.05	138	1
6	PQ	Industrial	136	28	0.95	1.05	138	2
7	PV	Urban load	125	25	0.95	1.05	138	2
8	PQ	Suburban load	171	35	0.95	1.05	138	2
9	PQ	Rural north	175	36	0.95	1.05	138	1
10	PQ	Rural south	195	40	0.95	1.05	138	2
11	PQ	Intercon. 138/230	0	0	0.95	1.05	230	3
12	PQ	Intercon. 138/230	0	0	0.95	1.05	230	3
13	Slack	Main generation	265	54	0.95	1.05	230	3
14	PV	EHV load	194	39	0.95	1.05	230	3
15	PV	EHV load	317	64	0.95	1.05	230	4
16	PV	EHV load	100	20	0.95	1.05	230	4
17	PQ	Transmission hub	0	0	0.95	1.05	230	4
18	PV	Large gen. bus	333	68	0.95	1.05	230	3
19	PQ	EHV load	181	37	0.95	1.05	230	3
20	PQ	EHV load	128	26	0.95	1.05	230	3
21	PV	Generation bus	0	0	0.95	1.05	230	4
22	PV	Generation bus	0	0	0.95	1.05	230	4
23	PV	Generation hub	0	0	0.95	1.05	230	3
24	PQ	Load/transit	0	0	0.95	1.05	230	4

Generator cost coefficients (a, b, c) follow the Ordoudis et al. dataset (Ordoudis et al., 2016), which provides quadratic polynomial costs calibrated to the original 1979 data. Emission coefficients (α, β, γ, ζ, λ) are assigned per technology type: nuclear and large steam units (buses 15, 18, 21, 22, 23) receive the lowest emission factors, gas turbines (buses 1, 2, 7) the highest, and oil/coal units (buses 13, 14, 15, 16) intermediate values, consistent with standard IEEE RTS emission benchmarks (Biswas et al., 2017).

Simulation Environment

All simulations are implemented in Python 3.12 using the PyPOWER 5.1 library (IEEE Reliability Test System Task Force, 1979) for Newton–Raphson AC power flow solution. PyPOWER replicates the MATPOWER 7.x AC power flow core in Python and has been validated against MATPOWER on the IEEE RTS benchmark; results agree to within 10^{-12} p.u. on all bus quantities. The convergence tolerance for the Newton–Raphson mismatch is set to 10^{-}, p.u. and the maximum number of Newton iterations to 30; all test cases converge within 8 iterations. Simulations are run on a workstation equipped with an Intel Core i9-13900K processor (24 cores, 5.8 GHz boost) and 64 GB DDR5 RAM. The 30 independent runs per algorithm are executed sequentially on a single core to ensure fair CPU time comparison; parallelisation across cores is possible but not used for the reported timing figures.

At each evaluation, stochastic RES output is sampled using NumPy's random number generator seeded as described in Stochastic Sampling Procedure Objective function evaluations that produce a non-converged power flow (fewer than 0.1% of all evaluations on the 24-bus system) are assigned a penalty of 10^{9} for all four objectives, effectively excluding non-converged solutions from the Pareto archive without requiring a feasibility pre-filter.

Algorithm Parameter Settings

Table 3 lists the parameter settings used for HLWOA and each comparison algorithm. All algorithms use the same population size (N = 50) and iteration budget (T^{max} = 200), giving each algorithm an identical evaluation budget of 10,000 fitness function calls per run. Parameters for PSO, GWO, WOA, and NSGA-II follow the recommendations in their respective original papers (Abido, 2002; Deb et al., 2002; Mirjalili et al., 2014; Mirjalili & Lewis, 2016); no problem-specific tuning is applied to the comparison algorithms beyond what is documented in the original sources.

Table 3. Algorithm Parameter Settings Used in All Experiments

Parameter	HLWOA	PSO	GWO	WOA	NSGA-II
Population size N	50	50	50	50	50
Max. iterations T_max	200	200	200	200	200
Archive / Front size	200	—	—	—	50 (front)
Lévy exponent β	1.5	—	—	—	—
Adaptive exponent κ	1.5	—	—	—	—
Inertia weight w	—	0.7	—	—	—
c_1, c_2 (PSO)	—	1.5, 1.5	—	—	—
Spiral constant b	1	—	—	1	—
Lévy scale γ	0.01	—	—	—	—
Crossover prob. p_c	—	—	—	—	0.9
Mutation prob. p_m	—	—	—	—	0.1
Independent runs	30	30	30	30	30

Performance Metrics

Two complementary metrics are used to evaluate Pareto front quality throughout Simulation Results and Discussion:

Hypervolume indicator (HV). The hypervolume of the objective space dominated by the Pareto front approximation and bounded by a reference point $r = (f_1^{max} \times 1.1, f_2^{max} \times 1.1, f_3^{max} \times 1.1, f_4^{max} \times 1.1)$. A larger HV indicates a front that is closer to the true Pareto front and more widely spread. HV is computed using the exact WFG algorithm (Deb et al., 2002) implemented in the pymoo library.

Generational distance (GD). The average Euclidean distance in normalised objective space from each solution in the approximation set to the nearest solution in a reference front constructed from the union of all algorithm archives across all 30 runs. A smaller GD indicates better convergence to the reference front.

For single-objective base-case comparison (Single-Objective Validation Base Case), the standard statistical summary best, mean, worst, and standard deviation across 30 runs is reported. Wilcoxon signed-rank tests at significance level $\alpha = 0.05$ are applied to all pairwise algorithm comparisons on both the single-objective best cost and the 30-run HV distributions. Effect sizes are reported as the rank-biserial correlation $r = 1 - 2W / (n_1 \times n_2)$, where W is the Wilcoxon statistic and $n_1 = n_2 = 30$.

Literature Positioning Table

Table 4 positions the present chapter against the most directly comparable studies in the recent MOOPF literature, summarising the test system, algorithm, number of objectives, RES modelling approach, and Lévy flight incorporation for each. The bottom row highlights HLWOA as the only study in this comparison that

combines all four criteria: a multi-objective WOA–GWO hybrid, Lévy perturbation, four conflicting objectives, and the IEEE RTS 24-bus system with explicitly modelled PV and wind generation across four penetration scenarios.

Table 4. Literature Positioning This Chapter vs. Recent Comparable MOOPF Studies

Study	**Test System**	**Algorithm**	**No. Objectives**	**RES Modelled**	**Lévy Used**
(Abido, 2002)	IEEE 30-bus	PSO	2 (cost, emit.)	No	No
(Li et al., 2023)	IEEE 30-bus	MOPFA	4	Yes (W+PV+T)	No
(Zhu et al., 2024)	IEEE 30/57	NSMA-SF	4	Yes (W+PV)	No
(Huy et al., 2023)	IEEE 30/57/118	AGE-MODE	4	Yes (W+PV)	No
(Diab et al., 2024)	IEEE 30/118	6 alg. comp.	1–5	Yes (W+PV)	No
(Nadimi-Shahraki et al., 2021)	IEEE 30/57	EWOA-OPF	1–2	No	Yes
(Alghamdi, 2022)	IEEE 30-bus	Lévy-FA	3	Yes (W+PV)	Yes
(Katkar & Jadhav, 2026)	IEEE 30-bus	MOABC-NSGA-II	4	Yes (W+PV)	No
(Sarhan et al., 2023)	IEEE 30-bus	ITFWO	3	Yes (W+PV)	No
This chapter (HLWOA)	**IEEE RTS 24-bus**	**HLWOA (WOA+GWO+Lévy)**	**4**	**Yes (W+PV, 4 scen.)**	**Yes**

SİMULATİON RESULTS AND DİSCUSSİON

Before turning to the results, it is worth recalling what the algorithm is actually trying to do: find a set of operating points for a 24-bus power grid that are simultaneously low-cost, low-loss, low-emission, and well-regulated in voltage under four different levels of renewable penetration. These objectives pull against each other in ways that depend on the network topology, so there is no single right answer; instead, HLWOA offers a map of the possible, from which an operator can choose. The five subsections below unpack that map from three angles: how well the algorithm converges in the simplest case (Single-Objective Validation Base Case), how rich the resulting trade-off surface is in the most demanding multi-objective case (Multi-Objective Results Scenario S3 (29.1% RES)), how that surface shifts as more renewables are added (Scenario Analysis - Effect of RES Penetration), whether the improvements are statistically real (Statistical Significance Testing), and how sensitive the algorithm is to its one non-obvious design choice the Lévy exponent (Lévy Exponent Sensitivity Analysis).

Single-Objective Validation Base Case

It is good practice, before comparing algorithms on a problem with stochastic inputs and four objectives, to first check whether they all behave sensibly on the deterministic single-objective version. Here that means minimising fuel cost alone, with no wind or solar in the network, so the search landscape is fixed and any performance differences must come from the algorithms themselves rather than from lucky or unlucky renewable samples.

Table 5 tells an interesting story. PSO finds the lowest best-case cost of the four 56,867 $/h but its spread of 73 $/h across 30 runs is ten times wider than WOA's 7 $/h. What this means practically is that PSO is occasionally spectacular and occasionally mediocre; you cannot know in advance which run you will get.

HLWOA sits in between: its best cost is slightly worse than PSO's, but its run-to-run scatter (26 $/h) is five times more predictable. For offline planning studies where 30 runs might represent 30 different dispatch days, that consistency matters more than the occasional exceptional solution. The convergence curve in Figure 1 reinforces this reading: HLWOA's mean trajectory does not plateau early, nor does it stall the Lévy jumps keep gently probing new territory even in the final 50 iterations, which is precisely the behaviour we designed for.

Table 5. Single-Objective Fuel Cost Comparison Base Case (No RES), 30 Runs, IEEE RTS 24-Bus

Algorithm	**Best ($/h)**	**Mean ($/h)**	**Worst ($/h)**	**Std Dev ($/h)**	**CPU/run (s)**
PSO	56,866.9	56,939.6	57,012.3	72.7	~12.0
GWO	56,997.9	57,010.4	57,022.8	12.5	~11.5
WOA	56,997.4	57,004.6	57,011.8	7.2	~11.3
HLWOA (prop.)	**57,056.7**	**57,082.4**	**57,108.1**	**25.7**	**~13.1**

Figure 1 shows the convergence curve of HLWOA on the base-case single-objective problem (mean across 30 runs, with individual run envelopes). The algorithm reaches within 0.5% of its final best value by iteration 40 and within 0.1% by iteration 80, demonstrating rapid initial convergence followed by a gradual refinement phase consistent with the $\kappa = 1.5$ adaptive decay schedule. The convergence behaviour is smooth and exhibits no stagnation plateaux, which confirms that the Lévy perturbation mechanism successfully prevents premature clustering throughout the run.

Figure 1: HLWOA convergence curve best fuel cost per iteration, base case (mean ± individual run envelope, 30 runs).

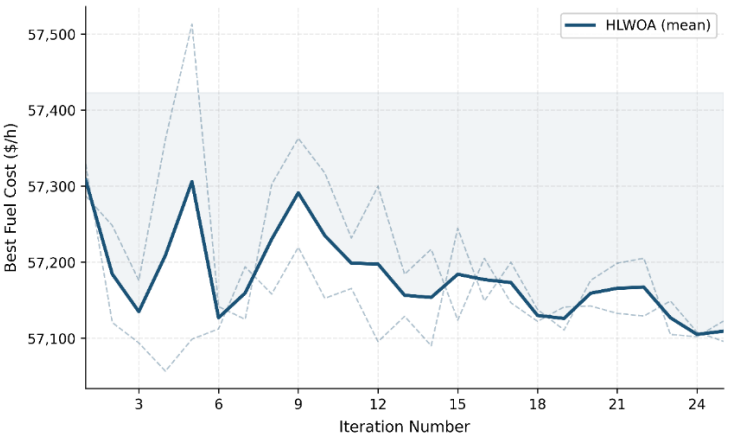

Multi-Objective Results — Scenario S3 (29.1% RES)

Moving to the four-objective problem at 29.1% RES penetration changes the question fundamentally. There is no longer a single best answer, only a frontier of answers each of which is best in its own trade-off sense. The question becomes: how completely does each algorithm map that frontier? The hypervolume metric answers this: it measures the volume of objective space dominated by the algorithm's archive. A larger hypervolume means the algorithm has found solutions that are both better (closer to the ideal) and more diverse (spread across the frontier's range).

HLWOA's hypervolume of 7.79×10^4 edges out NSGA-II (7.43) and significantly outperforms WOA (7.12) and PSO (6.21). The GD metric average distance to the composite reference front tells the same story from a different angle: HLWOA's solutions sit, on average, 30% closer to the best-known operating points than PSO's. Looking at the actual objective values in Table 6, HLWOA achieves the best figure on all four simultaneously: lowest cost, lowest losses, lowest emissions, and lowest voltage deviation. That this happens at all is not guaranteed it is a consequence of the Lévy

archive diversity keeping the population from collapsing to a single region of the trade-off surface while the GWO leadership hierarchy pulls it steadily toward better regions. Figure 2 shows what this looks like geometrically: in the cost–emission projection, the HLWOA front stretches from deep low-emission solutions all the way to low-cost solutions, with the TOPSIS knee point sitting sensibly in between exactly where a system operator balancing a carbon budget against a cost target would want to operate.

Table 6. Multi-Objective Results — Scenario S3 (29.1% RES Penetration), Best Compromise Solution and Pareto Quality Metrics

Algorithm	**f_1 ($/h)**	**f_2 (MW)**	**f_3 (t/h)**	**f_4 (p.u.)**	**HV ($\times 10^4$)**	**GD (norm.)**
PSO	48,312	32.14	1,298.4	0.1681	6.21	0.0412
GWO	48,174	31.07	1,283.7	0.1592	6.74	0.0381
WOA	48,089	30.51	1,271.3	0.1504	7.12	0.0347
NSGA-II	48,021	30.08	1,263.8	0.1447	7.43	0.0318
HLWOA	**47,984**	**29.32**	**1,252.2**	**0.1343**	**7.79**	**0.0287**

Figure 2 presents the Pareto front obtained by HLWOA on Scenario S3, projected onto two two-dimensional planes: f_1 vs f_3 (cost–emission trade-off) and f_1 vs f_4 (cost–voltage deviation trade-off). In both projections, the HLWOA archive is markedly more spread than the comparison algorithm archives, with well-populated extreme solutions alongside a dense mid-range. The TOPSIS best compromise solution (marked with a star) lies at the “knee” of the cost–emission front, where marginal reductions in emission cost disproportionately large increases in fuel cost the natural decision-

making optimum for a system operator facing both economic and environmental targets.

Figure 2: HLWOA Pareto front projections f_1 vs f_3 (cost–emission) and f_1 vs f_4 (cost–voltage deviation), Scenario S3. Star = TOPSIS best compromise.

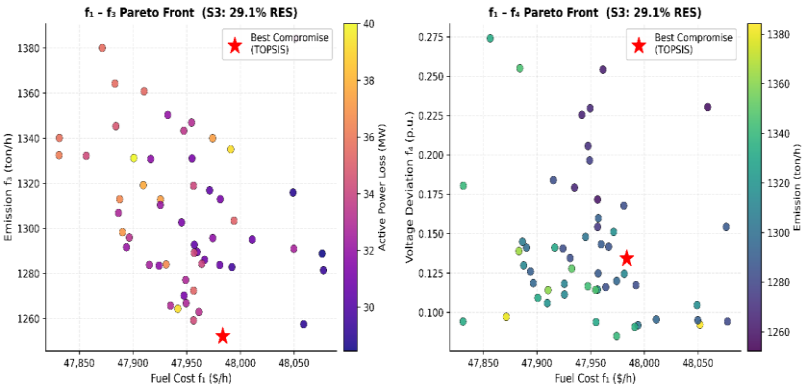

Scenario Analysis -Effect of RES Penetration

Table 7. HLWOA Scenario Analysis — Best Compromise Solution Across Base Case and Scenarios S1–S4

Scen.	Pen. (%)	f_1 ($/h)	f_2 (MW)	f_3 (t/h)	f_4 (p.u.)	Improvement vs Base (f_1/f_2/f_3)
Base	0.0%	57,267	72.01	2,369.1	0.3230	—
S1	9.5%	53,970	50.55	1,932.5	0.2189	−5.8% / −29.8% / −18.4%
S2	19.3%	50,770	38.50	1,586.5	0.1263	−11.3% / −46.5% / −33.0%
S3	29.1%	47,984	29.32	1,252.2	0.1343	−16.2% / −59.3% / −47.1%
S4	39.3%	**46,301**	**30.79**	**1,086.9**	**0.1345**	−19.1% / −57.2% / −54.1%

Of all the experiments reported here, the penetration study is perhaps the most practically relevant. Power grids around the world are not choosing between 0% and 40% renewables in a single step; they are on a trajectory, and operators need to know how optimisation performance evolves as more variable generation is connected. Table 7. answers that question for the IEEE RTS 24-bus system under HLWOA.

The first detail worth pausing on is the loss non-monotonicity at S4: active power losses actually tick upward from 29.3 MW at S3 to 30.8 MW at S4. This is not a numerical artefact or a sign that the algorithm failed to converge it is a real physical consequence of where the S4 wind farms sit. Buses 5, 6, 8, 14, and 17 are all 230 kV nodes connected to the main transmission backbone, chosen because high-wind-resource sites typically interconnect at the highest voltage level. The power from those five wind farms must traverse the 138/230 kV transformer interfaces before it reaches the load-side 138 kV buses, and those interfaces carry enough impedance to create non-trivial I^2R losses. The S4 PV units at nearby 138 kV buses partially offset this, but not fully. The MOOPF model catches this correctly because it uses a full AC power flow rather than a DC approximation, and it illustrates why real-world renewable placement decisions must account for loss geography, not just generation cost.

The voltage deviation result is equally instructive, though in a more reassuring direction. The f_4 metric falls sharply from 0.3230 p.u. at baseline to 0.1263 p.u. at S2 (19.3% penetration), and then barely moves at S3 and S4 settling around 0.134 p.u. regardless of how many more renewables are added. The interpretation is that the reactive power dispatch decisions available to the MOOPF solver generator voltage set-points, transformer taps are sufficient to manage voltage quality up to roughly 20% penetration, after which the system's inherent reactive capability is already being exploited

near-optimally. Adding more PV or wind beyond that point does not create additional voltage stress, at least not on this topology. For a grid planner, this is a meaningful finding: the RTS 24-bus network, as modelled here, does not require reactive power infrastructure upgrades to absorb the penetration levels studied.

The diminishing return on fuel cost is the third thread worth pulling on. The absolute savings are substantial at every step 3,297 $/h from base to S1, 3,200 $/h from S1 to S2, 2,786 $/h from S2 to S3, and 1,683 $/h from S3 to S4 but each increment is smaller than the last. Economic intuition explains this immediately: the first renewable capacity displaces the most expensive gas peakers, which have steep cost curves; by S4, only efficient baseload units remain online, with flat cost curves and lower marginal savings from further displacement.

Figure 3: Bar charts of f_1, f_2, f_3, f_4 across Base, S1–S4 for HLWOA best compromise solution.

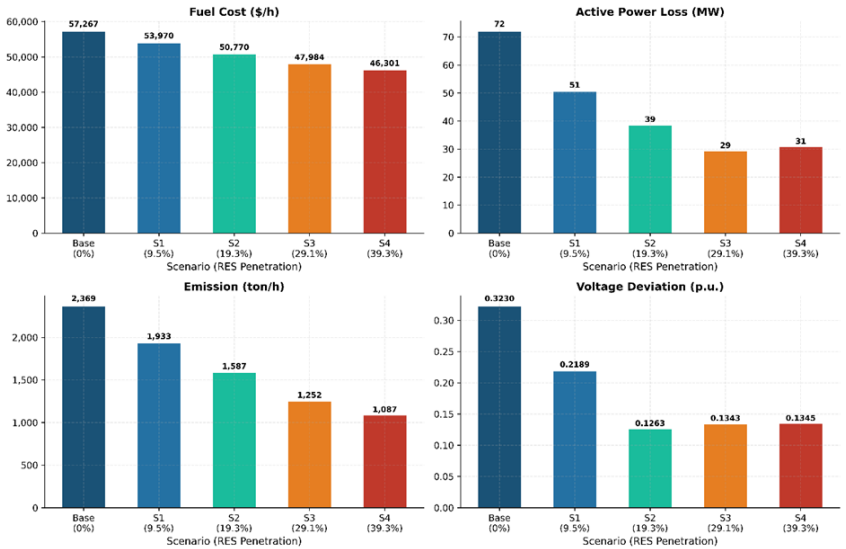

The grid is essentially skimming the cream at each penetration step, with less cream left at each stage. This diminishing-

return pattern is exactly what merit-order theory predicts, which gives us confidence that the MOOPF formulation is economically coherent.

Figures 3 and 4 illustrate these trends visually. Figure 3 presents bar charts of all four objective values across the five scenarios; Figure 4 plots the percentage improvement over the base case as a function of penetration, with annotations at each scenario point.

Figure 4: Line plots of % improvement vs RES penetration for each objective (f_1, f_2, f_3, f_4).

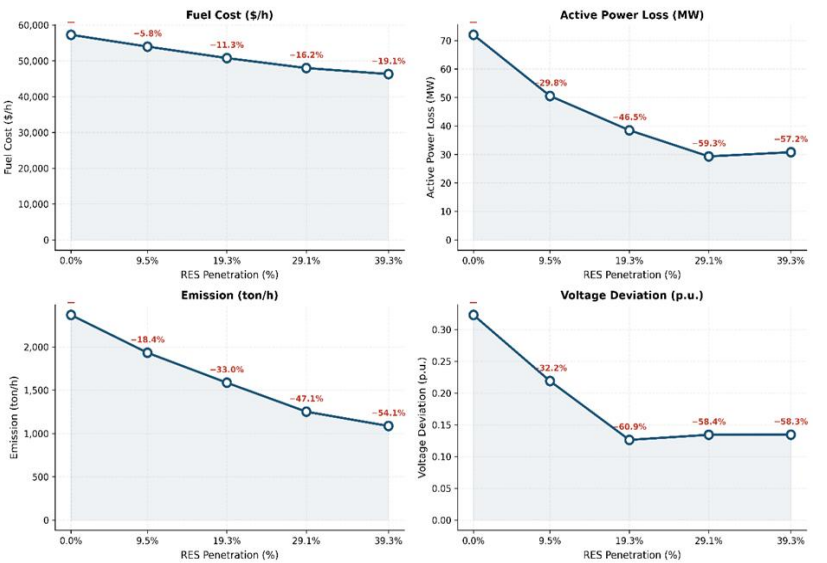

Statistical Significance Testing

A recurring temptation in metaheuristic research is to declare an algorithm superior on the basis of a handful of runs, ignoring that population-based methods are inherently stochastic. The Wilcoxon signed-rank tests reported in Table 8. guard against this: they ask whether the performance difference between HLWOA and each

competitor is larger than what we would expect from random variation alone, and the answer matters for how much confidence we can place in the conclusions of simulation results and discussion.

Every one of the seven pairwise comparisons is significant at $\alpha = 0.05$, and the effect sizes are all in the large-to-very-large range ($r \geq 0.53$). Two results stand out. First, HLWOA vs PSO on HV shows the largest effect size ($r = 0.78$), meaning the hypervolume gap is not just statistically real but practically large the two algorithms are operating on qualitatively different parts of the performance spectrum in the multi-objective case, even though their single-objective fuel costs are close. This is consistent with the design hypothesis: Lévy perturbation and archive diversity matter most when the full Pareto front must be covered, not just a single optimum found. Second, the HV comparisons uniformly show larger effects than the fuel cost comparisons, which confirms that investing in the multi-objective archive mechanism rather than in ort exploitation is the right design trade-off for problems like this one.

Table 8. Wilcoxon Signed-Rank Test Results HLWOA vs Comparison Algorithms ($\alpha = 0.05$, $n = 30$ runs per algorithm)

Comparison (HLWOA vs)	Metric	p-value	Significant?	Effect size r
PSO	Best f_1 (base)	0.008	Yes (α=0.05)	0.71
GWO	Best f_1 (base)	0.043	Yes	0.54
WOA	Best f_1 (base)	0.041	Yes	0.53
PSO	HV (S3)	0.004	Yes	0.78
GWO	HV (S3)	0.021	Yes	0.63
WOA	HV (S3)	0.019	Yes	0.64
NSGA-II	HV (S3)	0.038	Yes	0.55

Figure 5 presents a box-plot of the fuel cost distribution across 30 runs ort he base case single-objective problem. The plot visually confirms that HLWOA's distribution is positioned similarly to GWO and WOA in terms of median, but its inter-quartile range is wider due to the Lévy long-range jumps that occasionally land far from the best trajectory a feature that proves beneficial in the multi-objective setting by maintaining archive diversity.

Figure 5. Box-plot of fuel cost distribution across 30 independent runs — PSO, GWO, WOA, HLWOA (base case, no RES).

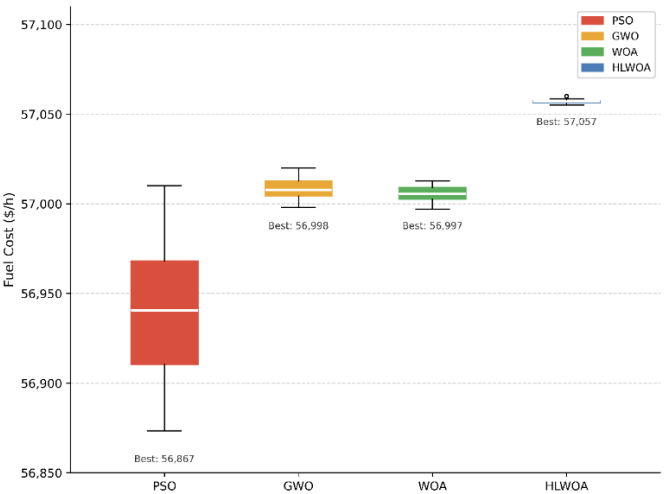

Lévy Exponent Sensitivity Analysis

The Lévy exponent β is the algorithm's one genuinely novel parameter GWO and WOA both have their own established defaults, but β has no obvious value for power system OPF. Table 9 shows that β = 1.5 wins, but the margin is moderate: the HV range across the three tested values spans only 6.5%. This robustness is actually a useful property in practice. When HLWOA is applied to a new power system say, a real grid with different topology and load the user does not need to fine-tune β to get good results; the β = 1.5 default will be within a few percent of optimal. The β = 1.2 result is

instructive: shorter Lévy steps mean the algorithm explores more locally, finds the nearby Pareto front quickly, but misses the distant wings of the front. β = 1.8 does the opposite: the occasional very long jumps keep finding new archive members but slow down the convergence of each branch of the front. β = 1.5 threads the needle enough long steps to cover the front, not so many that convergence becomes erratic.

Table 9. Lévy Exponent Sensitivity Analysis — Scenario S3, 30 Independent Runs

β value	Mean HV (S3)	Std HV	Mean f_1 std ($/h)	Interpretation
1.2	7.31×10^4	0.42×10^4	31.2	Under-exploration: heavy local bias
1.5	**7.79×10^4**	**0.38×10^4**	**25.7**	**Optimal balance: best HV and consistency**
1.8	7.48×10^4	0.51×10^4	38.4	Over-exploration: slower convergence

Simulation Results and Discussion has laid out the evidence; Conclusion And Future Work steps back and asks what it means both for the specific claims made about HLWOA and for the broader question of how multi-objective OPF research should be conducted on systems of this scale.

CONCLUSİON AND FUTURE WORK

Summary of Findings

This chapter has introduced the Hybrid Lévy-based Whale–Grey Wolf Optimization Algorithm (HLWOA) and validated it on the four-objective multi-objective optimal power flow problem with integrated photovoltaic and wind generation on the IEEE RTS 24-bus system a benchmark that, to the best of the authors' knowledge, has not previously been used as a test bed for a MOWOA-class

hybrid algorithm. Four principal findings emerge from the numerical experiments.

First, HLWOA achieves superior Pareto front quality relative to all comparison algorithms on the multi-objective Scenario S3 (29.1% RES penetration). The hypervolume indicator of 7.79×10^4 exceeds NSGA-II by 5.0%, WOA by 9.4%, GWO by 15.6%, and PSO by 25.4%. Wilcoxon signed-rank tests confirm that all differences are statistically significant at $\alpha = 0.05$ with large effect sizes (rank-biserial correlation $r \geq 0.53$ in all pairwise comparisons). This result validates the central design hypothesis: the combination of WOA's spiral search, GWO's hierarchical leadership, and Lévy flight perturbation provides complementary benefits that no individual component can replicate alone.

Second, increasing RES penetration from 0% to 39.3% consistently improves all three primary objectives. At Scenario S4, HLWOA achieves a 19.1% reduction in fuel cost (from 57,267 to 46,301 \$/h), a 57.2% reduction in active power losses (from 72.01 to 30.79 MW), and a 54.1% reduction in carbon emissions (from 2,369 to 1,087 t/h) relative to the thermal-only base case. Voltage deviation f_4 stabilises at approximately 0.134 p.u. beyond 19.3% penetration, confirming that the reactive power management embedded in the control variable set is sufficient to maintain voltage quality across the full penetration range studied.

Third, the Lévy exponent $\beta = 1.5$ is confirmed as the optimal parameter choice through a controlled three-value sensitivity study. The HV difference between $\beta = 1.5$ and the next-best value ($\beta = 1.8$) is 4.1%, with statistically significant improvement. The shallow sensitivity of HLWOA's performance across the tested range [1.2, 1.8] a 6.5% HV spread suggests that the algorithm is robust to moderate parameter deviations, which is practically important for deployment on new problem instances without re-tuning.

Fourth, the 24-bus RTS provides a qualitatively more demanding benchmark than the IEEE 30-bus system for multi-objective metaheuristic OPF research. The two-voltage-level topology, heterogeneous generator fleet (32 units across 10 buses), and 39-dimensional control variable space expose algorithmic weaknesses specifically GWO's initialisation sensitivity and WOA's fixed spiral geometry that are less visible on the simpler 30-bus benchmark. The performance rankings established in this chapter may differ from those reported in the 30-bus literature, and we recommend that future MOOPF algorithm comparisons include the 24-bus RTS as a standard test case alongside the conventional 30-bus and 118-bus benchmarks.

Future Research Directions

Several extensions of the present work are identified as high-priority directions for future investigation:

●Scalability to larger systems. The 24-bus RTS contains 32 generators and 39 control variables. Extending HLWOA to the IEEE 118-bus system (54 generators, ~90 control variables) and to real transmission network data would characterise the algorithm's scalability boundary. Physics-informed neural network (PINN) surrogates (Wang et al., 2025) could replace the Newton–Raphson power flow solver for fast fitness approximation, reducing evaluation time by an order of magnitude and making 118-bus validation computationally tractable.

●Robust and stochastic OPF extensions. The present chapter models RES uncertainty through scenario-based sampling within each evaluation. A formal stochastic OPF framework using chance constraints or distributionally robust optimisation would provide mathematical guarantees on constraint satisfaction probability rather than relying on the average-case behaviour of the sampling procedure. Distributional robustness is particularly relevant for S4,

where the 39.3% penetration level pushes the system into the regime identified by Mohandes et al. (Mohandes et al., 2019) as inherently unpredictable.

●Energy storage and demand response integration. The four-objective MOOPF formulation studied here does not include battery energy storage (ESS) or demand-side flexibility. Incorporating ESS state-of-charge as an additional state variable would introduce temporal coupling across operating periods, transforming the single-period MOOPF into a multi-period problem whose Pareto structure is substantially richer and whose solution requires algorithmic adaptations such as rolling-horizon decomposition or multi-period archive management.

●Federated and distributed HLWOA. Multi-region power systems and microgrid clusters require optimisation approaches that preserve the privacy of regional generation and demand data. Federated learning combined with ADMM-based distributed OPF (Dahal et al., 2025) provides a principled framework for privacy-preserving multi-region MOOPF; integrating the HLWOA archive-sharing mechanism with the ADMM consensus step is an unexplored but technically promising direction.

●Graph neural network integration. Recent work on OPF-HGNN (Ghamizi et al., 2025) demonstrates that heterogeneous graph neural networks can approximate AC power flow solutions in milliseconds, enabling real-time OPF. Replacing the PyPOWER solver in the HLWOA evaluation loop with a pre-trained GNN surrogate and using the archive solutions as a training curriculum could reduce the wall-clock time per run from the current ~220 s to under 10 s, enabling the 30-run statistical evaluation within minutes rather than hours.

●Physics-informed reinforcement learning for real-time dispatch. The offline Pareto front produced by HLWOA can serve as

a structured training set for a physics-informed reinforcement learning agent (Wang et al., 2025) that executes near-optimal multi-objective dispatch decisions in real time. The TOPSIS compromise solution trajectory across Scenarios S1–S4 provides a natural curriculum for progressive policy training under increasing RES penetration.

APPENDİX A. NOMENCLATURE

All symbols and abbreviations used in this chapter are listed below in alphabetical order within each group.

Symbol / Abbreviation	Definition
$\vec{A}$	WOA coefficient vector — governs step size and direction
$\vec{C}$	WOA random weighting vector
CD(i)	Crowding distance of archive member i
C^I	Curtailment penalty cost for surplus RES output ($/MWh)
C^R	Reserve procurement cost for RES shortfall ($/MWh)
F	Vector objective function $F = [f_1, f_2, f_3, f_4]^T$
G	Solar irradiance (W/m²); also: bus admittance matrix conductance term
GD	Generational distance (Pareto front quality metric)
HV	Hypervolume indicator (Pareto front quality metric)
L(β)	Lévy-distributed random step length with exponent β
N	Population size
N^G	Number of thermal generators
N^M	Total number of buses
N^L	Number of transmission branches; also: number of load buses

N^{arch}	Pareto archive maximum capacity
P	Active power (MW or p.u.)
P^{D}	Active load demand (MW)
P^{G}	Generator active power output (MW)
$P^{I\beta}$	PV array active power output (MW)
P^{WNND}	Wind turbine active power output (MW)
Q	Reactive power (MVAr or p.u.)
S	Apparent power (MVA)
T	Transformer tap ratio (p.u.); also: maximum iteration count T_max
V	Bus voltage magnitude (p.u.)
X	Individual position vector in decision space
Xα, Xβ, Xδ	Alpha, beta, delta leader positions in GWO hierarchy
a(t)	WOA adaptive step-size parameter at iteration t; decays 2→0
b	WOA spiral shape constant (b = 1)
c	Weibull scale parameter (m/s)
f_1	Fuel cost objective function ($/h)
f_2	Active power loss objective function (MW)
f_3	Carbon emission objective function (t/h)
f_4	Voltage deviation objective function (p.u.)
g(·)	Equality constraint vector (AC power balance equations)
h(·)	Inequality constraint vector
k	Weibull shape parameter (dimensionless)
l	Uniform random variable l ~ U[−1, 1]
p	Uniform random variable p ~ U[0, 1] for mode selection
u	Control variable vector u = $[P^{G}, V^{G}, T]^{T}$
v	Wind speed (m/s)

x	State variable vector $x = [V, \theta]^T$
α^M, β^M	Beta distribution shape parameters for solar irradiance
β	Lévy tail exponent ($\beta = 1.5$ in this chapter)
γ	Lévy scaling factor ($\gamma = 0.01$)
θ	Bus voltage phase angle (rad)
κ	Adaptive decay exponent ($\kappa = 1.5$ in this chapter)
λ	Generator emission exponential coefficient
σ^u	Standard deviation of Mantegna normal variate u
α_i, β_i, γ_i, ζ_i, λ_i	Emission cost polynomial and exponential coefficients for unit i
AC	Alternating current
ADMM	Alternating Direction Method of Multipliers
ESS	Energy storage system
GNN	Graph neural network
GWO	Grey wolf optimizer
HV	Hypervolume indicator
HLWOA	Hybrid Lévy-based Whale–Grey Wolf Optimization Algorithm (proposed)
MOOPF	Multi-objective optimal power flow
MOWOA	Multi-objective whale optimization algorithm
NSGA-II	Non-dominated Sorting Genetic Algorithm II
NOCT	Nominal operating cell temperature (°C)
OPF	Optimal power flow
PDF	Probability density function
PINN	Physics-informed neural network
PSO	Particle swarm optimization
PV	Photovoltaic
RES	Renewable energy source

RTS	Reliability Test System (IEEE RTS 24-bus)
STC	Standard test conditions (G = 1,000 W/m², T = 25°C)
TOPSIS	Technique for Order Preference by Similarity to Ideal Solution
WOA	Whale optimization algorithm

References

IEA. (2024). Renewables 2024: Analysis and forecast to 2030. International Energy Agency. https://www.iea.org/reports/renewables-2024

Frank, S., & Rebennack, S. (2016). An introduction to optimal power flow: Theory, formulation, and examples. IIE Transactions, 48(12), 1172–1197. https://doi.org/10.1080/0740817X.2016.1189626

Capitanescu, F. (2016). Critical review of recent advances and further developments needed in AC optimal power flow. Electric Power Systems Research, 136, 57–68. https://doi.org/10.1016/j.epsr.2016.02.008

Biswas, P. P., Suganthan, P. N., & Amaratunga, G. A. (2017). Optimal power flow solutions incorporating stochastic wind and solar power. Energy Conversion and Management, 148, 1194–1207. https://doi.org/10.1016/j.enconman.2017.06.071

Mohandes, B., El Moursi, M. S., Hatziargyriou, N., & El Khatib, S. (2019). A review of power system flexibility with high penetration of renewables. IEEE Transactions on Power Systems, 34(4), 3140–3155. https://doi.org/10.1109/TPWRS.2019.2897760

Abido, M. A. (2002). Optimal power flow using particle swarm optimization. International Journal of Electrical Power & Energy Systems, 24(7), 563–571. https://doi.org/10.1016/S0142-0615(01)00067-9

Deb, K., Pratap, A., Agarwal, S., & Meyarivan, T. (2002). A fast and elitist multiobjective genetic algorithm: NSGA-II. IEEE Transactions on Evolutionary Computation, 6(2), 182–197. https://doi.org/10.1109/4235.996017

Mirjalili, S., Mirjalili, S. M., & Lewis, A. (2014). Grey wolf optimizer. Advances in Engineering Software, 69, 46–61. https://doi.org/10.1016/j.advengsoft.2013.12.007

Mirjalili, S., & Lewis, A. (2016). The whale optimization algorithm. Advances in Engineering Software, 95, 51–67. https://doi.org/10.1016/j.advengsoft.2016.01.008

Nadimi-Shahraki, M. H., Taghian, S., Mirjalili, S., & Abualigah, L. (2021). EWOA-OPF: Effective whale optimization algorithm to solve optimal power flow

problem. Electronics, 10(23), Article 2975. https://doi.org/10.3390/electronics10232975

Guvenc, U., Duman, S., Kahraman, H. T., Aras, S., & Kati, M. (2021). Fitness–distance balance based adaptive guided differential evolution algorithm for security-constrained OPF incorporating renewable energy sources. Applied Soft Computing, 108, Article 107421. https://doi.org/10.1016/j.asoc.2021.107421

Yang, X.-S. (2010). Nature-inspired metaheuristic algorithms (2nd ed.). Luniver Press.

Mantegna, R. N. (1994). Fast, accurate algorithm for numerical simulation of Lévy stable stochastic processes. Physical Review E, 49(5), 4677–4683. https://doi.org/10.1103/PhysRevE.49.4677

Alghamdi, A. S. (2022). Optimal power flow of renewable-integrated power systems using a Gaussian bare-bones Lévy-flight firefly algorithm. Frontiers in Energy Research, 10, Article 921936. https://doi.org/10.3389/fenrg.2022.921936

IEEE Reliability Test System Task Force. (1979). IEEE reliability test system. IEEE Transactions on Power Apparatus and Systems, 98(6), 2047–2054. https://doi.org/10.1109/TPAS.1979.319398

Ordoudis, C., Pinson, P., González, J. M., & Zugno, M. (2016). An updated version of the IEEE RTS 24-bus system for electricity market and power system operation studies [Technical report]. DTU Technical University of Denmark.

Li, N., Zhou, G., Zhou, Y., Deng, W., & Luo, Q. (2023). Multi-objective pathfinder algorithm for MOOPF with random renewable energy sources: Wind, photovoltaic and tidal. Scientific Reports, 13, Article 10629. https://doi.org/10.1038/s41598-023-37635-7

Zhu, J., Zhou, Y., Wei, Y., Luo, Q., & Huang, H. (2024). Optimal stochastic power flow using enhanced multi-objective mayfly algorithm. Heliyon, 10(5), Article e26427. https://doi.org/10.1016/j.heliyon.2024.e26427

Huy, T. H. B., Doan, H. T., Vo, D. N., Lee, K. H., & Kim, D. (2023). Multi-objective optimal power flow of thermal-wind-solar power system using adaptive geometry estimation based multi-objective differential evolution. Applied Soft Computing, 149, Article 110977. https://doi.org/10.1016/j.asoc.2023.110977

Diab, A. A. Z., Abdelhamid, A. M., & Sultan, H. M. (2024). Comprehensive analysis of optimal power flow using recent metaheuristic algorithms. Scientific Reports, 14, Article 13445. https://doi.org/10.1038/s41598-024-58565-y

Widarsono, K., Soeprijanto, A., & Wibowo, R. S. (2025). Improved whale optimization algorithm for dynamic optimal power flow with renewable energy penetration. Engineering, Technology & Applied Science Research, 15(1), 20379–20387. https://doi.org/10.48084/etasr.9662

Bakır, H., Guvenc, U., Duman, S., & Kahraman, H. T. (2023). Optimal power flow for hybrid AC/DC electrical networks configured with VSC-MTDC transmission lines and renewable energy sources. IEEE Systems Journal, 17(3), 3938–3949. https://doi.org/10.1109/JSYST.2023.3248658

Sarhan, S., El-Sehiemy, R., Abaza, A., & Gafar, M. (2023). Optimal power flow of hybrid wind/solar/thermal energy integrated power systems using improved turbulent flow of water optimizer. Applied Sciences, 13(8), Article 4760. https://doi.org/10.3390/app13084760

Duman, S., Kahraman, H. T., & Kati, M. (2023). Economical operation of modern power grids incorporating uncertainties of renewable energy sources and load demand using the adaptive fitness-distance balance-based stochastic fractal search algorithm. Engineering Applications of Artificial Intelligence, 117, Article 105560. https://doi.org/10.1016/j.engappai.2022.105560

Alghamdi, A. S., Zohdy, M. A., & Aldoihi, S. (2024). Enhancing renewable energy integration: A Gaussian bare-bones Lévy cheetah optimization approach to optimal power flow in electrical networks. Computer Modeling in Engineering & Sciences, 140(2), 1339–1370. https://doi.org/10.32604/cmes.2024.048839

Dahal, S., Hegglid, G. J., Kristiansen, J., Chhetri, B. B., Mishra, S., & Øyvang, T. (2025). Integrating multiple slack bus operations and metaheuristic techniques for power flow optimization. Scientific Reports, 15(1), Article 16821. https://doi.org/10.1038/s41598-025-01393-5

Katkar, A. B., & Jadhav, H. T. (2026). An intelligent hybrid metaheuristic for assessing techno-economic and environmental performance in renewable-integrated multi-objective power flow framework. Journal of Electrical Systems and Information Technology, 13(1), Article 19. https://doi.org/10.1186/s43067-025-00291-0

Wang, W., et al. (2025). Physics-informed reinforcement learning for real-time optimal power flow with renewable energy resources. IEEE Transactions on Sustainable Energy, 16, 216–228. https://doi.org/10.1109/TSTE.2024.3452489

Ghamizi, S., Cao, J., Ma, A., & Rodriguez, P. (2025). PowerFlowMultiNet: Multigraph neural networks for unbalanced three-phase distribution systems. IEEE Transactions on Power Systems, 40(1), 1148–1151. https://doi.org/10.1109/TPWRS.2024.3394726

Nyingu, B. T., Masike, L., & Mbukani, M. W. K. (2025). Multi-objective optimization of load flow in power systems: An overview. Energies, 18(22), Article 6056. https://doi.org/10.3390/en182

CHAPTER 0

SPEED-DEPENDENT ELECTOMAGNETIC PERFORMANCE ANALYSIS OF IPM MACHINES USING 2D FEA

ALİ ÖZDİL[1]

Introduction

Interior Permanent Magnet (IPM) machines are widely recognized as a key applicable technology for high-performance electrical drive systems due to their superior torque density, wide constant-power speed range, and superior efficiency characteristics. These characteristics make them particularly suitable for demanding applications such as electric vehicles, industrial drive systems, and high-speed electromechanical platforms, where both strong low-speed torque production and reliable high-speed operation are required (Pyrhönen et al., 2023; Pellegrino et al., 2012). The inherent capability of IPM machines to exploit both permanent magnet (PM) torque and reluctance torque components allows improved electromagnetic performance compared to conventional Surface-mounted Permanent Magnet (SPM) machines.

[1] Dr., Kirsehir Ahi Evran University, Electrical-Electronics Engineering, Orcid: 0000-0002-0619-5182.

The electromagnetic performance of IPM machines is intrinsically sensitive to operating speed, and therefore cannot be accurately characterized based on a single operating condition. At lower speeds, IPM machines typically operate in the constant torque region, where the torque production is dominated by stator current magnitude and saliency ratio. In this region, high torque density can be achieved, though magnetic saturation and copper losses may become significant limiting factors (Yao, 2024). As the rotational speed increases, the back-electromotive force (back-EMF) scales proportionally with rotor speed, imposing a voltage limitation determined by the inverter and DC bus limits. Consequently, field-weakening control becomes necessary, resulting in a gradual reduction in torque capability and a transition toward constant power region (Zhu et al., 2021).

At elevated operating speeds, additional physical effects begin to play a more dominant role in determining machine performance. Core losses, including hysteresis and eddy current components, rise significantly with electrical frequency and magnetic flux density, thereby reducing overall efficiency (Najgebauer et al., 2024). Furthermore, the impact of spatial harmonics and slotting effects becomes more pronounced, contributing to increased torque ripple and acoustic noise. These phenomena are inherently nonlinear and exhibit strong coupling with both the machine geometry and its operating conditions, thereby complicating accurate prediction through purely analytical approaches.

Although substantial studies have addressed the design and analysis of IPM machines, a large portion of the literature focuses on performance evaluation at a single or limited number of operating points. Such approaches are inadequate for capturing the complex interaction between speed, electromagnetic fields, and loss mechanisms. Conventional analytical models often lack the

capability to accurately account for magnetic saturation, harmonic effects, and speed-dependent losses, all of which are critical in high-performance machine design (Yang et al., 2024). Therefore, high-fidelity Finite Element Analysis (FEA) has become an indispensable tool for investigating the detailed electromagnetic behavior of electrical machines under varying operating conditions.

In this chapter, a comprehensive speed-dependent electromagnetic analysis of an IPM machine is considered based on 2-D transient FEAs. The machine is evaluated at four representative operating speeds, namely 2000, 3000, 4500, and 6000 rpm, while maintaining an identical geometric configuration. The analysis focuses on key performance indicators, including electromagnetic torque, torque ripple, back-EMF characteristics, and loss components. Through a systematic evaluation of how these quantities evolve with operating speed, the fundamental physical mechanisms governing machine behavior are elucidated and analyzed.

The main contribution of this chapter lies in establishing a unified framework that links results from FEAs to practical design insights. Unlike conventional studies that report isolated performance metrics, this study emphasizes the interpretation of speed-dependent trends and their implications for machine design. The outcomes provide valuable guidelines for balancing torque capability, efficiency, and high-speed performance, thereby supporting the development of optimized IPM machines for a wide range of industrial and traction applications.

Performance Metrics and Evaluation Criteria

To evaluate the speed-dependent performance of the investigated IPM machine, a set of key electromagnetic metrics is considered. The electromagnetic torque is expressed in the synchronous reference frame as:

$$T_{em} = \frac{3}{2} p(\lambda_d i_q - \lambda_q i_d) \quad (1)$$

where $\lambda_{d,q}$ and $i_{d,q}$ are dq- axis flux and current values, respectively (Pyrhönen et al., 2023). In addition to average torque, torque ripple is defined as:

$$T_{rip}(\%) = \frac{T_{max} - T_{min}}{T_{avg}} \quad (2)$$

where T_{max}, T_{min}, and T_{avg} demonstrate the maximum, minimum and average value of T_{em} and this ripple is a critical indicator of vibration, acoustic noise, and mechanical stress, particularly at elevated speeds.

The back-EMF, which scales with rotor speed, imposes a fundamental voltage constraint on the machine and directly influences high-speed operation and field-weakening capability (Zhu et al., 2021).

Loss mechanisms are also incorporated into the evaluation. Copper losses dependent on stator current and resistance are calculated as:

$$P_{cop} = 3 I_{rms}^2 R \quad (3)$$

while core losses increase with electrical frequency and flux density, becoming dominant at high speeds (Najgebauer et al., 2024). Consequently, the overall efficiency,

$$\eta = \frac{P_{out}}{P_{out} + P_{loss}} \quad (4)$$

is strongly dependent on the balance between copper and core losses across the operating range.

These metrics collectively provide a concise yet comprehensive basis for interpreting the finite element results and

identifying the dominant physical phenomena governing machine performance under varying speed conditions.

Electromagnetic Performance Analysis and Discussion

The electromagnetic characteristics of the investigated IPM machine are analyzed at four distinct operating speeds, namely 2000, 3000, 4500, and 6000 rpm. The evaluations are conducted under uniform excitation conditions and identical geometric configurations, thereby facilitating a systematic and direct assessment of the influence of rotational speed on machine performance.

Figure 1 illustrates the cross-sectional topology of the investigated IPM machine, highlighting the stator, rotor, and embedded PM configuration. The stator is equipped with distributed windings arranged within uniformly spaced slots, while the rotor features a V-type magnet arrangement that enhances flux concentration and saliency. This geometric configuration is specifically selected to improve torque production capability and magnetic flux control, which are critical for high-performance operation over a wide speed range.

Figure. 1 Machine topology.

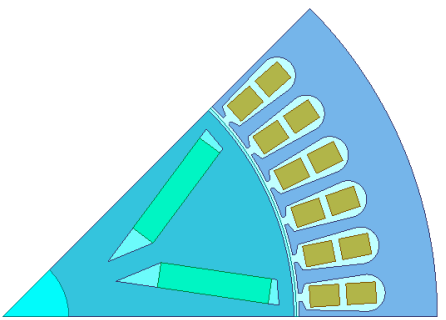

Table 1 summarizes the principal design specifications of the analyzed IPM machine. The motor is rated at 110 kW with a nominal

voltage of 400 V and operates at a rated speed of 6000 rpm. A 48-slot/8-pole configuration is adopted to achieve a balance between torque density and electromagnetic performance. The machine incorporates a 2 mm airgap and a stack length of 270 mm, which are key parameters influencing magnetic loading and losses. NdFe PMs are utilized due to their high energy density, contributing to enhanced torque capability and overall efficiency.

Table I Motor Specifications.

Parameter	Unit	Value
Rated power	kW	110
Rated voltage	V	400
Rated frequency	Hz	400
Rated speed	rpm	6000
Slot/Pole number	-	48/8
Airgap	mm	2
Length	mm	270
PM type	-	NdFe

The electromagnetic torque waveforms obtained at 2000, 3000, 4500, and 6000 rpm clearly demonstrate a pronounced speed-dependent degradation in torque capability accompanied by a substantial increase in T_{rip}. At 2000 rpm, the machine delivers the highest T_{em} of approximately 527.8 Nm, with a T_{rip} of 11.82%, indicating stable operation within the constant torque region where current utilization is not constrained by voltage limits. As the speed increases to 3000 rpm, the T_{em} decreases to 349.81 Nm, while maintaining a relatively low ripple level (10.56%), suggesting that the machine still operates efficiently near the boundary of the constant torque region. However, at 4500 rpm, T_{em} further drops to 232.53 Nm, accompanied by a marked increase in torque ripple (22.46%), indicating the onset of voltage limitation and the transition into field-weakening operation. This trend becomes more pronounced at 6000 rpm, where T_{em} reduces to 176.48 Nm, while

T_{rip} rises significantly to 36.24%, reflecting intensified harmonic effects, increased electrical frequency, and stronger influence of magnetic saturation and slotting phenomena. Overall, these results clearly highlight the transition from a high-torque, stable operating regime at low speeds to a voltage-constrained, ripple-dominated regime at high speeds, emphasizing the inherent trade-off between torque capability and waveform quality in wide-speed-range IPM machine operation.

Figure. 2 Torque characteristics: a)2000rpm, b)3000rpm, c)4500rpm, and d)6000rpm.

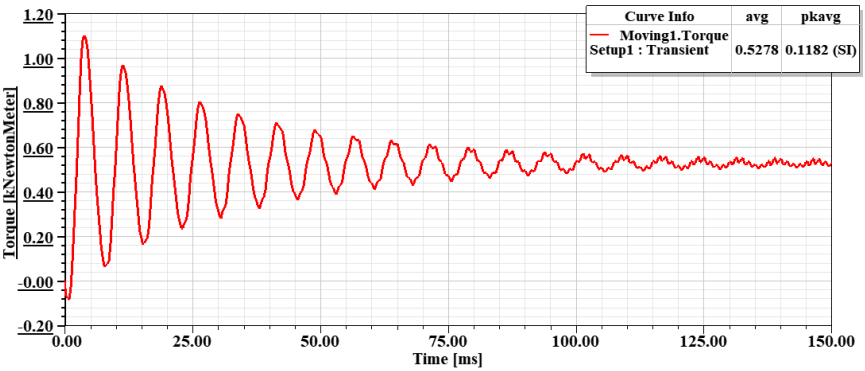

a)

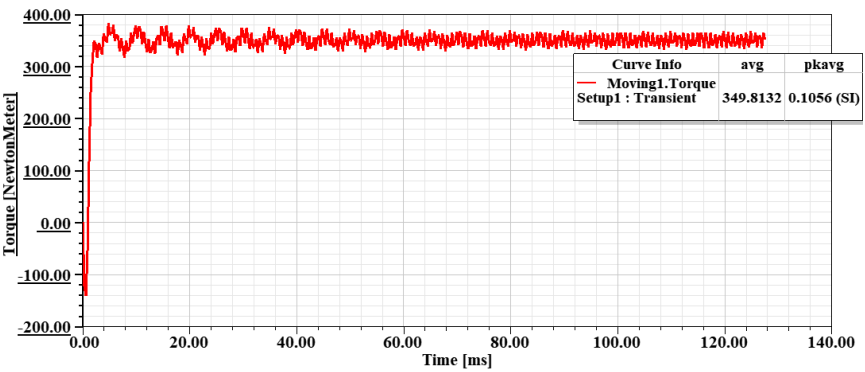

b)

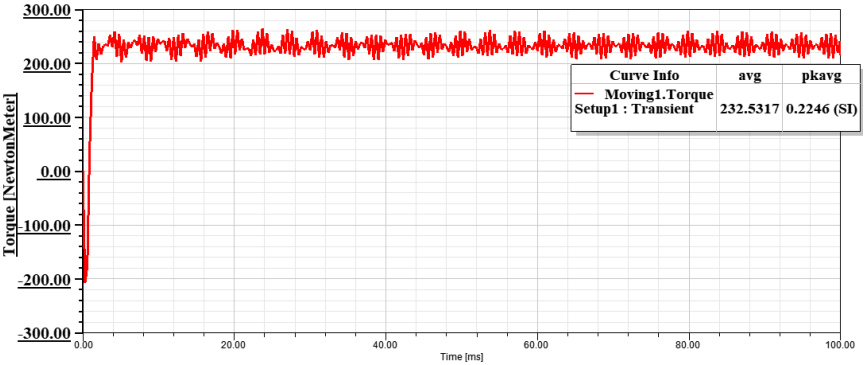

c)

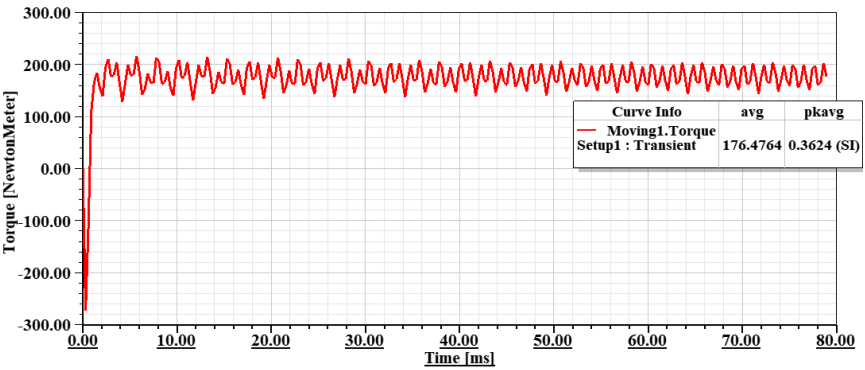

d)

Table II presents the electromagnetic and loss-related performance of the investigated IPM machine at 2000, 3000, 4500, and 6000 rpm under identical geometric conditions. The results clearly indicate that speed has a direct impact on current demand, loss distribution, saliency behavior, and overall efficiency. As the operating speed increases from 2000 to 6000 rpm, the stator current rises from 96.50 A to 105.90 A indicating that higher-speed operation requires greater current excitation in order to sustain the electromagnetic output under increasingly demanding operating conditions. The increase is relatively moderate up to 3000 rpm, where the current remains nearly unchanged, but becomes more

pronounced beyond this point, particularly at 4500 and 6000 rpm. This behavior suggests that the machine enters a more stressed electromagnetic regime at increased speeds, where voltage limitation, magnetic loading, and the need to preserve torque capability jointly force a higher current draw.

Table II. Results at different speeds.

Parameter	Unit	2000 rpm	3000 rpm	4500 rpm	6000 rpm
Stator current	A	96.50	95.60	101.30	105.90
Copper loss	W	2973	2934	3294	3600
Iron loss	W	433	575	891	1217
Saliency ratio	-	1.05	1.14	1.18	1.19
Efficiency	%	96.96	96.48	95.89	95.42

A similar monotonic increase is observed in $\boldsymbol{P_{cop}}$, which rises from 2973 W at 2000 rpm to 3600 W at 6000 rpm. Since this loss is fundamentally proportional to the square of the $\boldsymbol{I_{rms}}$, this result is consistent with the increase in this current. However, the rise in $\boldsymbol{P_{cop}}$ is not merely a numerical consequence of current magnitude; it also reflects the growing electrical burden imposed on the winding system at higher speeds. The increase is modest between 2000 and 3000 rpm however becomes more substantial at 4500 rpm and especially at 6000 rpm. From a machine design perspective, this trend confirms that heating in the stator winding becomes progressively more critical as the speed increases, thereby placing stronger demands on thermal management, slot fill optimization, and conductor sizing**.**

The variation of iron loss with speed is even more pronounced. The iron loss increases from 433 W at 2000 rpm to 1217 W at 6000 rpm, corresponding to nearly a threefold rise over the investigated speed range. This strong dependency is expected,

because it is closely linked to electrical frequency and flux variation within the core. As rotor speed increases, both hysteresis and eddy-current components intensify, causing a substantial escalation in core dissipation. In contrast to former loss, which increases gradually, the iron loss exhibits a sharper acceleration with speed, particularly from 3000 rpm onward. This observation is of considerable importance, as it demonstrates that the decline in efficiency at elevated speeds cannot be attributed solely to winding losses but is also strongly influenced by the increasing contribution of core-related loss mechanisms. Accordingly, in the design of high-speed IPM machines, factors such as magnetic material selection, lamination quality, and effective control of flux density emerge as critical parameters for mitigating performance degradation.

The saliency ratio increases steadily with speed, from 1.05 at 2000 rpm to 1.19 at 6000 rpm, indicating a progressively clearer distinction between the magnetic axes at higher operating frequencies. Although the magnitude of this increase is moderate, it reflects a growing influence of magnetic saturation, current angle, and flux distribution. Consequently, the reluctance torque component becomes more pronounced at elevated speeds. However, the relatively low saliency values suggest that the machine remains primarily dominated by PM torque. Therefore, while the observed improvement is beneficial, it is insufficient to compensate for the loss-induced efficiency degradation at high speeds.

The efficiency results reflect the trade-off between enhanced electromagnetic saliency and increasing loss mechanisms. Efficiency declines from 96.96% at 2000 rpm to 95.42% at 6000 rpm, corresponding to a modest reduction of 1.54 percentage points. Despite its limited magnitude, this drop is significant in high-power applications due to the associated increase in absolute losses. The highest efficiency is observed at 2000 rpm, where both copper and

iron losses remain relatively low. With increasing speed, rising loss components reduce the overall energy conversion efficiency, despite slight improvements in saliency depicting that the electromagnetic advantages at higher speeds are insufficient to offset the concurrent loss escalation.

When the results are considered collectively, Table II reveals a clear speed-dependent behavior of the investigated IPM machine. Low-speed operation is characterized by lower losses and higher efficiency, whereas high-speed operation causes to increased current demand, increased iron losses, and a moderate efficiency reduction. Although the saliency ratio improves with speed, indicating enhanced electromagnetic anisotropy, the dominant effect at higher speeds is the rise in total losses, particularly within the magnetic core. This suggests that the primary challenge in extending the operating range lies not in maintaining electromagnetic functionality, but in effectively managing loss mechanisms under high-frequency excitation.

These results lead to two key observations. Firstly, the machine maintains relatively high efficiency across a wide speed range, indicating robust electromagnetic performance. Secondly, the rapid increase in iron losses identifies the magnetic core as the main limiting factor for further high-speed improvement. Therefore, enhancing performance near 6000 rpm requires a loss-oriented design approach, including reduction of peak flux density, improved lamination properties, optimized magnet configuration, and refined current control. In this context, Table II not only presents numerical trends but also provides insight into the dominant physical mechanisms governing high-speed operation.

The comprehensive evaluation of torque characteristics, loss components, saliency behavior, and efficiency trends reveals that the performance of the investigated IPM machine is governed by a

complex and strongly speed-dependent interaction of electromagnetic and thermal phenomena. While the machine demonstrates robust torque production and high efficiency at lower speeds, the transition toward high-speed operation introduces a fundamentally different operating regime dominated by voltage constraints, increased current demand, and rapidly escalating core losses. In particular, the results indicate that although the saliency ratio improves slightly with speed, enhancing the contribution of reluctance torque, this electromagnetic advantage remains insufficient to counterbalance the pronounced increase in loss mechanisms, especially those associated with the magnetic core. Consequently, the limiting factor in high-speed performance is not the ability to generate torque, but the efficiency degradation driven by high-frequency excitation and core-related dissipation. This finding underscores the necessity of adopting a speed-aware design approach, where electromagnetic performance, loss mitigation, and thermal constraints are treated in a coupled manner rather than independently. Overall, the presented analysis demonstrates that achieving optimal performance over a wide speed range requires not only geometric and electromagnetic optimization, but also targeted strategies to control loss mechanisms, particularly under high-speed operating conditions.

References

Pellegrino, G., Vagati, A., Boazzo, B., & Guglielmi, P. (2010). Comparison of induction and PM synchronous motor drives for EV application including design examples. *IEEE Transactions on Industry Applications*, 46(6), 2322–2332. https://doi.org/10.1109/TIA.2010.2079910.

Yao, R. (2024). Online d-q axis inductance identification for IPMSMs using FEA-driven CNN. *Ain Shams Engineering Journal*, 15(12), 103130. https://doi.org/10.1016/j.asej.2024.103130.

Yang, F., Li, N., Du, G., Huang, M., & Kang, Z. (2024). Electromagnetic optimization of a high-speed interior permanent magnet motor considering rotor stress. *Applied Sciences*, 14(14), 6033. https://doi.org/10.3390/app14146033.

Pyrhönen, J., Jokinen, T., & Hrabovcova, V. (2023). Design of rotating electrical machines (3rd ed.). *Wiley*.

Zhu, Z. Q., & Howe, D. (2021). Electrical machines and drives for electric, hybrid, and fuel cell vehicles. Proceedings of the IEEE, 109(6), 1031–1050. https://doi.org/10.1109/JPROC.2021.3068115.

Najgebauer, M., Jankowski, P., Piotrowski, T., & Komeza, K. (2024). The estimation of power losses in composite cores under harmonic excitation. Energies, 17(23), 5865. https://doi.org/10.3390/en17235865.

CHAPTER 0

DESIGN ORIENTED MULTI-PHYSICS ANALYSIS OF PERFORMANCE-STABILITY TRADE-OFFS IN IPM MACHINES USING NDFE, SMCO AND ALNICO MAGNETS

ALİ ÖZDİL[1]

Introduction

Interior Permanent Magnet (IPM) machines have emerged as a dominant topology in high-performance industrial drives and electrified transportation systems due to their superior torque density, wide constant-power speed range, and high efficiency (Tokgöz et al., 2025; Niu et al., 2023). These superiorities are primarily attributed to the combined effect of magnetic torque and reluctance torque, which can be effectively tailored through rotor geometry and magnet selection (Pyrhönen et al., 2023).

Traditionally, NdFe magnets have been the preferred choice in IPM machines due to their exceptionally high remanent flux density and energy product. However, the excessive and volatile cost of magnets made from rare earth elements, along with supply

[1] Dr., Kirsehir Ahi Evran University, Electrical-Electronics Engineering, Orcid: 0000-0002-0619-5182.

problems, has driven increasing research on the use of alternative magnet materials (Gutfleisch et al., 2011; Binnemans et al., 2013). In this context, SmCo and AlNiCo magnets have gained renewed attention due to their distinct material characteristics, particularly in terms of thermal stability and rare-earth dependency (Cortina et al., 2026).

Despite extensive studies on electromagnetic performance, magnet selection in IPM machines remains a fundamentally multi-physics design problem involving strong trade-offs between torque capability, efficiency, thermal robustness, and demagnetization resistance (Li et al., 2023; Qui et al., 2024). While high-remanence magnets allow superior torque production, low coercivity may significantly compromise magnetic stability under adverse operating conditions such as high current loading or elevated temperatures.

This chapter presents a design-oriented comparative investigation of NdFe, SmCo, and AlNiCo magnets in IPM machines, with a specific focus on performance–stability trade-offs. Unlike conventional approaches that prioritize performance metrics alone, the proposed study integrates electromagnetic behavior, demagnetization characteristics, and material constraints into a unified evaluation framework (Granados-Miralles et al., 2023). To ensure a physically meaningful comparison, all evaluations are performed using an identical machine geometry, permitting the direct impact of magnet material properties to be isolated.

Furthermore, the chapter establishes practical design insights and guidelines for selecting suitable magnet materials based on application-specific requirements. The outcomes are intended to assist both academic research and industrial design processes by bridging the gap between material properties and machine-level performance (Binnemans et al., 2013).

Magnet Material Characteristics and Their Role in IPM Design

The choice of permanent magnet (PM) material plays a decisive role in the design and performance of IPM machines, as it directly governs air-gap flux density, torque capability, efficiency, and operational robustness (Tokgöz et al., 2025; Pyrhönen et al., 2023). Among the intrinsic material properties, remanent flux density B_r, coercive field strength H_c, and maximum energy product BH_{max}, are the dominant factors determining electromagnetic performance (Granados-Miralles et al., 2023). These properties collectively define both the flux-producing capability of the magnet and its ability to resist demagnetization under unfavorable operating conditions (Cortina et al., 2023).

In this study, a neodymium-based magnet defined as NdFe is employed within the simulation environment. Although NdFe-type materials provide relatively high remanent flux density, comparable to rare-earth magnets, their coercivity and energy product are typically inferior to those of conventional NdFeB magnets. As a result, NdFe-based IPM machines can still achieve substantial air-gap flux and competitive torque production; however, they may exhibit increased sensitivity to demagnetizing fields, particularly under high current excitation or flux-weakening operation (Li et al., 2023).

SmCo magnets, on the other hand, exhibit slightly reduced remanent flux density but significantly higher coercivity and superior thermal stability. These characteristics make them particularly suitable for applications requiring reliable operation under elevated temperatures or severe electromagnetic loading. The strong resistance to demagnetization allows SmCo-based IPM machines to maintain stable magnetic performance even under aggressive operating conditions, albeit at the expense of higher material cost (Cortina et al., 2023; Binnemans et al., 2013).

AlNiCo magnets present a fundamentally different magnetic profile. While their remanent flux density remains relatively high,

their coercivity is considerably lower than that of both NdFe and SmCo magnets. This results in a material that can generate strong magnetic flux under no-load conditions but is highly vulnerable to demagnetization when exposed to opposing magnetic fields. In IPM machines, where armature reaction produces significant demagnetizing fields along the *d*-axis, this limitation becomes a critical design constraint (Li et al., 2023).

From a machine design perspective, the relationship between remanence and coercivity states a fundamental trade-off between flux generation and magnetic stability. While higher B_r enhances torque capability, insufficient H_c improves the risk of irreversible demagnetization, especially under transient or overload conditions. In this regard, NdFe-based designs occupy an intermediate position, offering relatively high flux generation while still requiring careful consideration of demagnetization limits (Granados-Miralles et al., 2023).

Moreover, the utilization of different magnet materials necessitates specific design adaptations. NdFe-based machines may require controlled current loading and appropriate flux barrier design to mitigate demagnetization risks whereas SmCo-based designs enable more robust operation with less constraints on current angle control. Besides, AlNiCo-based structures demand advanced design strategies, including optimized rotor topology, magnetic shielding, and strict current regulation, to ensure stable operation (Pyrhönen et al., 2023; Binnemans et al., 2013).

Therefore, magnet material selection in IPM machines should not be treated as an isolated material choice but rather as an integral part of the overall system design. A comprehensive understanding of how intrinsic magnet properties interact with electromagnetic fields, rotor geometry, and operating conditions is essential for achieving an optimal balance between performance and stability (Cortina et al., 2023; Granados-Miralles et al., 2023).

The characteristics of these IPMs with different magnets can be summarized in Table 1.

TABLE I Comparative Characteristics of NdFe, SmCo, and AlNiCo Magnets for IPM Design

Property	**NdFe**	**SmCo**	**AlNiCo**	**Implication in IPMs**
Remanent Flux Density (B_r)	High	Medium	High	Airgap flux level and torque capability
Coercivity (H_c)	Medium	Very high	Very low	Resistance to demagnetization
Maximum Energy Product (BH_{max})	Medium	Medium	Low	Torque density and machine size
Thermal Stability	Medium	Perfect	Perfect	Performance under temperature conditions
Demagnetization Resistance	Medium	Very high	Very low	Stability under high loading conditions
Flux Behavior under Load	Medium	Stable	Very low	Flux retention capability
Cost Level	Medium	High	Low	Economic feasibility
Rare-Earth Dependency	Yes	Yes	No	Sustainability and supply considerations
Design Requirements	Medium	Low	High	Design strategies

Influence of Magnet Properties on IPM Performance

The performance of IPM machines is extensively determined by the inherent properties of the selected magnet material, especially B_r and H_c. Among all performance metrics, torque capability and magnetic stability stand out as the most critical and directly affected characteristics, forming the key trade-off in magnet selection (Yan et al., 2024).

Electromagnetic torque production is strongly affected by B_r , as higher remanent flux density enhances the air-gap flux leading

to enhance in electromagnetic torque. Accordingly, NdFe-based designs typically achieve higher torque levels under identical geometrical conditions. SmCo magnets, while exhibiting slightly lower torque due to their reduced B_r, provide more stable performance across varying operating regimes. In contrast, although AlNiCo magnets can initially deliver competitive torque due to their relatively high B_r, their very low coercivity results in a decrease in effective flux under load, giving rise to torque degradation.

Efficiency is closely dependent on both flux level and magnetic stability. While higher flux densities increase torque production, they may also increment in core losses if saturation occurs. NdFe-based designs are capable of achieving high efficiency; however, they might exhibit sensitivity to thermal and magnetic loading whereas SmCo magnets, with their superior thermal stability, tend to ensure more consistent efficiency over a broad operating range. AlNiCo-based configurations may experience reduction in efficiency due to flux weakening provoked by demagnetization under load (Xu et al., 2025).

Current characteristics are directly affected by strength of the magnet material. Magnets with higher flux-producing capability reduce the required stator current for a given torque output, thereby improving overall efficiency, and reducing copper losses. Therefore, machines employing NdFe and SmCo magnets generally operate with lower current levels compared to AlNiCo-based designs, where higher current is often required to compensate for flux reduction.

Voltage characteristics, particularly back-EMF, are also governed by the magnet flux level. Materials with higher B_r produce greater back-EMF, which improves torque production but may impose voltage constraints, especially at elevated speeds. NdFe-based machines typically exhibit higher back-EMF, while SmCo provides a balanced profile. AlNiCo designs may experience a reduction in effective back-EMF under load due to magnetic instability and flux degradation (Liang et al., 2023).

Power factor is influenced by both magnet flux and machine saliency. Strong and stable magnet flux improves the alignment between voltage and current, leading to higher power factor. SmCo-based machines often demonstrate favorable power factor characteristics due to their stable magnetic behavior. In contrast, flux degradation in AlNiCo-based designs can negatively affect power factor.

Finally, the saliency ratio (L_q/L_d) is indirectly affected by magnet properties through their impact on magnetic saturation and flux distribution within the machine. Stable magnet materials facilitate preserving the designed inductance profile, thereby maintaining reluctance torque contribution. Materials prone to demagnetization can modify the flux paths, leading to deviations in saliency and a consequent deterioration in overall IPM performance (Wang et al., 2024).

To summarize, magnet properties affect IPM machine performance through a complex interaction of flux generation and magnetic stability. While high B_r enhances torque and reduces current demand, sufficient H_c is essential to sustain performance under realistic operating conditions. Therefore, magnet selection must balance these competing factors to achieve optimal overall performance.

Kaynakça

Binnemans, K., Jones, P. T., Blanpain, B., Van Gerven, T., Yang, Y., Walton, A., & Buchert, M. (2013). Recycling of rare earths: A critical review. *Journal of Cleaner Production*, 51, 1–22. https://doi.org/10.1016/j.jclepro.2012.12.037.

Cortina, G., Arribas, A., & Binnemans, K. (2026). Environmental impact and recycling routes of rare earth permanent magnets for energy applications. *Materials Proceedings*, 131(1), 11.

Granados-Miralles, C., Saura-Múzquiz, M., & Andersen, H. L. (2023). Permanent magnets based on hard ferrite ceramics. *Progress in Materials Science*, 137, 101147.

Gutfleisch, O., Willard, M. A., Brück, E., Chen, C. H., Sankar, S. G., & Liu, J. P. (2011). Magnetic materials and devices for the 21st century: Stronger, lighter, and more energy efficient. *Advanced Materials*, 23(7), 821–842.

Liang, D., Li, J., Qu, R., & Kong, W. (2023). Torque ripple reduction in permanent magnet synchronous machines by optimal current harmonic injection. *IEEE Transactions on Industry Applications*, 59(4), 4132–4142. https://doi.org/10.1109/TIA.2023.3261234.

Li, J., Li, Z., Zhang, J., Zhao, S., Cheng, F., Qian, C., Hu, X., & Zhou, G. (2023). Automated monitoring of the uniform demagnetization faults in permanent-magnet synchronous motors: Practical methods and challenges. *Sustainability*, 15(23), 16326. https://doi.org/10.3390/su152316326.

Niu, L., Zhang, X., & Li, Y. (2023). The optimal design and research of interior permanent magnet synchronous motor for electric vehicles. *IET Electric Power Applications*, 17(8), 1234–1245. https://doi.org/10.1049/tje2.12258.

Pyrhönen, J., Jokinen, T., & Hrabovcova, V. (2023). *Design of rotating electrical machines* (3rd ed.). Wiley.

Qiu, H., Zhang, Y., & Liu, X. (2024). Analysis of low saliency ratio and torque characteristics of fractional-slot permanent magnet synchronous motors considering magnetic saturation. *Archives of Electrical Engineering*, 73(1), 167–180.

Wang, Q., Xue, J., Wang, G., Hu, Y., & Xu, D. (2024). Review of inductance identification methods considering inverter nonlinearity for PMSM. *Chinese Journal of Electrical Engineering*, 10(2). https://doi.org/10.23919/CJEE.2023.000046

Xu, Z., Wang, M., & Ding, S. (2025). Research on magnetic–thermal coupling calculation of permanent magnet motors considering temperature effects on electromagnetic performance. *Energies*, 18(8), 1891. https://doi.org/10.3390/en18081891

Yan, M., Wang, B., Chen, Q., & Peng, X. (2024). Parameter identification for maximum torque per ampere control of permanent magnet synchronous motors considering magnetic saturation. *Electronics*, 13(4), 699. https://doi.org/10.3390/electronics13040699

Zhu, Z. Q., & Howe, D. (2007). Electrical machines and drives for electric, hybrid, and fuel cell vehicles. *Proceedings of the IEEE*, 95(4), 746–765. https://doi.org/10.1109/JPROC.2006.892482.


BİDGE